Electromagnetic Radiator Characterization and Modeling Through Planar Near-Field Measurements

By
Tareef Ibrahim Al-Mahdawi,
B.Sc.(Eng.), M.Sc.(Eng.)
Department of Electrical Engineering
McGill University, Montréal
December 1991

A thesis submitted to the Faculty of Graduate Studies and Research in partial fulfillment of the requirements for the degree of Doctor of Philosophy

ABSTRACT:

This thesis deals with the use of planar near-field measurements for characterizing and modeling general electromagnetic radiators, particularly non-directive ones.

Relationships between the measured field on a plane and the equivalent currents on the radiator plane were established. These were used to determine the resolution with which these currents can be mapped. The equivalent currents then serve as a model from which the radiator external field can be calculated. It was shown that significant filtering of measurement errors results from the utilization of such a model. The consequent reduction in errors was estimated.

The behavior of the measurement probe was studied in depth. The two general probe types, wire and aperture, were analyzed, and field extraction formulation and procedure were established.

The techniques developed were applied to the experimental study of three different radiators leading to new information about their behavior. Results show close agreement between the calculated field values from the model and those measured directly.

RÉSUMÉ

Cette thèse porte sur l'utilisation des mesures planaires des champs proches en vue de la caractérisation et de la modélisation des radiateurs électromagnetiques en général, et en particulier des non-directionnels.

Les relations entre le champ mesuré sur un plan et les courants equivalents du plan radiateur sont établies. Elles sont utilisées pour determiner la resolution avec laquelle ces courants peuvent être tracés. Les courants équivalents servent ensuite comme modèle à partir duquel le champ externe du radiateur peut être calcule Il est prouvé qu'un filtrage significatif des erreurs de mesure découle de l'utilisation d'un tel modèle. La réduction des erreurs est estimée.

Le comportement de la sonde de mesure est etudie en détail. Les deux types généraux, à fil et à ouverture, sont analysés et une procédure et une formulation de l'extraction du champ sont établies.

Les techniques développees ont ete appliquées à l'étude expérimentale de trois différents radiateurs, conduisant à des avancées dans la connaissance de leur comportement. Les résultats démontrent un bon accord entre les valeurs du champ calculées d'après le modèle et celles mesurées directement.

ACKNOWLEDGEMENTS

I would like to thank Professor Tomas Pavlasek for his guidance and encouragement during the research and throughout writing this thesis.

The assistance of the technical staff in the Department of Electrical Engineering was valuable for carrying out the experimental part of this research. I would like to mention specifically Mr. John Foldvari for his help in building the experimental apparatus, Mr.John Walker for his assistance in fabricating the two microstrip patches mentioned in the thesis and Mr.Joseph Mui for producing the masks for printing these patches.

My appreciation extends to my friends Dave Lunney for proof-reading the manuscripts, Stephane Aubry for translating the abstract into French and finally Susanne Woodhouse for checking and correcting the early version of the first two chapters.

This work is dedicated to my parents, my sister Hadeel and my brother Samir.

TABLE OF CONTENTS

CHAPTER FOUR: APPLICATIONS

CHAPTER FIVE: CONCLUSIONS

CHAPTER ONE

INTRODUCTION

Near-field measurement techniques have, in the past decade, become an important component of antenna metrology and are, in many applications, replacing classical ones such as far-field range techniques. The methods developed have proved practical, reliable, cost and space effective in measuring the far-field behavior of large, highly directive antennas. Accordingly, the methodology of the measurement and the analytical work, used to determine the far-field, are largely directed to deal with this type of antenna. The work presented here, on the other hand, examines the near-field measurement theory for electromagnetic radiators in general Dealing with non-directive radiators has, therefore, required a re-examination and extension of the current practice in handling near-field measurements. This thesis considers the applications of planar near-field measurement on such radiators to determine the equivalent radiating currents at the radiating sources This enabled the evaluation of other radiation characteristics of the radiator, such as the near-field and the far-field from these currents.

Large, highly directive antennas are usually complete radiating systems, e.g. satellite or earth station antennas, and their specifications, particularly the far-field behavior, need to be tested. Non-directive radiators, on the other hand, differ in that they may form parts of the antenna system, such as feeds or array elements. A known radiating current model is, therefore, useful for integration into an antenna system. Alternatively, this might be non-intentional radiator, such as a junction or a discontinuity in a microwave integrated circuit, which produce radiation. This radiation is usually not desirable, but definitely needs to be taken into account.

The following section discusses the basic ideas and the state of the art in the subject of near-field measurements An extensive amount of literature exists about near-field measurements. Introductory references include the chapter on antenna measurements in the *Handbook of Antenna Design*[1], and the special issue of *IEEE Transactions on Antennas and Propagation*[2] The review paper by Yaghjian[3] is of particular interest, and it contains a major bibliography on the subject. The physical and mathematical nature of the problem is discussed in the third section as an overview of the ideas that are dealt with in the following chapters. At the end of this chapter, the necessary conventions and terminology employed in the subsequent chapters are clarified, followed by a section pointing out the original features that this thesis has introduced.

1.1. Development of Near-Field Measurements Principles and Techniques:

The practice of near-field scanning of microwave radiators was pioneered in the early 1950's. The main purpose was to understand the radiation mechanism of microwave antennas, scatterers and lenses, which was essential in the development process of radar systems. Amplitude and phase field maps were indispensable in understanding the radiation and diffraction phenomena in the microwave frequency range, and of the departure of the radiated field from the geometrical optics approximation in the vicinity of radiators and scatterers. The available scanners and data acquisition permitted the plotting of some detailed field structures, such as the one shown by Sletten[4] as Figure (17.5). The computing power and processing algorithms available at that time did not permit further elaboration. For the same reasons, there were no attempts to produce the original fields from the measurement probe data. There was, however, some interest in the development of probes for that purpose[5].

Some interest in the evaluation of the far-field radiation pattern using the near-field measured data evolved in the early 1960's. Brown and Jull[6] experimented with two dimensional radiators using cylindrical wave expansion: Field values were extracted from the measurement probe data using simplified probe models and the radiation pattern was predicted from this data.

The requirement of smaller space for testing large antennas has led to the development of indoor testing. Other advantages are gained from indoor measurements, such as independence from weather, confidentiality, and above all, freedom from reflections from the surroundings due to the utilization of anechoic testing chambers. Near-field testing of microwave antennas became practical, especially with the evolution of computer control and data acquisition, and the development of the algorithms necessary for efficient calculation of the far-field radiation pattern from the near-field data. This led to the development of modern near-field antenna testing practices, whose principles are reviewed in the following sub-section.

1.1.1. Radiation Pattern Prediction:

One of the characteristics of a field described by Maxwell's equations is the uniqueness principle[7], which implies that the field in a closed region can be uniquely determined if the tangential electric or magnetic fields on the boundary are specified. It follows that when the tangential field on a closed surface surrounding electromagnetic sources, e.g. an antenna, is measured, the field exterior to that surface can be uniquely specified. The source-free region in this case is the one bounded by the closed measurement surface and infinity, at which the field is known to vanish. If the

measurement surface is of infinite extent, such as an infinite plane separating two half spaces, the field in the empty half space is unique. This is the basis of the far-field radiation pattern evaluation of an antenna from the near-field measurement. The details involve the shape of the measurement surface and the measurement technique. The Huygens-Fresnel principle[8], which states that each point on a given wave-front can be regarded as a secondary source giving rise to spherical wavelet, provides one way of calculating the fields. An alternative way of expressing this, is by using the Equivalence theorem[7] to replace the measured field by equivalent electric and magnetic currents, and then calculating the field contribution from these sources, as implied by equations (2.1) and (2.2) in this thesis.

There are problems in employing this approach of direct calculation of the far-field Performing an integration over the measurement surface for each point on the far-field is numerically inefficient. There is also no criterion defining the sample spacing on the surface of measurement, which might result in measuring a prohibitively large number of unnecessary data points. This approach necessitates measuring both the tangential electric and magnetic fields at each point, which can be impractical. The assumption made here is that the field can be measured at a point, which is not true, since the probe has to have a finite size. It is worth mentioning here that such an approach excludes any possibility of using the measured data to gain information about the field interior to the surface of measurement.

The modal expansion of the electromagnetic field simplifies the above mentioned difficulties. Stratton[9] had formulated the modal expansion of the solution of the homogeneous (source-free) Helmholtz equation, in which a solution is expressed as an integral of elementary solutions over the mode variables, or:

$$\vec{E}(\vec{r}) = \int\int_{\alpha\,\beta} [A_e(\alpha,\beta)\vec{T}_e(\alpha,\beta,\vec{r}) + A_m(\alpha,\beta)\vec{T}_m(\alpha,\beta,\vec{r})]d\alpha d\beta \qquad ..(1.1)$$

where; $\vec{E}(\vec{r})$ is the electric field as a function of the space variable $\vec{r}$. $\vec{T}_{e,m}(\alpha,\beta,\vec{r})$ are the TE and TM elementary solutions, respectively, as functions of the space variable, and defined by the modal variables α and β. The weights for each mode are $A_{e,m}(\alpha,\beta)$, which, when specified over the domain of the mode variable, will result in an analytical description of the field over the source-free region. Examples of elementary modes are plane, cylindrical and spherical waves, for which the specific forms of Equation (1.1) can be found elsewhere[1,3]

The above description of the field made it possible to design practical measurement procedures. In these, the measurement of the near-field over planar, cylindrical or spherical surfaces results in the determination of the weights of each mode in planar,

cylindrical and spherical field expansion respectively. The main reason for specifying measurement surface shapes is the fact that the Helmholtz equation is separable in these coordinate systems, and the modes are orthogonal over these surfaces. This allows the use of Fourier transformation for planar surfaces and equivalent transforms for the other two shapes[1]. This will be shown in Chapter Two when dealing with the planar field expansion. The modal field expansion facilitates the derivation of asymptotic expressions for the far-field directly from the modal weights, as derived by Collin[10] for plane-wave modal expansion, and as summarized by Yaghjian[3] for the three forms of expansion indicated here.

The modal field expansion also allows the definition of measured field sampling criteria. This is demonstrated in Section (2.5) of this thesis for planar measurements, and there exist similar criteria for the other scanning schemes[11,12]. The utilization of field expansion represents the state of the art in near-field measurements for radiation pattern prediction. Research on this subject concentrates on improving the accuracy and efficiency in calculating the far-field[2].

There has been some work reported recently[13,14] which uses the equivalent currents at the radiator aperture to evaluate the far-field. These equivalent currents are calculated from exterior field measurement This approach is similar to that employed in this thesis in the sense of utilizing the equivalent currents, but differs in the method of evaluation of these currents. This has resulted in major differences between the two approaches regarding experiment design and measurement error handling. A comparison between them was, therefore, detailed later in Chapter Five.

1.1.2. Antenna Diagnostics and Near-Field Metrology:

One application of near-field measurements is to gain information about field structure in the vicinity of the radiators. As stated earlier, the first near-field measurement practice was concerned with using near-field data to produce field maps, which can be used to understand the radiation phenomena of different antennas and scatterers. There were no attempts to process these results further. There is still some interest in this approach, especially for antennas where understanding of the radiation mechanism is not highly developed Levine[15] reported some work on probing the field very close to microstrip radiators He produced pictures of the field by scanning the measuring probe very close to microstrip patches and arrays. In spite of the valuable information that can be gained from these plots, they cannot be used for quantitative evaluation of the immediate field of the radiators because of the close proximity of the measuring probe to the radiator surface. This proximity causes modification of the original radiation mechanism of the radiator by the measuring probe.

Frayne[16] has recently reported a technique he developed for surface-field metrology of open microstrip structures. The technique uses a small monopole for producing detailed electric field maps of the normal component over these structures, for diagnostic purposes. This technique has been developed independently here, and used by the author to produce similar maps for model confirmation and qualitative field probing as demonstrated in sections (3.1) and (3.2). The method, however, cannot be used to gain precise quantitative information about the immediate field, because of the strong interaction between the radiator and the measuring probe.

The modal field expansion allowed the development of some techniques, that use the near-field data measured at moderate distance from an antenna, to predict the immediate field at the surface of the radiator. These techniques are based on the fact that once the complex amplitude of each mode, $A_{e,m}(\alpha,\beta)$ in Equation (1.1), is determined, an analytical representation of the whole field structure throughout the source-free region results. However, this can also be used to evaluate the field back at the radiator surface, provided the radiator itself is excluded from that region. The limitation in this case is that some modes grow larger as they are referred backwards, and their calculation at that surface will result in significant multiplication of the measurement errors. These modes, sometimes called *invisible*, are contributed by the reactive part of the field around the radiator, which decays rapidly away from the radiator. The inability to use these modes in radiator surface-field metrology permits only the possibility of gaining partial, or smoothed, reconstruction of the field. This limitation is discussed in detail in chapter two of this thesis for the planar near-field scanning scheme.

The above technique is applied in antenna diagnostics, in which the field on a reflector antenna surface is estimated to locate deformations of the reflecting surface using near-field measurement on planar[17], plane-polar[18] or complex radiation pattern measurement, which is similar in principles to spherical near-field scanning[19]. Another application in antenna near-field metrology is to locate faulty elements in large planar arrays, by measuring the near-field and referring back to the array plane[20]. All these applications involve large reflectors or arrays, for which only a small range of modes need to be considered in mapping the antenna surface because of the high directivity of these radiators. The type and behavior of the measurement probe, also, does not pose serious issues in dealing with the measurement results as will be demonstrated in the following two chapters in this thesis.

There have been some attempts to map the immediate field of small, non-directive radiators, such as a slit, using near-field measured data[21], and employing an extension of optical holographic techniques into the vector electromagnetic field. The method uses modal field expansion, but makes assumptions about the radiator, such as boundary conditions and analytical continuation, to predict the non-radiating modes. This resulted

in improved imaging resolution, but quantitative uncertainty. In fact, source imaging in this case uses a form of regularization discussed in Section (2.2). The resulting mapped sources, therefore, cannot be used to represent the radiation behavior of the radiator. The work reported by Joy[22,23,24], which uses spherical backward transform, to find the immediate fields of radomes and small radiators, is successful in dealing with the non-directive radiator because of the use of spherical near-field scanning. It is necessary, however, to enclose the whole radiator including the supporting structure, by the scanned surface The method is therefore not applicable to small radiators with large supporting structures, such as those dealt with in Chapter Four

The utilization of the equivalent currents of the radiator to calculate the exterior fields at non-asymptotic distances, i e. near-field, is discussed in Chapter Two of this thesis. Lewis and Newell[25], evaluated the near-field of a directive antenna directly from the plane wave spectrum (modal expansion in cartesian coordinate system) of the measured field, using local integration of the plane wave spectrum. The main problem in applying this approach to a non-directive radiator is the accumulation of certain measurement errors on small area of the plane wave spectrum as will be discussed in Section (2.7). This might effect the accuracy of field calculation if the local spectrum integration was carried out over this area.

1.1.3. Field Probe Considerations:

In the early applications of near-field measurements, the measurement probe output was considered to be proportional to one of the field components at the point of measurement. This required the selection of probes with small effective aperture, highly polarized with enough output power to activate the measuring instruments[5]. Woonton[26] concluded that a probe should not be longer than one-half wavelength, linearly polarized, and not more directive than a half-wave dipole. These requirements were convenient for qualitative field mapping. Probes that fit these requirements are still being used in investigative and diagnostic measurements[16,27,28].

Interest in near-field measurement for radiation pattern prediction had imposed the consideration of detailed behavior of the measuring probe. The early work on this subject by Brown and Jull[6], using cylindrical near-field measurements, had considered the averaging effect of the field probe discussed in Section (3.1). They proposed compensating for that effect by multiplying each mode by a constant which could be derived from the probe radiation pattern using the reciprocity theorem.

The emergence of near-field scanning as a technique of antenna measurements had encouraged the search for more rigorous methods to account for the measuring probe. One of the early works is the introduction by Kerns[29,30] of the plane-wave scattering matrix, which deals with the problem as three cascaded networks the antenna under test is a single-input multi-output network, with the antenna feed as the input and each planar mode as an output port The space separating the antenna and the probe modifies each mode according to the propagation constant of that mode, and the measuring probe is a multi-input single-output network, with each propagated mode as an input, and the measured probe voltage as an output. This enabled the utilization of an S-parameter circuit representation to construct the planar modal expansion of the radiated field from the measured near-field on a plane The far-field is evaluated asymptotically from that expansion as stated earlier. This theory, which was later documented in a book[30], uses the circuit form of the reciprocity theorem and assumes that negligible multiple scattering occurs between the antenna under test and the probe The multiple scattering will complicate the interaction mechanism between the antenna and the probe by modifying the electromagnetic behavior of the antenna while the probe is scanning. Coupling between the probe and the radiated modes, which is otherwise a linear convolution relation, e g Equation (3 1), becomes a highly complicated phenomenon.

The use of modal expansion, the reciprocity theorem and the assumption of negligible multiple scattering is used throughout subsequent work published about this subject. Variations exist such as consideration of different scanning geometries[12,31,32], applying the electromagnetic fields version of the reciprocity theorem[33], and the analytical convenience resulting from expressing the measured probe output as a vector with each component corresponding to a probe orientation. The latter proved valuable in this thesis in representing the probe output voltage.

In the formulation associated with the near-field measurement, the mathematical representation of the probe was by *either* the modal expansion of the fields exterior to the probe as a radiator *or* by the phasor radiation pattern of the probe This represents both analytical and experimental convenience, since the phasor radiation pattern of the probe can be measured with acceptable space investment. This is attributed to the small size of the probe, and to the fact that the radiating part of the modal field expansion can be evaluated from this phasor radiation pattern[34] Coupling between the antenna under test and the measuring probe is expressed in terms of the modal expansion of the fields radiated by both[1], or their complex far-field radiation pattern[35]. The selection of the probe and the evaluation of the probe performance under near-field measurement environment are determined by the characteristics of the probe such as the gain and the shape or location of nulls in the radiation pattern. In other words, the probe output is supposed to respond, in a measurable way, to all the expected significant radiated modes from the antenna under test.

The effect of the probe behavior varies depending on the shape of the measurement surface and the antenna under test[3]. The most severe case is in the planar scanning surface, and non-directive radiator, where the coupling between the probe and the radiator under test will depend on the probe receiving characteristics for large off-boresight angles, while for the spherical scanning surface, the boresight direction of the probe will always be facing the radiator under test, so that for a scanning surface radius of several radiator diameters, the probe behavior need not be considered off-boresight.

1.2. On Thesis Objectives and Methodology:

A unique definition of the electromagnetic fields can be accomplished through defining the sources, or the radiating currents. In the Near-Far-Field transformation technique, the near-field data is considered to represent secondary sources from which a unique far-field can be defined. The complete description of the radiation from a general electromagnetic radiator, however, requires the definition of equivalent radiating currents on the radiator surface, from which the field at any point exterior to the radiator can be calculated The equivalent sources can be measured directly if there is available some measuring probe that does not interact electromagnetically with the measured sources. Usually this is not possible even as an approximation, since a measuring probe must absorb power from the sources, and consequently, must have a finite size. Its presence, therefore, may highly modify the sources or the radiation mechanism It is possible, however, to use the near-field data, measured at some reasonable distance from the radiator, to gain information about the radiating sources. Chapter Two in this thesis deals with the problem of employing planar near-field scanning to determine the source distribution.

The limitations in the evaluation of the equivalent sources are defined for different source representations in Chapter Two Measurement configuration and parameters for this purpose are suggested Furthermore, the chapter defines the problem encountered in finding the field quantities in the near-field region from the measured near-field data. These data are available, for practical purposes, in the form of plane-wave spectra. A method is, therefore, suggested for evaluating the near-field quantities. A study of the effect of errors on the near-field evaluation is carried out in the same chapter, and the problems in the calculation of the near-field directly from the plane wave spectrum are discussed for non-directive radiators. A major consequence is that it can be shown that the use of the equivalent current model to determine the external fields tends to filter out some of the measurement errors. The extent of this filtering is evaluated.

It is assumed in Chapter Two that the field data at the surface or plane of measurement is available from the measuring probe. Chapter Three deals with the extraction of the field quantities from the measurement probe output voltage. It is demonstrated there, that the characterization of the measuring probe is of significant importance in the interpretation of the measurement results. The probe behavior under the planar near-field measurement environment is examined thoroughly to determine, in addition to the method of field extraction, the limitations imposed by the measurement noise and uncertainty, and the significance of the probe type on the interpretation and extraction process. This chapter introduces some theoretical and experimental methods for determining the field extraction parameters for the measuring probes, and finally, indicate the advantages of the adopted technique in comparison with the known approaches.

Chapter Four deals with applications of some of the developed theory. The first radiator dealt with is an approximation of an infinite, open, microstrip edge. Diagnostic field probing is used to validate the approximation, and scanned measurements are used to gain useful information about the edge. The second part deals with a small microstrip patch radiator. In this case, the field has three dimensional structure compared to the two dimensional structure of the previous case The aim, in this case, is to examine the extent to which the near and immediate field measurement can be used to reveal the radiation behavior of such a sub-wavelength sized antenna. The third radiator considered is a horn cluster used as a feed for a satellite reflector antenna. This represents a case of a relatively larger radiator, which is still not highly-directive. Dealing with this kind of radiator is an attempt to find a practical application of the equivalent source mapping to represent the external field of the horn cluster It is noticed that for the three cases considered, the planar near-field scanning offers the most practical way of probing the field close to the radiator, because of the relatively large size of the supporting structure compared to the size of the radiating areas themselves.

1.3. The Theoretical and Mathematical Nature of the Problem:

Most of the theoretical and analytical work that this thesis deals with falls into one of the following categories:

i) The evaluation of far-field from near-field, or the near-field from the equivalent sources.

ii) The evaluation of the equivalent sources from the near-field measured data.

iii) The extraction of the field values from the measuring probe output voltage.

These cases are mathematically modeled throughout the thesis, such as equations (2.1) and (2.2), with the unknown outside the integral for case (i), the same equations with the currents as the unknown inside the integral for case (ii), and Equation (3.1) for the case (iii).

It is noted that the basic mathematical form of the three cases can be described by the relation:

$$\mathcal{A}x = b \qquad \ldots.(1.2)$$

where $\mathcal{A}$ is a convolution operator, x is the function describing sources (cause) on which $\mathcal{A}$ would operate to produce the effect b. By analogy to the cases described above, x is the measured near-field, the equivalent sources, or the field incident on the measuring probe for the three cases respectively. On the other hand, b represents the far-field, the measured near-field or the measuring probe output voltage, respectively. This way of looking into the problem will identify case (i) as the forward evaluation of an integral, for which one has only to worry about ensuring proper sampling of the sources (the measured near-field) to guarantee a correct evaluation of the far-field.

Cases (ii) and (iii) involves the solution of an integral equation, with the unknown, the equivalent sources or the near-field respectively, inside the integral, from the knowledge of the quantities outside the integral, the measured near-field or the probe output voltage respectively. This is easily distinguished as an inverse problem. One has to worry, in addition to the source and effect sampling, about the existence, uniqueness, and the sensitivity of the solution[36,37]. It is necessary to modify the convolution relation to facilitate partial solutions, and to examine the limitations of these solutions.

The physical nature of the problem comes from the fact that the operator $\mathcal{A}$ is defined by the measurement configuration in cases (i) and (ii), and additionally, by the probe geometry and orientation in case (iii). This implies that these factors play direct roles in defining the mathematical problem and the possibility of a solution. This link enabled setting criteria and rules for measurement configuration, probe selection and design as demonstrated by the following two chapters.

It seems that the majority of the theoretical work in this thesis can be described in the above abstract fashion, except at some points of the work, where it is important to use unprocessed information gained from raw measurement data for investigative or diagnostic purposes.

1.4. Comments on Conventions and Terminology:

The terms *immediate, near-* and *far-* field are used extensively in this work, to define regions in the space exterior to the radiator, based on the nature of the field at these regions. The immediate field region is that where the radiator reactive field is measurable, due to the existence of the non-propagating modes in addition to the radiating ones. The near-field region, which is further away from the radiator, is dominated by the radiated modes, while the reactive modes are not detectable. The field at a point there, however, cannot be assumed as the contribution of a single plane wave as is the case with the far-field region. In the far-field region, on the other hand, the radiator is far enough that it will behave like a point radiator. The field quantities will accordingly have $e^{-jk_0 r}/r$ dependence where: r is the radial distance and k_0 is the intrinsic wave number of the medium.

There are no strict criteria to define boundaries between these regions, but based on experience in near-field measurements, the immediate (or reactive) field region extends to within one wavelength away from the radiator surface. The near-field region extends up to $2D^2/\lambda + \lambda$ from the radiator, where D is the largest antenna dimension and λ is the wavelength at the operating frequency. Sometimes the immediate field region is considered as a sub-region of the near-field region[3]. The use of modal expansion made it convenient, occasionally, to use the term *evanescent* region for the immediate field region, because of the significant contribution of the evanescent (or reactive) modes in this region.

Great advantage was gained in this work by employing the concept of duality between the electric and magnetic fields and currents The terms *field, current* or *current distribution* when used without specifying their type, implies that the discussion applies to both electric or magnetic fields and currents.

The modal (or eigen function) expansion has been used in this work, as is the case with most of the literature dealing with near-field measurements. The planar modal expansion has particularly been used, for which different terms were employed to designate this expansion such as plane wave spectrum[30], spectral domain representation or angular spectrum[38], because of the Fourier transform relationship between the modal representation and the space domain dependence. This terminology was discussed by Zucker[10] and accordingly, the terms spectral domain representation and spectral variables refer to the planar modal expansion and the modal variables, as opposed to the space domain representation and space variables. The terms field or current mapping indicate the evaluation of space domain description of the fields and currents.

1.5. Claim of Originality:

The author would like to claim the originality of the following features presented in this thesis:

1. The utilization of an equivalent current distribution, calculated from planar measurement data, as a model from which the external fields of the radiator under test can be calculated. It is shown in Section (2.6) that this will result in stable calculation of the near-field quantities, and also shown in Section (2 7) that the possibility of space domain truncation of the equivalent current distribution will result in significant reduction in measurement errors The amount of reduction in measurement errors was estimated. The technique was applied to the radiators tested in Chapter Four, where the utility and the advantages of the approach was demonstrated. These measurements in themselves are also original contributions.

2. The definition of the mapping limitations of the equivalent currents (or the immediate fields) at the radiator plane (Section (2.4) and figures (2.4) and (2.5)). The important feature of this definition is the handling of the evanescent modes, or the reactive field components. Measured evanescent modes were actually used to calculate the current distributions shown in figures (4.5), (4.16) and (4.17).

3. The procedure of field extraction using the *Vector Field Extraction Coefficients* which are linked to the measurement probe electromagnetic behavior[39]. This link allowed the new interpretation of the output of the measuring probe demonstrated by Figure (3.4), and the evaluation of measurement validity limits as shown in Figure (3.6). An experimental procedure and the related analysis were suggested and implemented within Section (3.4) for the measurement of the field extraction parameters of a dipole probe[40].

4. The suggestion and implementation of an experimental model in Section (4.1), which approximates an infinite microstrip edge. This claim includes the use of the near-field measurement on this model to reveal the characteristics of an infinite edge. This approach can be applied to study other infinite two dimensional structures, such as slits or edges.

CHAPTER TWO

THEORETICAL FOUNDATIONS OF MEASUREMENTS

This chapter deals with the problem of defining the mathematical relationships which permit the determination of a radiating source from a measurement of its external field The conditions and the parameters of the measurement process are also defined. First, a general model of the radiator is introduced in the form of equivalent electric or magnetic current distributions, then, the relations between these currents and the measured field are established Such a problem is recognized to be an ill-posed inverse problem when formulated in the space domain The spectral domain approach is therefore utilized to permit a well-posed formulation of the problem.

Practical considerations are taken into account in the formulation, such as the nature of the available measuring instruments and the field probe (whose detailed considerations is the subject of Chapter Three) The mechanical structures involved are such that the planar field scanning is of main concern in this chapter. This is evident in the applications described in Chapter Four. Also, since only the two field components tangential to the measurement surface may be available, this possibility is considered as well as the general case.

Additionally, the measured sources determined from the measurement will be sensitive to noise and errors in the measured fields. This sensitivity is determined analytically to obtain suitable formulae for the maximum measured field resolution. The required measurement sampling rate is also considered The computational determination of the near-field surrounding the radiator from planar near-field measurement is investigated, and a method is proposed towards this objective, taking into account the non-directive nature of the radiator under consideration.

Finally, this chapter discusses the sources of measurement noise and errors, with specific attention to non-directive radiator measurements, and examines the measurement error contribution to errors in the radiator model.

2.1. Radiator Models:

This section reviews the well established principles on which the radiator models are based, and discusses some of the concepts needed to structure an appropriate model.

Electromagnetic fields are naturally generated from electric currents and charges, and since the charges are related to the currents by the equation of continuity ($\nabla . J = -\rho$), the radiator can be described by electric current distributions alone. Consequently, the antenna radiation behavior can be specified uniquely by such a current distribution within its volume. The electric current distribution can work as a convenient model for certain type of antennas like the dipoles and loops, where the radiated fields are generated by relatively simple electric current distributions. For other antennas with more complicated structures, the description of the antenna in terms of the actual electric currents is rather complicated if not impossible Different types of aperture antennas are good examples of these cases, e g electromagnetic horns The radiation sources for these antennas would be simpler when described in terms of the aperture electric field distribution. The exterior fields of these antennas can be calculated from the aperture field using the Huygens-Fresnel principle[8]. The equivalence principle[7] can also be used to replace these aperture fields by equivalent fictitious magnetic currents without changing the external fields of the antenna This will result in a complete symmetry of Maxwell equations The duality between the electric and magnetic currents is used to unify the approach of treating electric current and aperture radiators.

It can be shown that, for a planar source model, and using the image principle, the field sources can be represented by *either* equivalent electric *or* magnetic current outside the source region[41]. In the planar source representation adopted in this work, the choice of the current type will affect the shape of the resulting current distribution. For example, if a horn antenna is modeled as a magnetic current source, the current distribution will be localized in and about the horn aperture area. Representing the horn with electric current sources will result in distributing that current over a large area within the plane containing the aperture This leads to the conclusion that it is preferable to take the nature of the radiator into account before selecting the type of equivalent current that can best represent the radiation behavior.

The problem of characterizing the external behavior of the antenna can be restated here as that of finding the equivalent electric and/or magnetic currents that contribute to the external field of the antenna. Figure (2.1) shows examples of antennas with their suggested equivalent currents. It can be demonstrated that, in general, wire antennas and aperture antennas are more conveniently represented by electric current and magnetic current sources respectively. The problem of determining the sources from the measured field, is easily recognized as an inverse problem for which, the existence, uniqueness and sensitivity of the solutions[36] have to be considered.

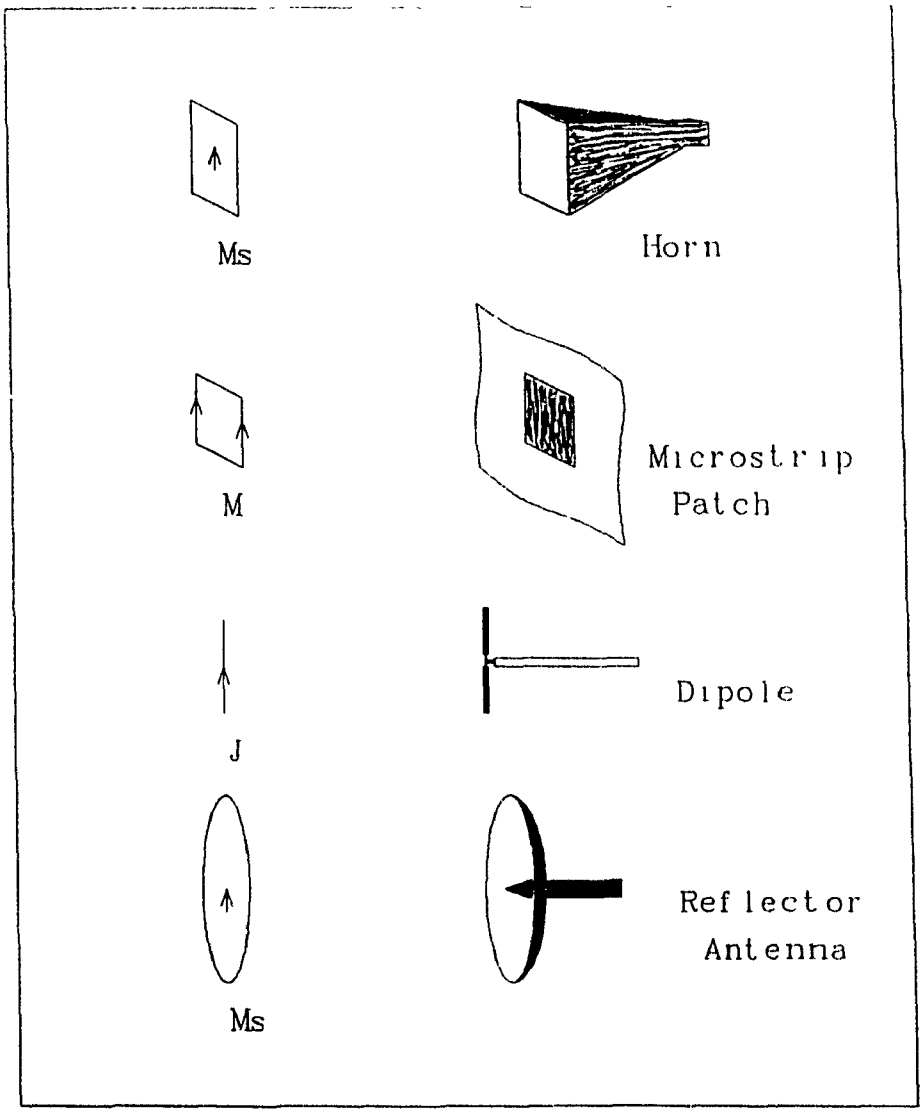

Figure (2.1): Examples of antennas with their equivalent current distribution.

It is known from the principles of inverse problem formulation[36,37,42] that one way of facilitating a solution is to include some assumption or *a priori* information about the solution. There seems to be logical contradiction between this requirement and the fact that an investigative measurement is attempted. Any assumptions will imply that the nature of the measured results is already known, which is not always the case. The only trade off employed here is that the sources are located on a plane (radiator plane), since this thesis deals with antennas with planar apertures.

2.2. General Relation between Source Currents and Measured Fields:

A general geometry which corresponds to the problem of defining the current distribution of a radiator from the measured field quantities on a surface, is illustrated in Figure (2.2). The radiator is represented by the tangential electric and magnetic currents $J(r')$ and $M(r')$ respectively on the surface S' surrounding the radiator. The field measurement surface is S on which it is assumed that $E(r)$ and (/or) $H(r)$ are determined by measurement. The relationship between the sources and the field is as follows:

$$\vec{E}(r) = \int_{S'} [\vec{G}_1(r/r').J_s(r') + \vec{G}_2(r/r').M_s(r')].dr' \quad \ldots\ldots\ldots\ldots (2.1)$$

and

$$\vec{H}(r) = \int_{S'} [\vec{G}_2(r/r').J_s(r') + \vec{G}_1(r/r').M_s(r')].dr' \quad \ldots\ldots\ldots\ldots (2.2)$$

Where the kernels $\vec{G}_1$ and $\vec{G}_2$ are, in general, the free space dyadic Green's functions[7].

Practically, either $\vec{E}(r)$ or $\vec{H}(r)$ are measured, so only one of the above relation would be used. Also, from the preceding section either J or M is used to define the external field.

The above equations are Fredholm's integral equations of the first kind which are generally ill-posed for smooth kernels[42]. This is the case here, since the measurement surface does not coincide with the sources. This kind of problem is encountered in many electromagnetic problems in addition to the inverse problem under consideration. The conventional approach is to limit the possible current distributions, or in other words to apply constraints on the permissible solutions of equations (2.1) and (2.2). This approach, which is called the regularization of the problem[37,42], relies on the trade off between accurate current distribution evaluation and the problem condition. This can take many forms, such as applying a smoothing factor to the current distribution, or

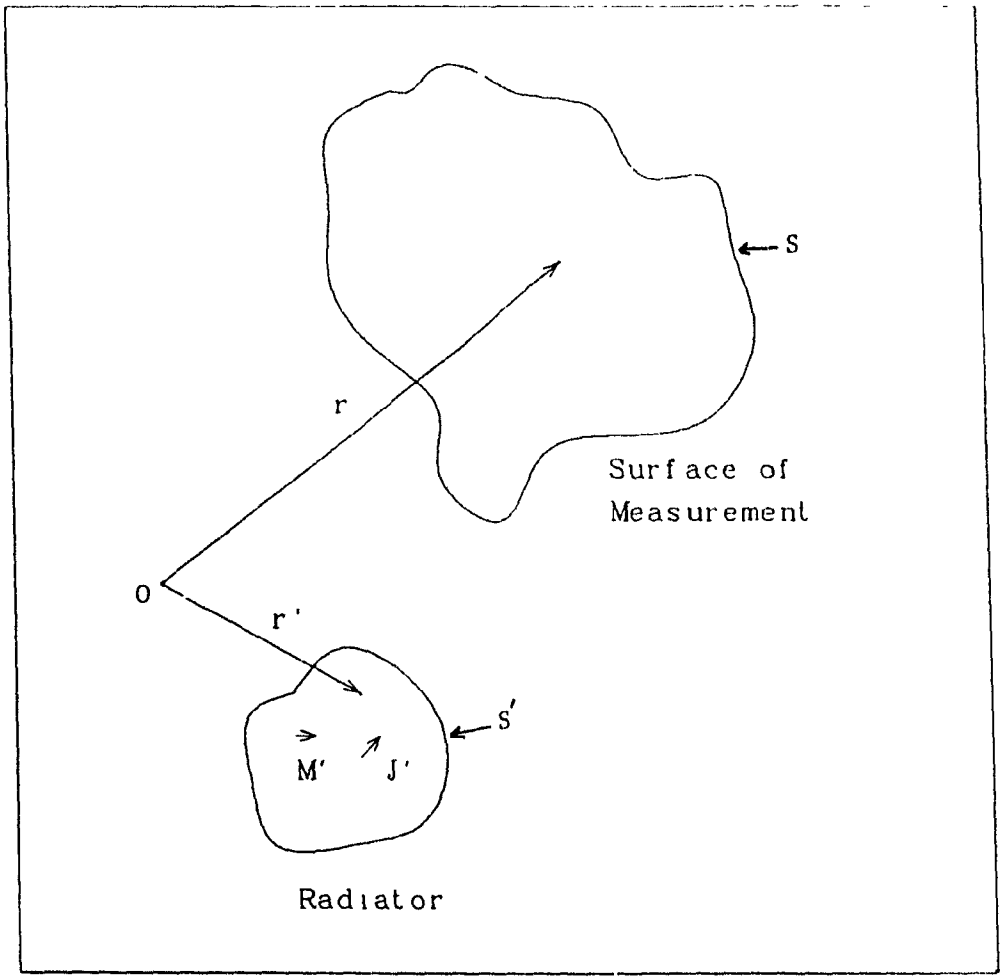

Figure (2.2): General near-field measurement configuration:
The radiator is represented here by equivalent current distribution. Information about the radiator field are gained through measuring fields at an exterior surface.

expanding the currents into orthogonal distribution functions, as is often used in numerical treatment of scattering problems, by expressing the currents as mutually orthogonal basis functions or modes [43].

In this work, considering the nature of the problem, the source expansion into orthogonal functions is adopted for the following reasons:

1. When the currents are expanded into certain entire domain modes[43] for which the Helmholtz equation is separable, and when the fields are similarly expanded, the modes will decouple The relation between the sources and fields will be algebraic which will allow separate treatment of the modes. This is advantageous numerically, and also allows the examination of the reliability of the inversion for each mode This will facilitate quantitative evaluation of the effect of the measurement noise and uncertainty on the determination of the sources

2. The predetermination of the modes, that can be reliably used towards the inversion procedure, gives an idea about the resolution with which the sources can be mapped for certain measurement configuration. The modal description of the field also allows establishing criteria for the sample spacing of the measured field, which was impossible for the general field description. This is demonstrated in Section (2.5) for the planar source model.

3. In near-field measurements, the determination of the radiated field from the field probe output is possible only when the field is expanded into orthogonal modes, except for the special cases specified in Chapter Three Thus, the field data is already available in the form of orthogonal modes

4. Other regularization schemes can be used to determine the radiating sources from the measured field but require pre-assumptions about the nature of the radiator to enable well-posed inversion formulation This can be useful in some cases where there is some confidence about the validity of the pre-assumptions. In general, presuming anything about sources may conflict with the objectives of investigative measurement.

2.3. Spectral Domain Formulation:

As stated in the Introduction, the external field in free space can be expanded as an integral of simple modes[7,9] over the domain of a mode vector, each mode having a complex amplitude as a function of the mode vector. The expansion of the field into planar modes is specified here, because planar immediate and near scanning is chosen in this work. This choice is justified by the fact that it is not necessary to enclose the whole radiator including the supporting structure, by the surface of measurement in planar scanning. This would be necessary for the other two available schemes, which are cylindrical and spherical scanning. The planar scanning surface will enable measuring the field close to the radiator, while minimizing the contribution of the supporting structure. This practical advantage can be demonstrated by observing the structure of the radiators dealt with in Chapter Four. As described in Appendix (C), the measuring equipment used is particularly convenient for planar measurements. Similar principles apply to other field expansions, such as cylindrical and spherical wave expansions, used in cylindrical and spherical measurements respectively[1].

The plane wave spectrum[38] (PWS) representation of electromagnetic fields is employed, but the decomposition of the field into TE and TM modes implied by Equation (1.1) is not considered here. This decomposition is based on the assumption that each mode can be looked at as a transmission line, whose characteristic impedance is determined by the mode variables and the mode type (TE or TM). This can be useful in evaluating the interaction between the radiator under test and the measuring probe using circuit concepts (S-parameters)[30]. Maxwell's equations are used here instead, to characterize the propagation and the interaction with the measurement probe of each mode, without the need for the type decomposition. This is useful in observing the influence of the probe's electromagnetic behavior on the measurement.

The measurement procedure is described here with reference to Figure (2.3). The probe is scanned over a plane S exterior to the radiator, using a field probe. Phasor output voltages are read from the probe on a regular grid, for different probe orientations, and the plane of measurement is extended to include an area over which the field magnitude is measurably significant. The extraction of field information from the probe output voltage is the subject of the next chapter. In the following development, however, it is assumed that the field quantities are already extracted from the measurement output data.

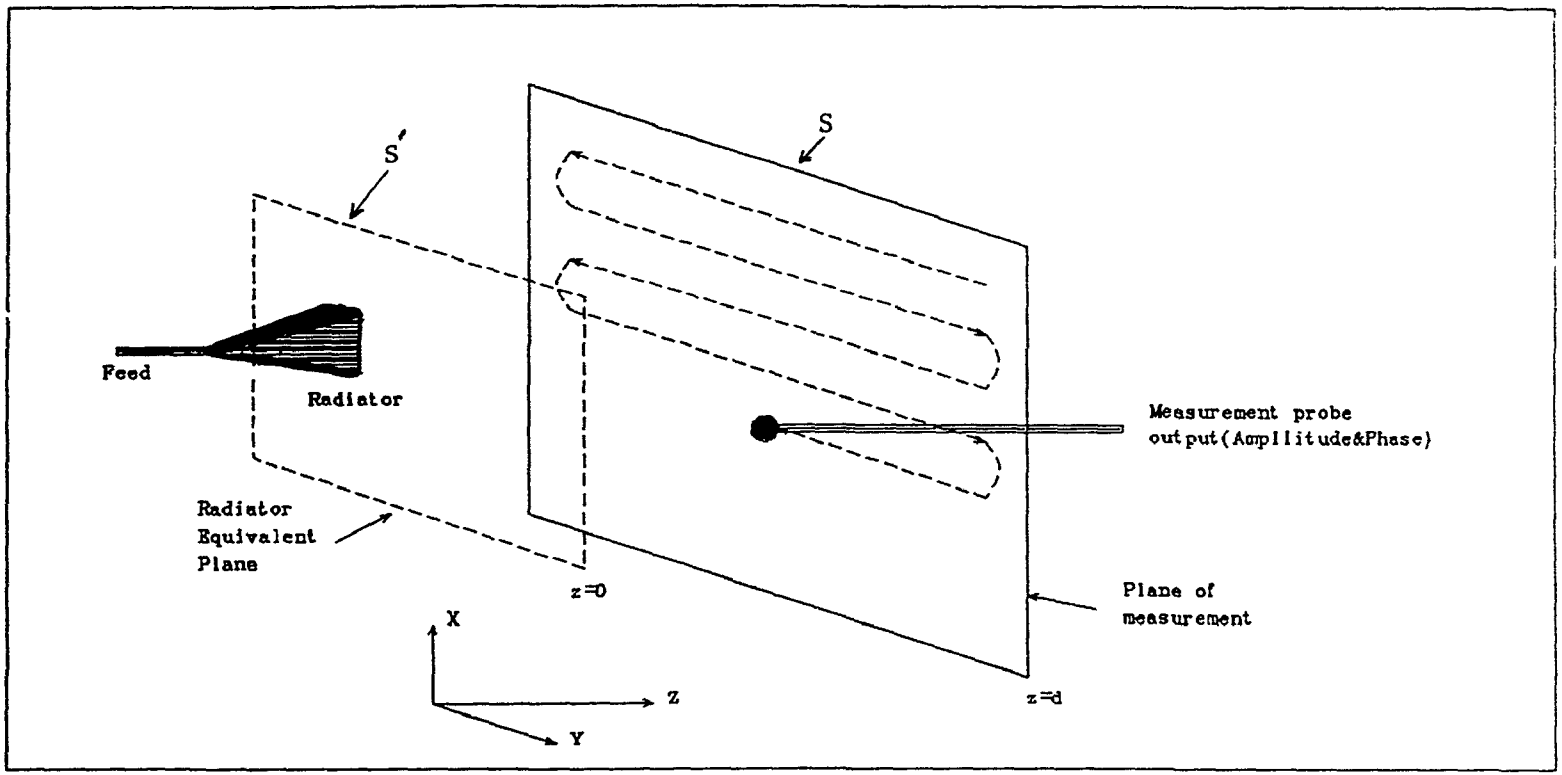

Figure (2.3): Planar near-field measurement is conducted by scanning the field probe over a regular grid on the plane of measurement, and recording the probe output amplitude and phase at each point.

2.3.1. Field-Source Relation in the Spectral Domain:

The equivalent currents on the antenna surface S' can be expressed as:

$$\vec{M}_s(x',y') = \hat{x}M_x(x',y') + \hat{y}M_y(x',y')$$

$$and \quad \vec{J}_s(x',y') = \hat{x}J_x(x',y') + \hat{y}J_y(x',y')$$

Alternately, these currents can be described as:

$$\vec{M}_s(x',y') = \int_{k_x}\int_{k_y} \vec{M}_s(k_x,k_y)e^{-j(k_x x' + k_y y')}dk_x dk_y \qquad ....(2.3-a)$$

$$and \quad \vec{J}_s(x',y') = \int_{k_x}\int_{k_y} \vec{J}_s(k_x,k_y)e^{-j(k_x x' + k_y y')}dk_x dk_y \qquad ....(2.3-b)$$

where; $\vec{M}_s(k_x,k_y)$ and $\vec{J}_s(k_x,k_y)$ are the two dimensional inverse Fourier transforms of the magnetic and electric currents respectively. It is recognized that the Fourier transform and its inverse are dual operations. Either will transform a function from the space domain (x,y) into the spectral domain (k_x,k_y) or vice versa. In this work, the inverse transform is used to transform from the space domain into spectral domain and the Fourier transform is used to transform from the spectral to the space domain. A single mode with spectral variable (k_x,k_y), therefore, can be described as:

$$\vec{M}(x',y') = (\hat{x}M_x(k_x,k_y) + \hat{y}M_y(k_x,k_y))e^{-j(k_x x' + k_y y')}$$

$$and \quad \vec{J}_s(x',y') = (\hat{x}J_x(k_x,k_y) + \hat{y}J_y(k_x,k_y))e^{-j(k_x x' + k_y y')}$$

The electric and magnetic fields can be related to these currents, but at this point, only the electric field is considered, since the magnetic field relations can be constructed by the duality properties of Maxwell's equations as stated earlier.

Considering the planar mode orthogonality[7], the vector potentials will have the same tangential (x,y) space dependence as the currents, but the z dependence is expressed in terms of a normal wave number k_z such that:

$$\vec{F}(x,y,z) = \vec{F}_o(k_x,k_y)e^{-j(k_x x + k_y y + k_z z)} \quad \text{and} \quad \vec{A}(x,y,z) = \vec{A}_o(k_x,k_y)e^{j(k_x x + k_y y + k_z z)} \qquad ....(2.4)$$

where[7]; $k_o^2 = k_x^2 + k_y^2 + k_z^2$, and $\vec{F}$ and $\vec{A}$ are the contributions of $\vec{M}$ and $\vec{J}$ respectively.

To comply with the radiation conditions for $z>0$ the normal wave number k_z is expressed as:

$$k_z = \sqrt{k_o^2 - k_x^2 - k_y^2} \qquad \text{for } k_z \text{ real}$$

$$k_z = -\sqrt{k_o^2 - k_x^2 - k_y^2} \qquad \text{for } k_z \text{ imaginary}$$

The electric field for $z>0$, which includes the measurement surface, can be evaluated from these potentials using the relations $\vec{E} = -\nabla \times \vec{F}$ and $\vec{E} = -j\omega\mu\vec{A} + \frac{1}{j\omega\epsilon}\nabla(\nabla.\vec{A})$. The mode magnitude of the potentials can be evaluated using the boundary conditions $\vec{M} = \hat{z} \times \vec{E}$, and $\vec{J} = -\hat{z} \times \vec{H}$ at the source plane. This results in expressing the electric field in terms of the magnetic and electric currents as:

$$\begin{bmatrix} E_x(k_x, k_y) \\ E_y(k_x, k_y) \\ E_z(k_x, k_y) \end{bmatrix} = \begin{bmatrix} 0 & -e^{-jk_z z} \\ e^{-jk_z z} & 0 \\ -\frac{k_y}{k_z}e^{-jk_z z} & \frac{k_x}{k_z}e^{-jk_z z} \end{bmatrix} \begin{bmatrix} M_x(k_x, k_y) \\ M_y(k_x, k_y) \end{bmatrix} \qquad \ldots.(2.5-a)$$

$$\begin{bmatrix} E_x(k_x, k_y) \\ E_y(k_x, k_y) \\ E_z(k_x, k_y) \end{bmatrix} = \frac{1}{j\omega\epsilon} \begin{bmatrix} \left(\frac{k_y^2}{k_z} + k_z\right)e^{-jk_z z} & \frac{-k_x k_y}{k_z}e^{-jk_z z} \\ \frac{-k_x k_y}{k_z}e^{-jk_z z} & \left(\frac{k_x^2}{k_z} + k_z\right)e^{-jk_z z} \\ -k_x e^{-jk_z z} & k_y e^{-jk_z z} \end{bmatrix} \begin{bmatrix} J_x(k_x, k_y) \\ J_y(k_x, k_y) \end{bmatrix} \qquad \ldots.(2.5-b)$$

Rewriting Equation (2.5) in a simplified form:

$$\vec{E}_M(k_x, k_y, z) = \vec{G}_1(k_x, k_y, z).\vec{M}_s(k_x, k_y) \qquad \ldots.(2.6-a)$$

$$\vec{F}_J(k_x, k_y, z) = \vec{G}_2(k_x, k_y, z).\vec{J}_s(k_x, k_y) \qquad \ldots.(2.6-b)$$

The electric field in the plane of measurement $z=d$, due to the radiator equivalent electric and magnetic current on the surface S', is expressed as:

$$\vec{E}_s(x, y, d) = \int_{k_x}\int_{k_y} [\vec{G}_1(k_x, k_y, d).\vec{M}_s(k_x, k_y) + \vec{G}_2(k_x, k_y, d).\vec{J}_s(k_x, k_y)]$$

$$e^{j(k_x x + k_y y)} dk_x dk_y \ldots.(2.7)$$

Two observations may be made at this stage about the above relations:

1. The algebraic form of the relations between the sources and fields facilitates a simplified determination of the condition of these relations. It is possible to evaluate J or M from E only for the modes (k_x, k_y) for which the determinants of $\bar{\bar{G}}_1$ or $\bar{\bar{G}}_2$ are non-zero or small enough to cause multiplication of measurement noise and errors beyond a pre-specified limits. An elaboration on this is detailed in the following section to determine the useful range of field measurement in the spectral domain and the attainable source mapping resolution.

2. Equation (2.7) is a Fourier transform relation which indicates that the determination of the modal fields over the spectral domain is equivalent to the determination of the space dependent fields. While this is mathematically correct, it will be shown in Section (2.6) that an under-sampling problem may exist when dealing with the spectral domain expressed as discrete data.

2.4. Source Mapping Limitations:

Practical considerations have to be taker into account in estimating the limitations in mapping the sources. As will be discussed in Chapter Three, the nature of the measuring probes, usually, allows high resolution measurement of only those two components of the field that are tangential to the plane of measurement, when a single probe is used. The measurement of the normal component involves the use of a different probe. Accordingly, the following three cases can be distinguished:

1. Calculation of equivalent magnetic current distribution from two measured tangential electric field components. The same conclusions apply to the dual case of calculating the equivalent electric current distribution from two measured tangential magnetic field components.

2. Calculation of equivalent electric current from two measured tangential electric field components. The same conclusions apply, also, to the dual case of calculating the equivalent magnetic current distribution from two measured tangential magnetic field components.

3. Calculation of equivalent electric or magnetic current from three measured electric or magnetic field components.

It will be shown below that cases (1) and (3) are equivalent. In the following sub-section, the mapping limitation for the first case is examined, and in the subsequent sub-section, the second case is considered.

2.4.1. Magnetic Current Source Model from Measurement of two Tangential Electric Field Components and the Dual Case:

Referring to Equation (2.5-a), it appears that only the two tangential electric field components may need to be used to determine the equivalent magnetic currents. The z (normal) component is especially noise sensitive, since it is weakly coupled to the source currents, as evident from the third row of the matrix in the same equation. The measurement of this component, therefore, is not necessary. If the three components of the magnetic field are measured, the electric field can be calculated directly using Maxwell equation $\nabla \times \vec{H} = j\omega\epsilon \vec{F}$ for each mode. The conclusions from this case, therefore, apply to the first and the third cases listed above.

The measurement errors component in the measured electric field is $\vec{\epsilon}_e = \hat{x}\epsilon_{ex} + \hat{y}\epsilon_{ey}$, and the resulting error in estimating the equivalent magnetic current is $\vec{\epsilon}_m = \hat{x}\epsilon_{mx} + \hat{y}\epsilon_{my}$. The relation between their magnitudes from Equation (2.5-a) is:

$$|\vec{\epsilon}_m| = e^{jk_z d}|\vec{\epsilon}_e| \qquad \ldots.(2.8)$$

To establish the limits of the usable range of modes (k_x, k_y), for use in calculating the currents, it is useful to express the tangential wave numbers as:

$$k_x = k_t \cos\Psi$$

$$k_y = k_t \sin\Psi$$

where $k_t^2 = k_x^2 + k_y^2$. The wave number k_t is then the magnitude of the tangential wave number for the mode (k_x, k_y) and Ψ is its direction.

Using the relation between the three wave number components indicated in Equation (2.4), the normal wave number k_z can be expressed as:

$$\begin{aligned} k_z &= \sqrt{k_o^2 - k_t^2} \quad \text{for} \quad k_t < k_o \\ k_z &= -\sqrt{k_o^2 - k_t^2} \quad \text{for} \quad k_t > k_o \end{aligned} \qquad \ldots(2.9)$$

The above two cases indicate radiating and evanescent modes respectively. Equation (2.8) can be rewritten as:

$$|\vec{\epsilon}_m| = T(k_t, d)|\vec{\epsilon}_o| \qquad \ldots(2.10)$$

where:

$$T(k_t, d) = 1 \quad \text{for} \quad k_t < k_o$$

$$T(k_t, d) = e^{-j\sqrt{k_t^2 - k_o^2}\,d} \quad \text{for} \quad k_t > k_o$$

It is obvious from the above relation that the field-current transformation is well-conditioned for the radiating modes, while the possibility of ill-conditioned transformation arises only for the evanescent modes, and is dependent on the distance d.

To set a criterion for the maximum acceptable measured tangential mode k_{tmax}, a mode is considered usable in transformation if the error power in the calculated currents does not exceed twice that of the error in the mode ($k_x = k_y = 0.$) (i.e. $k_t = 0.$) for the same measurement noise power. In other words:

$$T(k_{tmax}, d) = e^{-j\sqrt{k_{tmax}^2 - k_o^2}\,d} = \frac{1}{\sqrt{2}}$$

By manipulating the above equation and expressing the distance as $d_\lambda = d/\lambda$:

$$k_{tmax} = \frac{k_o\sqrt{d_\lambda^2 + \left(\frac{\ln 2}{4\pi}\right)^2}}{d_\lambda} \qquad \ldots(2.11)$$

Figure (2.4) shows the relation between the maximum tangential wave number and the distance in wavelengths between the equivalent currents and measurement planes. It can be seen that the evanescent modes are useful only in the proximity of the radiator surface while k_{tmax} approaches k_o as the distance gets larger. The dashed curves in Figure (2.4) shows the maximum attainable k_{tmax} when the error power is allowed to multiply by four and eight, respectively, instead of the above mentioned double power

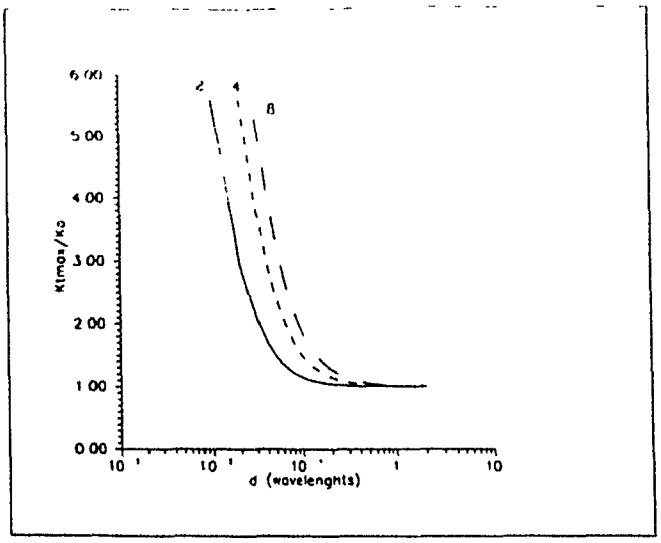

Figure (2.4): Maximum tangential wave number of the equivalent currents (k_{imax}/k_o), versus the distance d_λ, in wave lengths, between the equivalent currents and measurement planes.

Solid curve: noise power multiplied by a maximum of two.

Dashed curves: noise power multiplied by maximum of four and eight.

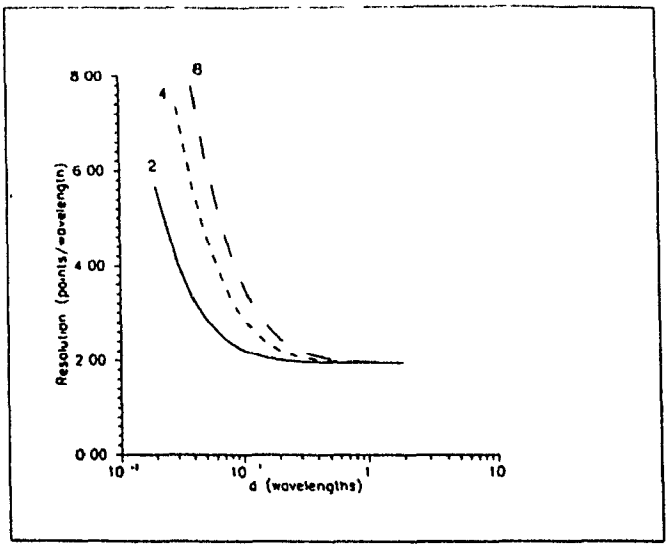

Figure (2.5): Equivalent currents mapping resolution for maximum noise power multiplication of two, four and eight.

The resolution is defined here as the maximum distinguishable number of points per wavelength.

criterion. These represent different levels of measurement errors and noise significance compared to the original field contribution. By inspecting the three curves, it can be concluded that the evanescent mode measurement is possible only for d on the order of 0.1λ. Strong interaction between the radiator and the measuring field probe is highly possible in this case.

Since k_{tmax} is the highest radial spectral frequency component of the mapped radiator current distribution, it can be used to define the attainable resolution of that distribution. The first step in doing so is to find out how a magnetic current ideal point source at $x' = y' = 0$ would be mapped, with the constraint of k_{tmax}. The point source, being an impulse in the space domain, has a constant spectral response over the entire spectral domain. With the limitation of a maximum measurable tangential wave number imposed by Equation (2.11), the space domain measured point source $R(x', y')$ is by Fourier transformation:

$$R(x', y') = \int\int_{k_t < k_{tmax}} e^{-j(k_x x' + k_y y')} \frac{dk_x dk_y}{4\pi^2}$$

Expressing the space variation in terms of the radial distance from the origin r' instead of the rectangular coordinates x', y', to account for the radial symmetry of the space response, and integrating along r':

$$R(r') = k_{tmax} \frac{J_1(k_{tmax} r')}{2\pi r'} \qquad \ldots(2.12)$$

As a measure of the resolution, one can consider that two point sources on S', separated by a distance r'_{min} are distinguishable, if the response of either of them decays to, at least, half power at the location of the other point. In this case the resolution can be defined as the maximum number of distinguishable point sources per wavelength on the radiator plane. According to the definition used here, a higher resolution number indicates a better resolution. This criterion is used in plotting the results in Figure (2.5), which relates the attainable mapping resolution to the distance between the measurement and the antenna surfaces. The solid curve corresponds to a permissible measurement noise power multiplication of two, while the dashed curves are for noise power multiplication of four and eight respectively. It can be seen that except for small distances ($d_\lambda < .1$), the resolution approaches 2 points/wavelength, independent of d_λ.

2.4.2. Electric Current Source Model from Measurement of two Tangential Electric Field Components and the Dual Case:

This is the second case indicated in the beginning of this section. In this case Equation (2.5-b) applies to relate the electric currents to the two measured components of the electric field, excluding the last row of the matrix in this equation. By duality, similar relation applies to relate the measured magnetic field components and the equivalent magnetic currents representing the radiating sources, except that ϵ is replaced by μ. Excluding the last row of the matrix in Equation (2.5-b), it can be used to relate the error in the calculated electric current $\vec{\epsilon}_j$, to the errors in the measured field $\vec{\epsilon}_e$, as follows:

$$\begin{bmatrix} \epsilon_{ex} \\ \epsilon_{ey} \end{bmatrix} = \frac{k_o^2 e^{-jk_z d}}{2\omega c k_z} \begin{bmatrix} 1-\left(\frac{k_x}{k_o}\right)^2 & -k_x k_y \\ -k_x k_y & 1-\left(\frac{k_x}{k_o}\right)^2 \end{bmatrix} \begin{bmatrix} \epsilon_{jx} \\ \epsilon_{jy} \end{bmatrix} \qquad \ldots.(2.13)$$

The matrix in the above equation has two distinct eigenvalues:

$$\lambda_1 = \frac{k_o^2 e^{-jk_z d}}{2\omega c k_z}$$

$$\lambda_2 = \frac{k_z e^{-jk_z d}}{2\omega c}$$

As was done in Equation (2.10), the field and current errors can be related such that:

$$|\vec{\epsilon}_j| = T(k_t, d)|\vec{\epsilon}_e| \qquad \ldots.(2.14)$$

For a certain mode, the minimum value of T in the above equation is $1/\lambda_1$, and the maximum value is $1/\lambda_2$ which corresponds to the worst case of noise multiplication, and is considered in evaluating k_{tmax} for this case. Using the same criterion as in Equation (2.11), the maximum tangential wave number for which the source electric current density can be measured is:

$$k_{tmax} = \frac{k_o}{\sqrt{2}} \qquad \ldots.(2.15)$$

The resolution can be found in a similar fashion as the previous sub-section using the above k_{tmax}. The source mapping resolution for the cases of this sub-section is far lower than that of the cases of the previous sub-section. It will be shown in the next chapter, however, that a proper choice of the measuring probe will enable a high resolution measurement of the tangential components of the desired field type. This will facilitate dealing with only the cases of the previous sub-section, and will result in relatively high resolution equivalent current mapping at the source plane.

The following table lists a summary of the results of this section:

Measured field type	Number of components*	Equivalent Current type	Resolution**
Electric	Two	Magnetic	High
	Two	Electric	Low
Magnetic	Two	Electric	High
	Two	Magnetic	Low
Electric or Magnetic	Three	Electric or Magnetic	High

* *Two* measured components are tangential to the plane of measurement

** *High* resolution is defined using Equation (2.11), and *Low* resolution is defined using Equation (2.15).

2.5. Experiment Design and Field Sampling Criterion:

The design of an experiment is highly dependent on the nature of the radiator under test and the accuracy required in field mapping. The factors to be determined when designing a measurement are; the distance d between the radiator and the surface of measurement, the dimensions of the measurement surface, the sampling spacing of the measurement points and the field probe to be used. The last factor is considered in detail in the next chapter

The choice of the distance d between the radiator and the measurement plane depends on the objective of the measurement. If the measurement is intended to investigating the qualitative immediate field behavior of the radiator with high resolution, the distance d should be as small as possible, so that k_{tmax} described by Equation (2.11) is large enough to give high resolution to the mapped radiator currents Figure (2.4) shows that d has to be in the order of 1λ, so that the evanescent modes contributed by the fine details of the current distribution can be detected. The fact that the evanescent modes are measured, implies that there is strong interaction between the measurement probe and the reactive field of the radiator under test This makes such a measurement inadequate for quantitative evaluation of the radiator immediate field, especially in narrow bandwidth radiators such as a resonant microstrip patch, but very useful for qualitative purposes. It should be mentioned here that a distance too close to the radiator in not always enough to gain a high mapping resolution of the source currents, since, as will be seen in Chapter Three, the probe is able to measure the field components up to a certain maximum tangential wave number depending on the size of the probe, so that close proximity of the probe might not increase the mapping resolution.

When a quantitative accuracy is required for the mapped field, it is logical to increase the distance d, typically to more than a wavelength[3] to avoid mutual interaction, or multiple scattering, between the radiator and the field probe At such a distance, the evanescent modes have decayed enough to be too small to be measured, and k_{tmax} will equal to k_o as demonstrated by Figure (2.4). This means that the larger d implies dealing with only the radiating (or visible) modes, which will limit the attainable field resolution.

The choice of the dimensions of the plane of measurement is such that the field magnitude exterior to that plane is below the sensitivity level of the measuring instruments. This implies that this field is considered zero in the subsequent measurement data processing. This will also limit the number of data points to a manageable amount. As the distance d is increased, the radiator will "illuminate" a larger area on the plane of measurement. This will necessitate a choice of larger dimensions of

the measurement plane, and subsequently a larger measurement facility and more data points with the benefit of less mutual interaction between the radiator and the field probe.

From the above discussion, it seems that the logical way of setting the distance d and the measurement plane dimensions is to conduct several trial scans to gain some idea about the radiator field structure, before attempting to perform a final measurement.

The remaining factor in designing a measurement is the choice of the spacing τ between the measurement points. Starting from the definition of Nyquist rate[44] as the minimum sampling rate at which a band limited signal can be completely reconstructed from a sampled one, which equals twice the maximum frequency content of that signal, and using the fact that the tangential wave number is the radial spatial frequency of the field (Equation (2.3)), the sampling spacing can be defined as:

$$\tau \leq \frac{1}{2 f_{tm}} = \frac{\pi}{k_{tm}} \qquad \ldots.(2.16)$$

where k_{tm} is the maximum *detectable* mode tangential wave number, which is different from k_{tmax} defined earlier and $f_{tm} = k_{tm}/2\pi$. Choosing a larger sampling space will cause distortion in the Fourier transformed field representation and subsequently the mapped current due to frequency aliasing[45].

When a part the measurement plane is located in the evanescent region of the radiator, there is no way to predict the maximum detectable field mode, since the original currents contributing to the evanescent modes are unknown. The best way is probably to over-sample the field for this case, so that the field with significant magnitude will be confined to a small area of the plane of measurement This will enable a choice of a smaller dimension plane of measurement and a manageable number of data points. On the other hand, when the measurement plane is totally located in the radiation region of the radiator $d > \lambda$, the maximum detectable tangential mode is k_o, and in this case, the sample spacing is:

$$\tau \leq \frac{\pi}{k_o} = \frac{\lambda}{2} \qquad \ldots.(2.17)$$

The duality between the Fourier transformation and its inverse implies that the Nyquist rate can be used to specify the spectral domain sampling rate, based on the measurement plane dimension. The sample spacing in the spectral domain (Δk_x and Δk_y)

can be expressed in terms of W_x and W_y, the plane of measurement dimensions, as:

$$\Delta k_{x,y} = 2\pi / W_{x,y} \qquad \ldots.(2.18)$$

Exceeding this spacing will cause distortion in the mapped current due to under-sampling, while selecting a lower value will result in an unnecessarily large amount of spectral domain data. It is worth mentioning at this point that the sampling rate specified in the above equation is necessary to preserve the space domain information, but is not always useful for the numerical evaluation of the space domain data using Fourier transformation as will be clarified in the next section.

It seems that the choice of the measurement dimensions, distance and sample spacing is a matter of experience that can be gained by investigative experiments and by considering the nature of the radiator itself. For example in determining the distance d, a narrow-band (high Q) radiator, such as a resonant microstrip patch, is expected to be more internally influenced by the presence of the measuring probe than a wide-band horn antenna This is attributed to the fact that a high Q of an antenna indicates that a large proportion of the field energy in and around the antenna region is reactive (stored energy), which is represented in the modal expansion by the evanescent modes. This can lead to the possibility of measuring evanescent modes in close proximity of the radiator, but consequently indicating that a small d means significant interaction between the radiator and the measuring probe These judgements are applied in Chapter Four, in which all the experimental work directed towards source mapping was preceded with preliminary field probing to gain some idea about the field structure.

2.6. Experimental Evaluation of the Near-Field:

One purpose of defining the equivalent radiating currents is to define the field in the vicinity and around the radiator, i.e the external field. A question may arise in this context about the necessity of dealing with the equivalent sources; since the plane wave spectral representation of the field is available from measurement, why not mapping the near-field region directly from spectral domain data using Fourier transformation? This was attempted using real measurement data, and it was found that determining the mapped field was unsuccessful and yielded extremely noisy results. Calculating the near-field from the equivalent radiating currents, using Equation (2.1), proved successful as shown in Section (4.3). Explaining this phenomena is important in exploring

the limitations involved in using the plane wave spectrum, particularly considering the fact that the spectral domain representation is adequate in calculating the immediate field and the far-field of the radiator under test.

The explanation starts by expressing the space domain electric field in terms of the plane wave spectrum $\vec{E}(k_x, k_y)$. transformed into the radiator surface, using Fourier transformation:

$$\vec{E}(x,y,z) = \frac{1}{4\pi^2}\int_{-\infty}^{\infty}\int_{-\infty}^{\infty}\vec{E}(k_x,k_y)e^{-j(k_x x+k_y y+k_z z)}dk_x dk_y \qquad \ldots.(2.19)$$

Transforming into spherical coordinate system $\vec{r}(r,\theta,\phi)$:

$$\vec{E}(\vec{r}) = \frac{1}{4\pi^2}\int_{-\infty}^{\infty}\int_{-\infty}^{\infty}\vec{E}(k_x,k_y)e^{-j\vec{k}\cdot\vec{r}}dk_x dk_y \qquad \ldots.(2.20)$$

where $\vec{r} = r(\hat{x}\sin\theta\cos\phi + \hat{y}\sin\theta\sin\phi + \hat{z}\cos\theta)$, and the phase term is:

$$\vec{k}.\vec{r} = r\hat{r}.\left(\hat{x}k_x + \hat{y}k_y + \hat{z}\sqrt{k_o^2 - k_x^2 - k_y^2}\right) \qquad \ldots.(2.21)$$

It is evident from the above equation that the phase term variation in Equation (2.20) is proportional to r as the integration is performed over the radiation region in the spectral domain. For small values of r, this term is slowly varying and the integral can be numerically evaluated with a moderate spectral domain sampling rate. This is the reason why the Fourier transform is adequate for evaluating the equivalent currents. As r grows larger within the near-field region, but not large enough into the far-field, the phase term will change faster with respect to the spectral variables. This requires very small sampling intervals in the numerical integration of Equation (2.20), and the major contribution to the integral will be from the integration of a small area around the stationary phase point[46], while the contribution is supposed to average to zero for the rest of the spectrum. In the far-field, the field is evaluated directly from a single point in the spectral domain for each direction of propagation, since the integral can be approximated analytically using the method of stationary phase[10]. The far-field evaluation, therefore, does not encounter the undersampling problem because it does not involve numerical integration to begin with.

The approach used in this work was to use the spectral domain data to evaluate the equivalent radiating current, using the theory presented in this chapter, and from that, the near-field is evaluated using the space domain relations of equations (2.1) and (2.2). This approach has the advantage of added efficiency when dealing with small radiators because the equivalent currents are confined to a small region around the radiator physical aperture, requiring a small number of integration points.

The near-field as opposed to the immediate field, contains only radiating modes. This suggests that for the purpose of evaluating the near-field, only the radiation region needs to be considered in finding the equivalent radiating currents. This implies that the equality in Equation (2.17) can be used to define the space domain sampling rate of the equivalent currents when using equations (2.1) or (2.2).

It is possible here to define the steps for evaluating the exterior field distribution from planar near-field data. These steps are shown in the block diagram of Figure (2.6).

2.7. On Measurement Errors Sources and Contribution:

One of the purposes of the near-field measurement in this work is to obtain quantities which represent the radiation behavior of the radiator under consideration. In the commonly used spectral domain representation, the weight of each discrete mode is extracted from the near-field measurement data, so that it can be used to evaluate the fields exterior to the radiator, within the limitations discussed in the previous section. The equivalent currents, considered here, are an alternative space domain representation of the radiation behavior.

The errors in these representations will result in reduced accuracy in evaluating the external fields of the radiator. In this section the sources of errors are defined, and the effect of these errors on each representation is estimated, particularly for non-directive radiators. Considerations for highly directive radiators are discussed in detail by Newell[47].

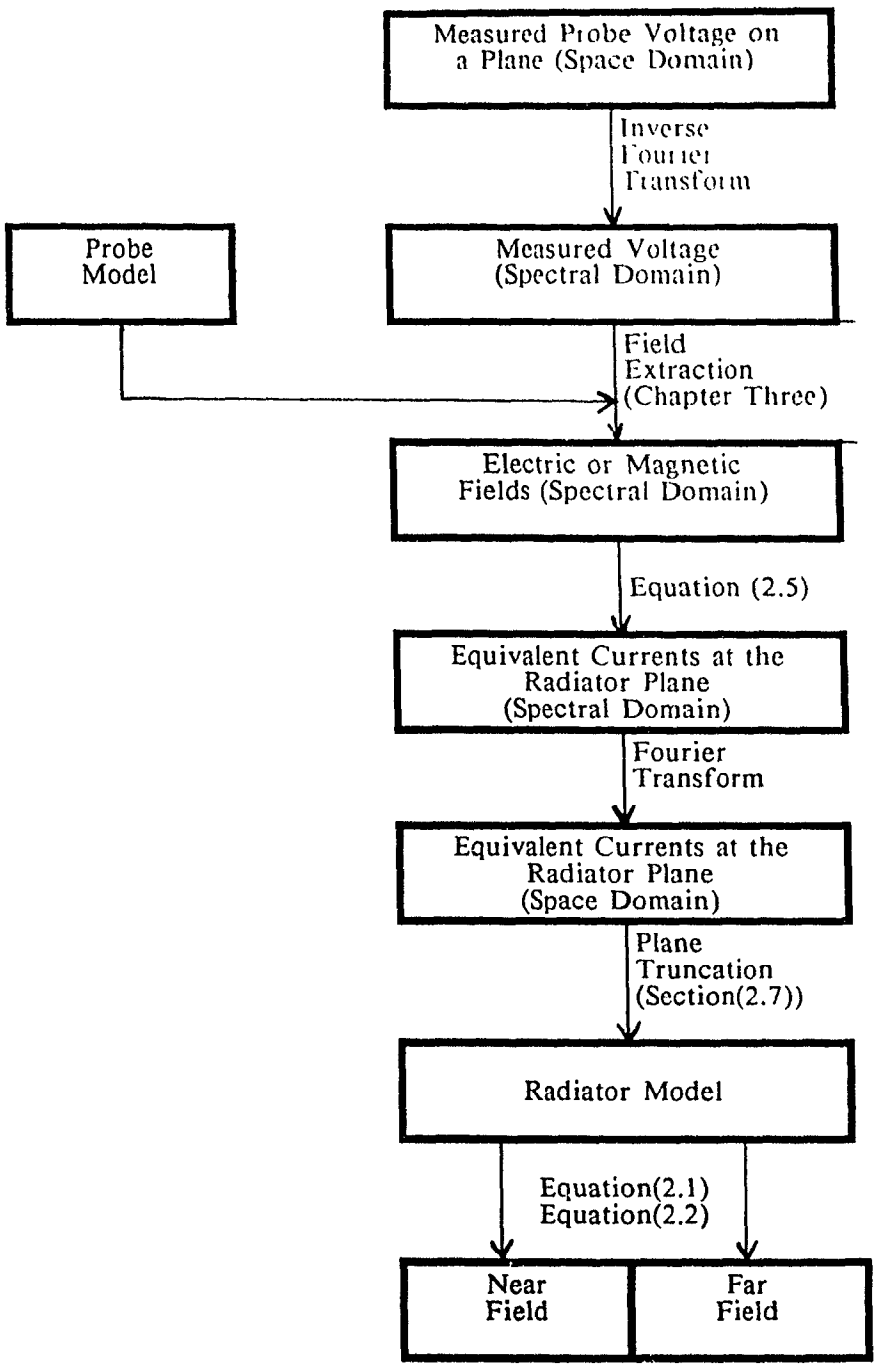

Figure (2.6): A block diagram of the suggested processing sequence of the planar measurement data to obtain the near-field or the far-field distribution.

2.7.1. Sources of Errors in the Equivalent Currents:

The common source of errors in any measurement is the *random* errors encountered due to noise from the measuring instruments and circuits, and the quantization error when digitizing the measured samples. These errors can be minimized by improving the quality of the measuring instruments, reading multiple samples at a point and increasing the quantization levels. Random errors are uniformly distributed throughout the points on the plane of measurement. The inverse Fourier transformation results also in uniform distribution of these errors over the spectral domain. When the evanescent modes are considered, this type of error becomes the limiting factor in source mapping resolution.

There are other types of errors that can be assumed to behave in a similar fashion, i.e. uniformly spread over the spectral domain, such as random probe position error, amplitude and phase nonlinearity, the effect of variation in measurement environment, such as temperature and frequency. The logic behind this assumption is that there is no reason why these errors should accumulate in one or a few spectral components, therefore, these errors can be treated as random errors.

The types of errors discussed above differ from other types which tend to accumulate in certain spectral components or within a small region in the spectral domain, affecting noticeable distortion on the plane wave spectrum representation at these regions. For this reason, these alternative types of errors are called here *spectral* errors. The leakage from the cables and joints of the radiator feed circuits and guides is an example of these errors. Since the leakage points are relatively far from the plane of measurement, they produce nearly a plane wave, originating from the leakage direction, at this plane. Transforming the measured data into the spectral domain will result in the accumulation of the leakage error on specific and neighboring spectral components. Because of this error accumulation, it can be significant compared to the contribution of the radiator under test, even though it might not be noticeable in the space domain data. The same discussion applies to scattering from the surroundings within the measurement facility. These errors can be minimized by careful setup and shielding of the radiator feed, and by using high quality absorbers in the anechoic chamber enclosing the measurement facility.

The coupling, or cross-talk, between the reference channel and the reference channel of the network analyzer, Appendix (C), used in measuring the amplitude and phase of the measurement probe will produce a constant error component over the plane of measurement. This will accumulate in the spectral domain only at the component $(k_x = k_y = 0)$ which corresponds to the plane wave travelling along the boresight direction away from the radiator.

Leakage and coupling errors are more significant in non-directive radiator measurement, because the radiated power is spread over a broad solid angle, which makes the local distortion of the spectral domain more observable.

One of the error sources that is specific to the non-directive radiator is the truncation of the measurement plane. This source of error was mentioned by Yaghjian[3] as a limiting factor in applying planar near-field measurement to broad-beam antennas. The explanation given in the same reference about the effect of truncation on an antenna with an end-fire radiation response, is that this response will decay asymptotically as $e^{-jk_o r}/r$, where r is the distance between the radiator and the extremity of the measurement plane. The measured field can decrease to a negligible quantity at points on the boundary of the plane of measurement Considering the above radiator response, the integral of the boundary measured points around the plane of measurement has a finite value even if the area of the measurement plane is extended to infinity. This phenomenon will cause an error in the $(k_x = k_y = 0)$ component in the spectral domain, that oscillates with increasing the area of the plane of measurement.

An alternative presentation of the mechanism causing this error is presented here, which may facilitate better understanding. The truncation of the plane of measurement can be considered as equivalent to multiplying the original field $\vec{E}(x,y)$ over an infinite plane of measurement by a window function $W(x,y)$, which equals unity within the actual plane of measurement and vanishes outside that plane. The measured field, $\vec{E}_m(x,y)$, can be expressed as:

$$\vec{E}_m(x,y) = W(x,y)\vec{E}(x,y) \qquad \ldots.(2.22)$$

The inverse Fourier transform will result in the expression of the above equation in the spectral domain as:

$$\vec{E}_m(k_x,k_y) = \int\int W(k'_x,k'_y)\vec{E}(k_x+k'_x,k_y+k'_y)dk'_x dk'_y \qquad \ldots.(2.23)$$

which shows that the effect of plane of measurement truncation is the distortion of the measured spectrum caused by convolution with the window spectrum. A theoretical evaluation of the spectral domain field of a broad-beam radiator, such as an elementary dipole, shows that the spectral representation is singular on the perimeter of the radiation circle, $(k_x^2 + k_y^2 = k_o^2, k_z = 0.)$. The rectangular window function can be expressed in the spectral domain as:

$$W(k_x,k_y) = 4W_x W_y sinc(k_x W_x/2)sinc(k_y W_y/2) \qquad \ldots.(2.24)$$

where W_x and W_y are the measurement plane dimensions defined in Section (2.5).

The window function spectrum has a main lobe centered at $k_x = k_y = 0$. and side lobes whose amplitude decay away as $1/k_x k_y$. The use of the spectral domain sampling rate of Equation (2.18) will result in zero coupling between adjacent points in the k_x and k_y directions, because of the first null in the window function spectrum. The significant error contribution is the coupling between the singularity in the field spectrum described above, and the field spectrum within the radiation circle. This coupling seems to add coherently at the $k_x = k_y = 0$ spectral component, which results in field spectrum distortion at this point. This error can be classified as spectral error as in the case of the leakage and coupling errors, but it differs from the other two by the fact that it originates from the measurement configuration rather than from apparatus imperfections.

The spectral errors can be a limiting factor in evaluating the near or the far fields directly from the plane wave spectrum, because this evaluation involves the use of small range of propagating modes[25] to evaluate the near-field, or a point in the spectral domain to evaluate the far-field. The evaluated field will suffer an observable distortion if a point or region containing spectral error is used in this evaluation.

2.7.2. Error Contribution to the Equivalent Current Model:

In this sub-section, it is shown that the use of equivalent current model of a radiator results in a reduction of the effects of measurement errors. The amount of this reduction is estimated here. As shown in Figure (2.6), the evaluation of these currents involves a transformation to the spectral domain, then a transformation into spectral equivalent currents at the radiator equivalent plane, and finally transformation back into the space domain. The error under consideration is, therefore, normalized at each stage to the power of the unperturbed contribution from the radiator under consideration.

The measured field $\vec{E}_m$ can be decomposed into three components:

$$\vec{E}_m(x,y) = \vec{E}(x,y) + \vec{\epsilon}_r(x,y) + \vec{\epsilon}_s(x,y) \qquad \ldots.(2.25)$$

where $\vec{E}$ is the contribution from the radiator, $\vec{\epsilon}_r$ is the contribution of the random errors, and $\vec{\epsilon}_s$ is the contribution of spectral errors defined in the previous sub-section. x and y are within the truncated plane of measurement.

The distance between the plane of measurement and the radiator is assumed to be large enough so that only the propagating modes contribute to the measured field. This assumption is a consequence of the discussion in Section (2.5) dealing with the selection of that distance. The transformation into the spectral domain, therefore, will restrict the radiator contribution to within the radiation circle shown in Figure (2.7-a). The spectral error will increase, due to the measurement plane truncation error described earlier, by an amount that depends on the dimensions of the plane of measurement and the original field structure of the radiator, as evident from Equation (2.23). The spectral domain will retain all the space domain information if the sampling rate of Equation (2.18) is used and the range of the spectral variable is within:

$$-\pi/\Delta x \le k_x \le \pi/\Delta x, -\pi/\Delta y \le k_y \le \pi/\Delta y \qquad \ldots.(2.26)$$

where Δx and Δy are the x and y spacing between samples. The above range of the spectrum is one of the properties of the discrete Fourier transform[45].

The truncation of the spectral domain, by setting to zero all the modes outside the radiation circle, will filter out the portion of the random error component which is outside this circle. Since this error is uniformly distributed over the spectral domain, error power will be reduced proportionally due to this truncation. The error contribution will be reduced to the ratio of the radiation circle area to the area of the domain of the spectral variable described by Equation (2.26). This ratio from Figure (2.7-a) is $k_o^2 \Delta x \Delta y / 4\pi$. This truncation neither affects the original radiator field nor the spectral noise component because both have their spectrum confined mainly to within the radiation circle.

The transformation of the fields backward into equivalent radiating currents will not modify the nature of the errors if the current type is chosen properly, as evident from Equation (2.5-a), in which k_z is real for the propagating modes under consideration. This means that these modes will only encounter phase change by this transformation.

The transformation of the currents into the space domain at the equivalent current plane will not change the relative power of the errors, and the area in the space domain that contains the truncated spectral domain has the same dimensions and origin as that of the plane of measurement. This is based on the assumption that Equation (2.18) is used in sampling the spectral domain, and on using the properties of the discrete Fourier transform. It is expected that the unperturbed equivalent radiator currents will be

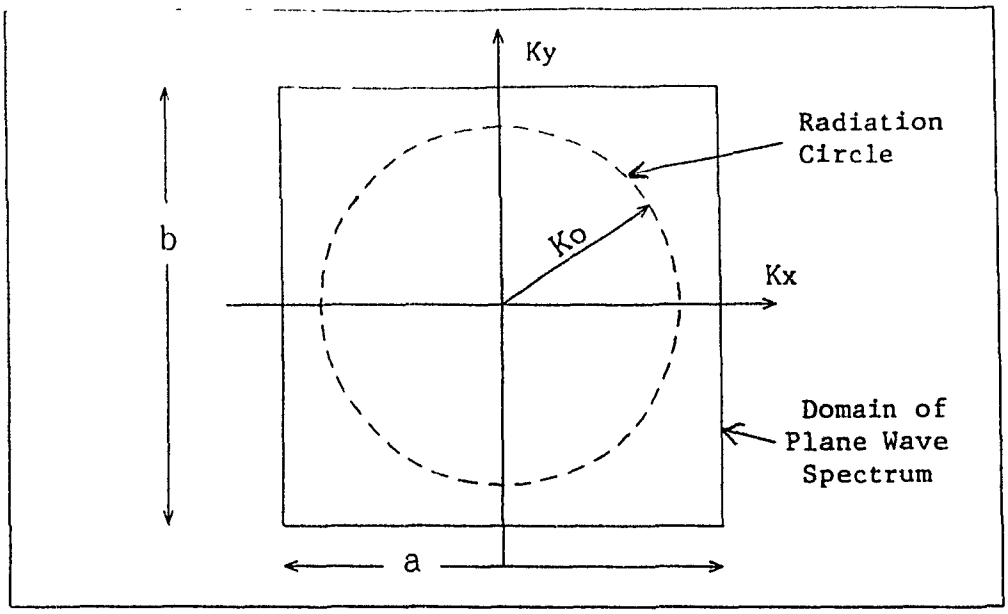

Figure (2.7-a): Spectral domain truncation. Only modes within the radiation circle are considered. The measurement information are spread over a rectangular area of dimensions $a = 2\pi/\Delta x$ and $b = 2\pi/\Delta y$.

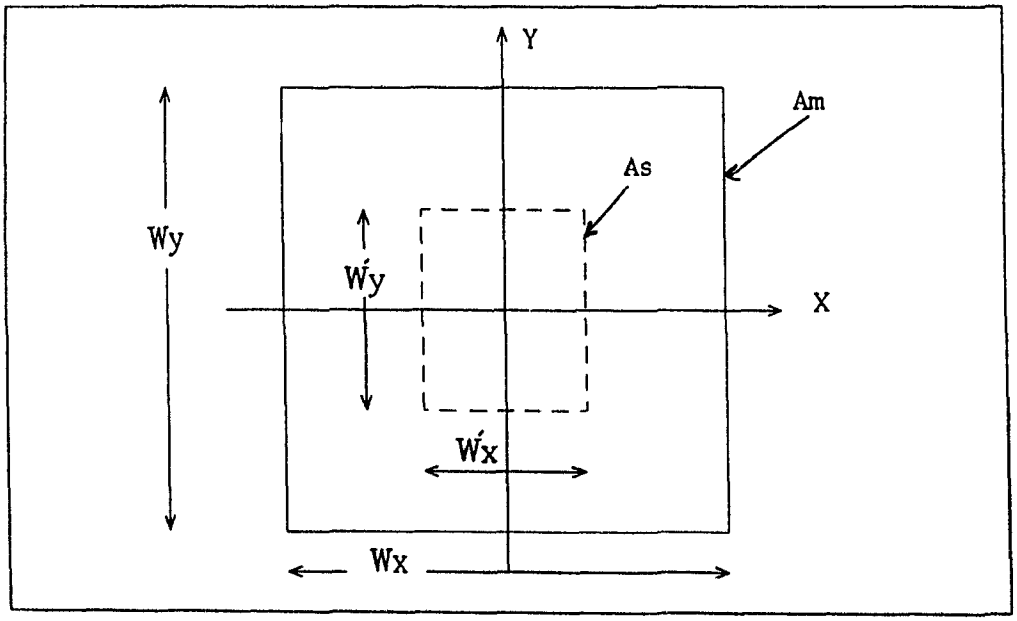

Figure (2.7-b): Equivalent current plane truncation. Only equivalent currents on and around the radiator aperture are considered for exterior field calculations. ($A_m = W_x W_y$ and $A_s = W_x' W_y'$).

confined to an area A_s on and around the physical aperture of the radiator. On the other hand, the contribution of the errors, random and spectral, is expected to be uniformly distributed over the area of the equivalent current plane A_m with dimension W_x and W_y. The truncation of the equivalent radiating current plane to include only A_s. (= W'_x X W'_y, as shown in Figure (2.7-b)), will effect a reduction of the relative error power by the ratio of this area to the area of the original plane of measurement, i.e. A_s / A_m, without significant effect on the original sources.

In summary the error power is attenuated by the ratios R_r and R_s for random and spectral error types respectively, by using the truncated equivalent current model. These ratios can be expressed as:

$$R_r = \frac{k_0^2 \Delta x \Delta y A_s}{4\pi W_x W_y} \qquad \ldots.(2.27-a)$$

$$R_s = \frac{A_s}{W_x W_y} \qquad \ldots.(2.27-b)$$

The relative error power, ϵ_{tot}, in the truncated equivalent current model is, therefore:

$$\epsilon_{tot} = \frac{A_s}{W_x W_y}\left(\epsilon_s + \frac{k_0^2 \Delta x \Delta y}{4\pi}\epsilon_r\right) \qquad \ldots.(2.27-c)$$

Where ϵ_s and ϵ_r are the original spectral and random error power components respectively prior to the spectral and space domain truncations.

Two points have to be emphasized concerning the effect of space domain truncation of the equivalent currents:

1. The aperture area of a non-directive radiator is usually small compared to the area of the plane of measurement. This makes such a truncation effective in filtering out the measurement errors, in comparison to corresponding measurements on directive antennas, where the area of the measurement plane is comparable to the effective aperture area of the antenna[3].
2. It was pointed out in the previous sub-section that the problem with the spectral errors is that they tend to accumulate on certain modes. The truncation of the equivalent currents plane will, in addition to reducing the relative error power, smear the error in the spectral domain, which will further reduce its peak value in this domain. For

example, if a relative coupling error of $\vec{\epsilon}_{DC}$ is superimposed on the measured field at the measurement plane, its contribution in the spectral domain is similar to the window function of Equation (2.24), and will be:

$$\vec{\epsilon}_{DC}(k_x, k_y) = 4\vec{\epsilon}_{DC} W_x W_y \, sinc(k_x W_x/2) \, sinc(k_y W_y/2)$$

whereas the field spectrum from the equivalent currents, under the assumption that the equivalent current truncated plane dimensions of W'_x and W'_y, is:

$$\vec{\epsilon}'_{DC}(k_x, k_y) = 4\vec{\epsilon}_{DC} W'_x W'_y \, sinc(k_x W'_x/2) \, sinc(k_y W'_y/2) \qquad \ldots.(2.28)$$

From the above two relations, it can be concluded that the peak error in the spectral domain fields is reduced by A_s/A_m, while the r.m.s. error for the same component is $\sqrt{A_s/A_m}$, as evident from Equation (2.27-b), where A_s and A_m are the truncated equivalent currents plane and the measurement plane areas, respectively. This further reduction in the peak error comes from the broadened spectral response demonstrated by the above two equations. The same argument applies to the remaining spectral errors, such as the leakage and truncation errors described in the previous sub-section.

2.8. Concluding Remarks:

In defining a procedure for the measurement and the subsequent data processing to determine the equivalent current distribution on a radiator surface, this chapter introduced possible models for such equivalent radiating currents. These models are constrained to tangential currents on a planar radiator equivalent surface. In addition, *either* electric *or* magnetic currents were considered. It is apparent that the problem of mapping the currents directly from the measured field is an ill-posed inverse problem. It is possible, however, to use the modal expansion of the field to formulate a well-posed source mapping procedure This is at the expense of limited mapping resolution. The planar measurement design is discussed in the context of defining the measurement plane dimensions, the distance from the radiator and the sample spacing. Some of these factors are quite indeterminate beforehand and it is concluded that several investigative measurements need to be conducted before undertaking a final measurement.

Based on computer simulation, Wang[48] suggested larger sampling intervals than that implied by Equation (2.17) when the radiator is highly directive. The analysis of this chapter and the experimental results of Chapter Four contr this suggestion. In the case of practical measurements, sampling intervals larger than $\lambda/2$ may incur the danger of aliasing, and will introduce distortion in the spectral domain when an unknown and

unpredicted behavior of a radiator is encountered. This implies that Equation (2.17) defines the absolute maximum sampling interval for a measurement conducted in the radiation region of the antenna under test.

This chapter has demonstrated and explained the difficulty of evaluating the space domain near-field directly from the plane wave spectrum, and an alternative approach is suggested. This approach employs space domain integration of the equivalent radiating currents over the radiator aperture. This technique is applied in Chapter Four for evaluating the near-field quantities of antennas using planar near-field measurements.

The classification of measurement errors into two types, random and spectral, according to the behavior of the error type in the spectral domain, facilitated the estimation of error power and peak reduction for each error type, using the equivalent currents model of the radiator. The basic factors affecting the error power reduction is the exclusion of the noisy areas in the spectral domain and similarly in the equivalent current plane. It was shown that the second factor can be effective for error reduction in non-directive radiators, because of their small aperture area.

The consideration of near-field measurement is not complete without examining the effect of the field probe on the measurements. The behavior of the probes, the interpretation of their electrical output and their influence on the near-field measurement process is the subject of the following chapter.

CHAPTER THREE

MEASUREMENT PROBE CONSIDERATIONS

This chapter deals with the problem of determining the effects of the probe on the measurement of the field, and the methods of accounting for these effects. The name commonly given in the literature[3,34] for such a procedure is *Probe Correction*, and this term was previously used by the author[39,40]. It can be argued that the effect of the probe on the measurement is by no means an "error" which needs "correction", it is simply part of the measurement apparatus which should have a contribution to the measurement data It will be shown later that the field values can be extracted accurately from the measured data, if there exists an exact model of the probe. The only *errors* involved arise from the approximations made in determining the probe model. The term used in this work, therefore, is *field extraction*, which can be defined as the extraction of field quantities from measured probe output voltage.

The derivations and formulae introduced in this chapter aim at the determination of the field quantities at the plane of measurement from the measured probe output voltage. The main purpose is then to evaluate the equivalent current sources. In addition, the extracted field values can be used to calculate the far-field directly. No specific assumptions are made about the nature of the measured field. Available literature published about *probe correction*, for example, generally presume that highly directive radiators are being measured, and only in the radiation region. On the other hand, certain assumptions are made in this chapter about the probes themselves. These include; linearity, reciprocity and single frequency operation.

3.1. Formulations for a General Probe:

When the electric or magnetic field measurement is attempted, the measured phasor voltage is expected to be proportional to a weighted average of the incident field over the probe surface. An assumption of a probe with finite volume, and made of materials that have linear electromagnetic parameters is made here. This means that a practical probe cannot measure the field at a point, because it has to have a finite volume, so that it can withdraw enough energy from the field to activate the measuring instruments. In addition, the currents induced on the probe by the incident field will disturb and modify the original incident field. Another consequence of the existence of a finite probe is that it can be viewed as a scatterer which in turn will modify the radiation mechanism of the

radiator under test. This in turn will modify the field values which existed before the introduction of the measuring probe. The latter effect, which is called multiple scattering is a very complicated phenomenon with a secondary influence on the measurement results for moderate separations between the probe and radiator[3]. The approach employed is to insure that the measurements are made (see Chapter Four) in a manner to ensure that the multiple scattering effect is negligibly small instead of trying to account for it. When the antenna and the field probe are close enough to effect noticeable multiple scattering, the extracted values may still be useful for qualitative evaluation but not for quantitative use.

Considering the above discussion, neglecting the multiple scattering and taking into account the implications of the linearity of the antenna, the output voltage of a probe, v_o, for a field, $\vec{E}_i$, incident on the probe, in reference to Figure (3.1) is:

$$v_o(\vec{r}) = \int_{pa} \vec{E}_i(\vec{r}+\vec{r}').\vec{f}(\vec{r}')d\,pa \qquad \ldots.(3.1)$$

where pa is the effective probe area and the weighting function is $\vec{f}(r'')$, which depends entirely on the probe geometry and materials.

It is obvious from Equation (3.1) that extracting the incident field from the output voltage involves two steps: the determination of the weighting function over the probe area, and then, solving the integral equation for the incident field.

Before going into the details, it is appropriate to mention three distinct cases of measurement and identify the nature of the probe behavior for each case:

The first case is when the probe dimensions are small enough in terms of wavelength such that it is possible to assume that the incident field is approximately constant over the probe surface. The field variable in Equation (3.1) then, can be placed outside the integral and the equation will be:

$$v_o(\vec{r}) \approx \vec{E}_i(\vec{r}).\int_{pa} \vec{f}(\vec{r}')d\,pa \qquad \ldots.(3.2)$$

The integral in Equation (3.2) is entirely dependent on the probe geometry and orientation which is a constant vector for a fixed frequency of operation. This means that the probe output voltage is proportional to the incident field at the measurement point. The field can be extracted, in this case, by multiplying the output voltage by a constant vector.

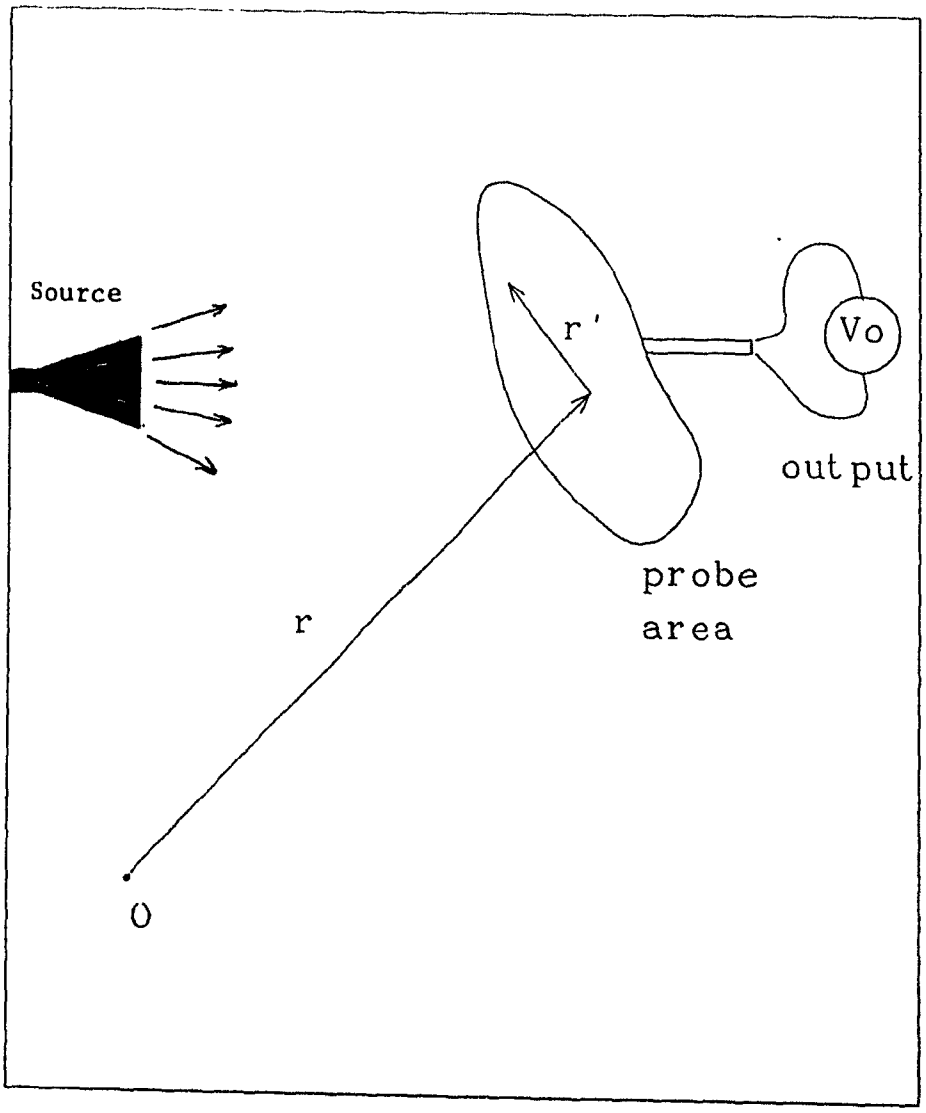

Figure (3.1): General probe configuration. Probe local origin is located at $\vec{r}$, and $\vec{r}'$ is the coordinate of a point at the probe surface relative to the probe origin.

The second case is when the measurement point is far enough from the radiator, such that the incident field can be approximated as plane wave originating from the radiator direction, in this case the electric field can be expressed as:

$$\vec{E}_i(\vec{r}) \approx \vec{E}_o e^{-\vec{k}\,\vec{r}} \qquad \ldots.(3.3)$$

where $\vec{k}$ is the wave number vector of the incident field with the magnitude k_o (the intrinsic wave number of the propagation medium), and direction of the incident plane wave. The output voltage from the probe will be:

$$v_o(\vec{r}) \approx \vec{E}_o \cdot \int_{pa} \vec{f}(\vec{r}') e^{-j\vec{k}\,(\vec{r}+\vec{r}')} d\,pa \qquad \ldots.(3.4)$$

The value of the integral will be a vector which depends on the direction of the plane wave in addition to the probe geometry. It can be shown, using the reciprocity theorem, that this integral can be expressed in terms of the phasor radiation pattern of the probe and the direction of the incident plane wave. The form of Equation (3.4) indicates that the field can, again, be determined at a point from a single phasor voltage measurement.

The third case is the general case, when no assumptions can be imposed on the nature of the incident field. This is the case for a practical probe used in the near or the immediate field measurement of the radiator. Equation (3.1) in this case is a Fredholm integral equation of the first kind which is ill-posed with a non-singular weighting function. When the field, however, is expressed in terms of an integral of orthogonal modes as described in the previous chapter and for certain shapes of the surface of measurement, Equation (3.1) can be rewritten in an algebraic form In this case the magnitude and phase for a certain range of modes can be determined from the phasor output voltage. The rest of this chapter deals with this problem. The field decomposition into elementary plane waves introduced in the previous chapter is utilized to permit a field extraction methodology.

3.2. Probe Considerations in Planar Near-Field Measurements:

When the planar measurement configuration of Figure (3.2) is considered, and the probe surface is assumed to be located on the plane of measurement ($z=0$), Equation (3.1) can be rewritten for this case as:

$$v_o(x,y) = \int\int_{pa} \vec{E}_i(x+x', y+y') \cdot \vec{f}(x', y')\, dx'\, dy' \qquad \ldots.(3.5)$$

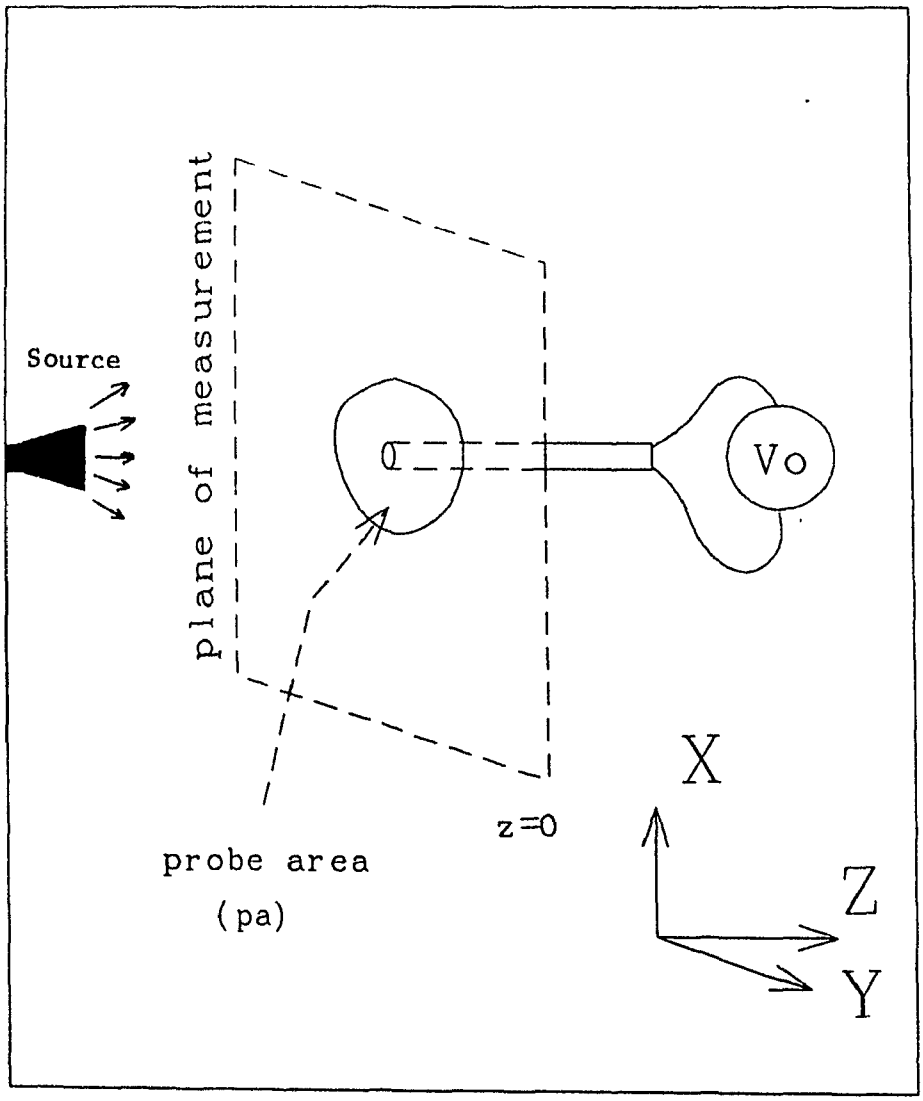

Figure (3.2): Field probe in planar near-field scanning configuration.

This convolution integral equation is ill-posed as stated earlier, but when inverse Fourier transforming both sides in two dimensions to express the variables in the spectral domain as a function of the spectral variables (k_x, k_y), the space domain convolution relation will yield a spectral domain multiplication as follows:

$$v_o(k_x, k_y) = \vec{E}_i(k_x, k_y).\vec{F}(k_x, k_y) \qquad \ldots.(3.6)$$

where $\vec{E}_i(k_x, k_y)$ is the inverse Fourier transform of incident field, and $\vec{F}(k_x, k_y)$ is the Fourier transform of the weighting function.

It is evident here that the recoverable field modes are the ones for which the transformed weighting function is not small enough, so that the calculation of the mode amplitude is sensitive to errors or noise in the measured voltage.

The procedure of planar field measurement considered here is described in Section (2.3). To collect enough information about the field, the output voltage in planar scanning is measured on a regular grid over the plane of measurement S for two orthogonal probe orientations. This is done to acquire information about the two perpendicular field polarizations. The two orientations can be labeled as x and y, indicating the direction of a particular axis of the probe geometry which lies within the surface S. Then, for each point of measurement on the plane S, it is possible to define the *vector measured voltage* by the following relationship:

$$\vec{v}(x, y) = \hat{x}v_x(x, y) + \hat{y}v_y(x, y) \qquad \ldots.(3.7)$$

whose inverse Fourier transform is:

$$\vec{V}(k_x, k_y) = \hat{x}V_x(k_x, k_y) + \hat{y}V_y(k_x, k_y) \qquad \ldots.(3.8)$$

The above definition of the measured voltage combined with Equation (3.6) results in a set of two algebraic equations with three unknown field components. The third relation, necessary for completing the set, can be obtained using the fact that the measurement plane is source-free. The incident field divergence is, therefore, zero, i.e. $\nabla.\vec{E}_i(k_x, k_y) = 0.$, which leads, using Equation (2.19), to the third relation:

$$\vec{k}.\vec{E}_i(k_x, k_y) = 0$$

This indicates that it is possible to write the three incident field components in terms of the *vector measured voltage* as follows:

$$E_x(k_x,k_y) = \vec{C}_x(k_x,k_y).\vec{V}(k_x,k_y)$$
$$E_y(k_x,k_y) = \vec{C}_y(k_x,k_y).\vec{V}(k_x,k_y) \quad \ldots.(3.9)$$
$$E_z(k_x,k_y) = \vec{C}_z(k_x,k_y).\vec{V}(k_x,k_y)$$

where $\vec{C}_{x,y,z}(k_x,k_y)$ are the *vector field extraction coefficients* that have to be determined. These depend on the probe structure, the operating frequency as well as the tangential wave numbers. $\vec{C}_x(k_x,k_y)$ can be written as:

$$\vec{C}_x(k_x,k_y) = \hat{x}C_{xx}(k_x,k_y) + \hat{y}C_{xy}(k_x,k_y) \quad \ldots.(3.10)$$

The two remaining vectors $\vec{C}_y(k_x,k_y)$ and $\vec{C}_z(k_x,k_y)$ can be constructed similarly.

Expressing Equation (3.6) in the form of Equation (3.9) has the following advantages:

1. The ability to include the cross polarization of the probe as part of the measurement data. Under the assumption of a perfectly polarized probe, the coefficients $\vec{C}_x$ and $\vec{C}_y$ may have only one component if the probe axis is chosen properly.

2. The logic that led to Equation (3.9) applies to both the electric and magnetic incident fields. Only the values of the field extraction coefficients will be different for the same probe as will be shown later.

3. It is possible to evaluate the sensitivity of the calculation of each field component to the error in the measured vector voltage. Therefore, the range of validity of the measured results in (k_x,k_y) can be defined after setting some acceptable error limit criterion. To illustrate this point, if the error in the vector voltage for a certain mode is expressed as $\vec{\epsilon}_v = \hat{x}\epsilon_x + \hat{y}\epsilon_y$ then the error ϵ_e in calculating one of the field components is:

$$\epsilon_e(k_x,k_y) = \vec{C}(k_x,k_y).\vec{\epsilon}_v(k_x,k_y) = |\vec{C}(k_x,k_y)||\vec{\epsilon}_v(k_x,k_y)|\cos\theta \quad \ldots.(3.11)$$

where θ is the angle between the field extraction and the voltage error vectors. This angle can be set to zero to represent the worst case. This relation is used in defining the range of validity of measurements for the dipole and open ended waveguide probes considered in a subsequent section. The ability to define the range of valid measurement in (k_x,k_y), or alternatively the maximum tangential wave number for which the mode can be measured reliably, implies that the field mapping resolution on the measurement

surface can be determined employing Equation (2.12). This capability would not be possible if the probe measured voltages were considered for each probe orientation separately instead of considering a single vector measured voltage.

3.3. Theoretical Determination of the Vector Field Extraction Coefficients:

For any field probe with a linear behavior, there exist a set of vector field extraction coefficients. Their existence is based on the validity of Equation (3.1), for which the linearity of the probe material is the only assumption made. Further constraints on the probe structure are necessary to facilitate analytical expressions for these coefficients: first, the probe and its feed circuit must be reciprocal, i.e. made only of material with symmetric permittivity and permeability tensors[49], so that the application of the reciprocity theorem is possible in relating the behavior of a transmitting probe to a receiving one. The second constraint is that the probe receiving (or radiating) elements are either wires contained within a plane that coincides with the planar surface of measurement, or an aperture whose plane coincides with the surface of measurement as shown in figures (3.3-a) and (3.3-b) It is worth mentioning that most of the probes used in near field scanning meet these constraints A further assumption made here is that the electric current distribution on the wire probe or the aperture tangential electric field distribution on the aperture probe are known when these probes are transmitting. These distributions may be determined using measurements, existing numerical techniques or by reasonable, experience proven, approximations. In the latter two cases, only the receiving (or radiating) elements of the probe have to be reciprocal.

The details of the procedure used to find expressions for vector field extraction coefficients in terms of their current and aperture field distributions are shown in Appendix (A) in reference to Figure (3.3). The basis of the procedure is the application of a form reciprocity theorem[7]. This form relates the probe output voltage to the incident modal field. The probe is represented in this relation by the electric current or the aperture electric field distribution at the radiating elements for a unit input voltage. This result in a relation between the field components and the output voltage of the probe, in which the vector field extraction coefficients can be easily recognized.

The electric field extraction coefficients for the wire probe are thus:

$$\vec{C}_x = \frac{1}{\Delta}(\hat{x}F_x^* - \hat{y}F_y) \qquad \ldots(3.12-a)$$

$$\vec{C}_y = \frac{1}{\Delta}(\hat{x}F_y^* + \hat{y}F_x) \qquad \ldots(3.12-b)$$

$$\vec{C}_z = \frac{1}{\Delta}\left(\hat{x}\frac{-k_xF_x^* - k_yF_y^*}{k_z} + \hat{y}\frac{k_xF_y - k_yF_x}{k_z}\right) \qquad \ldots(3.12-c)$$

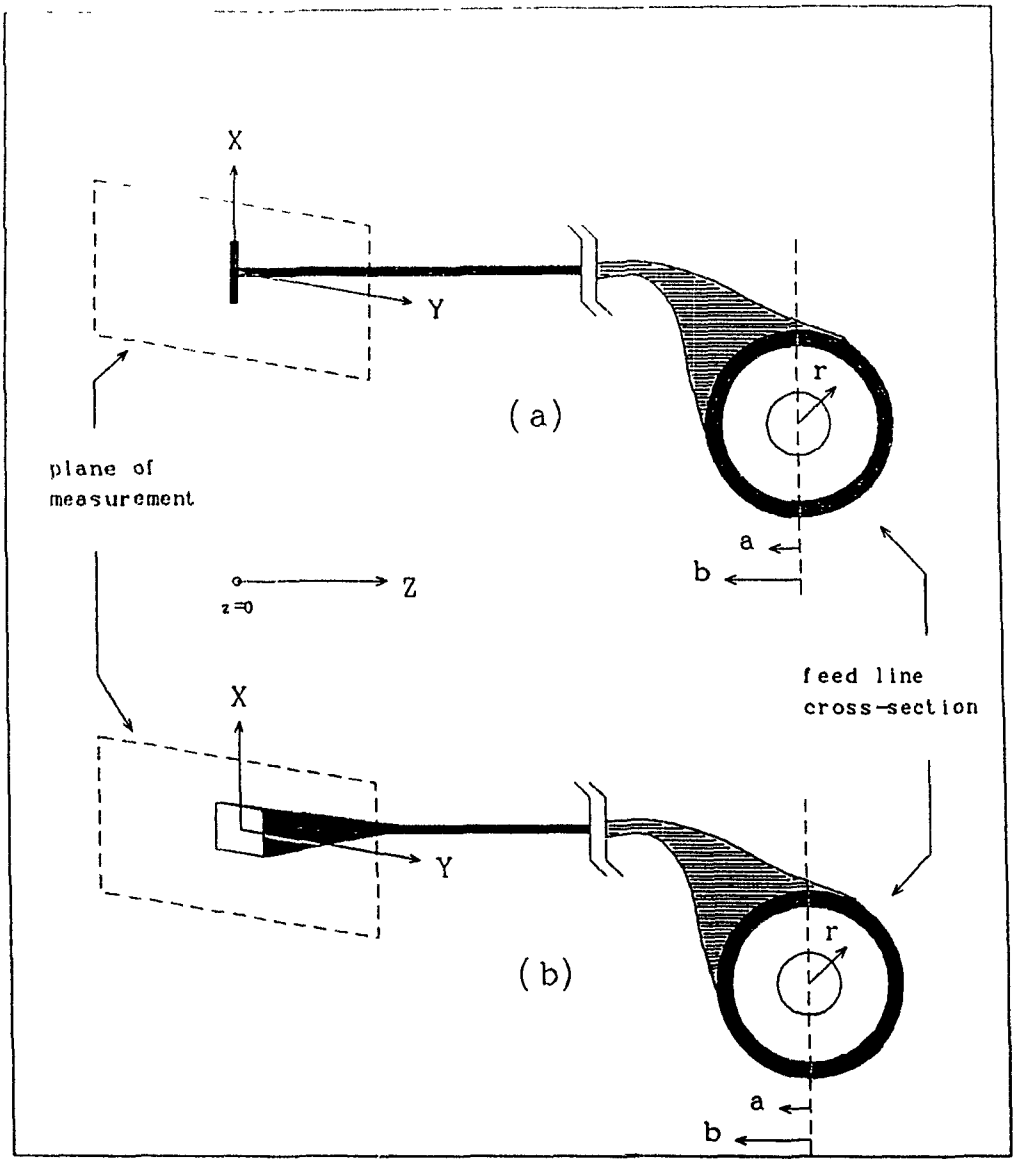

Figure (3.3): Field probe and probe feed line cross-section configuration.

a- Wire probe.

b- Aperture probe.

and correspondingly for an aperture probe, the electric field extraction coefficients are:

$$\vec{C}_x = \frac{1}{k_0^2\Delta}\left(\hat{x}\frac{(k_y^2+k_z^2)F_x^* - k_xk_yF_y^*}{k_z} - \hat{y}\frac{(k_y^2+k_z^2)F_y + k_xk_yF_x}{k_z}\right) \quad \ldots.(3.13-a)$$

$$\vec{C}_y = -\frac{1}{k_0^2\Delta}\left(\hat{x}\frac{(k_x^2+k_z^2)F_y^* - k_xk_yF_x^*}{k_z} + \hat{y}\frac{(k_x^2+k_z^2)F_x + k_xk_yF_y}{k_z}\right) \quad \ldots.(3.13-b)$$

$$\vec{C}_z = \frac{-1}{k_0^2\Delta}(\hat{x}(k_xF_x^* + k_yF_y^*) + \hat{y}(k_yF_x - k_xF_y)) \quad \ldots.(3.13-c)$$

where $\Delta = F_xF_x^* + F_yF_y^*$, $F_x(k_x, k_y)$ and $F_y(k_x, k_y)$ are the $\hat{x}$ and $\hat{y}$ components, respectively, of $\vec{F}(k_x, k_y)$, which is the Fourier transform of the wire electric current distribution or the aperture electric field distribution, and $F^*(k_x, k_y) = F(k_x, -k_y)$.

It is evident from Equation (3.12) that the output voltage is completely coupled to the electric field tangential to the plane of measurement in a wire probe, except for the averaging effect introduced by the finite size of the probe. The coupling for the component normal to the plane of measurement z, is dependent on the incident mode, in addition to the averaging effect, and will approach zero for $k_z = 0$, which is the border of the radiation region in (k_x, k_y), because of the singular value of $\vec{C}$ at these points. The opposite holds for an aperture probe as concluded from Equation (3.13), which indicates that the two probes complement each other, thus providing a wider range of validity of measurement of the three field components.

The aperture probe is characterized by the tangential electric field distribution on the aperture. The equivalence principle[7] can be used to replace the aperture field distribution by an equivalent magnetic current, $\vec{M} = \hat{n} \times \vec{I}$ for a planar aperture, where $\hat{n}$ is a unit vector normal to the aperture plane ($= -\hat{z}$) This will affect slight modification on Equation (3.13) by replacing I_x by $-I_y$ and I_y by I_x so that $\vec{I}$ will stand for an equivalent magnetic current distribution on the probe aperture In this case, the wire and aperture are exactly dual, which implies, from the symmetry in Maxwell equations, that the expressions of the vector magnetic field extraction coefficients are simply Equation (3.12) for an aperture probe, and the modified Equation (3 13) for the wire probe. In this manner, the field extraction coefficients of Equation (3 12) which yield the electric field components for a wire probe, will also yield the magnetic field components when applied to an aperture probe, and the opposite hold for the modified Equation (3.13). This is shown graphically in Figure (3.4).

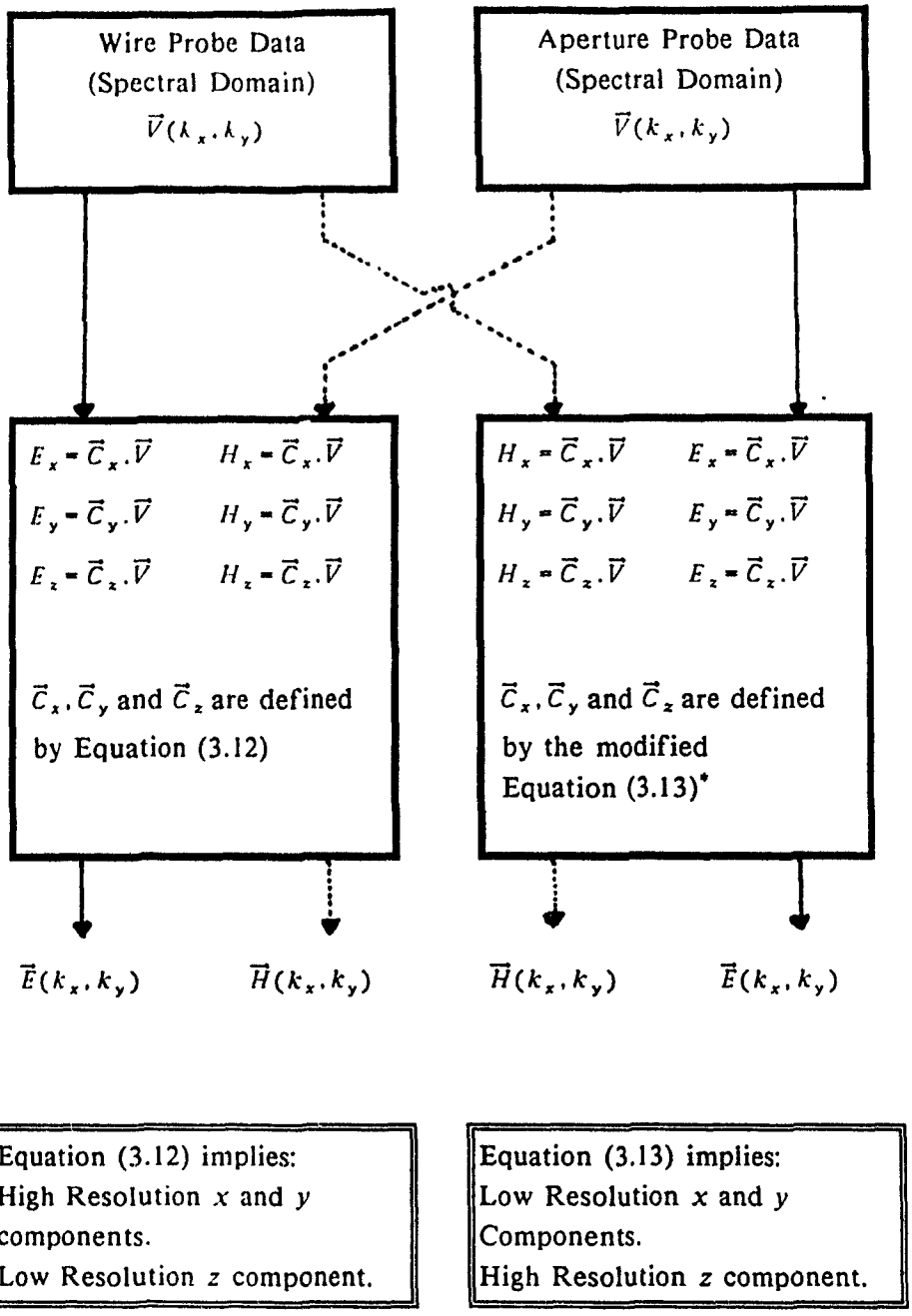

Figure (3.4): Illustration of the consequences of the symmetry of Maxwell equations. Either electric or magnetic field data can be extracted from the probe measured voltage, but with varying resolution for the three components.

* Equation (3.13) is modified by replacing F_x by $-F_y$ and F_y by F_x, so that these quantities represent the spectral domain equivalent magnetic current at the probe aperture instead of the aperture electric field distribution.

As illustrative examples of the application of the vector field extraction coefficients, two common types of probes are considered; a half wave length dipole as a wire probe, and an open ended dielectric loaded rectangular waveguide as an aperture probe. These probes are shown in Figure (3 5). When the probes are transmitting, cosine current distribution is assumed along the $\lambda/2$ dipole, and the TE_{10} mode is assumed at the waveguide opening with dimensions $(\lambda/5, \lambda/2)$. This assumes a dielectric constant of approximately 2.2 so that the two probes are operating at the same frequency. These distributions are, of course, first order approximations More realistic distributions could be used, but would unnecessarily complicate the following expressions. There is no loss of generality if the propagation constant k_o is set to unity, which corresponds to a wavelength of 2π. Considering the above, the current and aperture distribution functions can be written in the space and spectral domains as:

$$f_{xd}(x,y) = \frac{1}{2}\delta(y)\cos(x), \quad f_{yd}(x,y) = 0.$$

$$F_{xd}(k_x,k_y) = \frac{\pi}{4}\left[sinc\left(\frac{\pi}{2}(1-k_x)\right) + sinc\left(\frac{\pi}{2}(1+k_x)\right)\right]$$

$$f_{xa}(x,y) = \frac{5}{4\pi}\left[U\left(x+\frac{\pi}{5}\right) - U\left(x-\frac{\pi}{5}\right)\right]\cos(y), \quad f_{ya}(x,y) = 0.$$

$$F_{xa}(k_x,k_y) = \frac{\pi}{4} sinc\left(\frac{\pi}{5}k_x\right)\left[sinc\left(\frac{\pi}{2}(1-k_y)\right) + sinc\left(\frac{\pi}{2}(1+k_y)\right)\right]$$

where the subscripts (d) and (a) indicate the dipole and aperture probes, respectively. The field extraction coefficients are evaluated from the above spectral domain distributions using equations (3.12) and (3.13).

To evaluate the range of validity of the measured field components, a measured field component for a mode (k_x, k_y) is considered acceptable if the error power multiplication, calculated using Equation (3.11), for this mode does not exceed twice the error multiplication for the mode (0,0). This criterion takes into account the fact that the radiation pattern peak is in the boresight direction for both probes. Other criteria can be applied depending on the nature of the probe, the quality of measuring instruments and the accuracy requirements. The value of the field extraction vectors lengths for the two probes and for the three field components are evaluated. Equation (3.11) is then applied to determine the error in the extracted field relative to the measured voltage error. The range of validity of the three electric field components for the two probes are shown in figures (3.6-a) and (3.6-b) for the cases of the dipole and aperture probe, respectively.

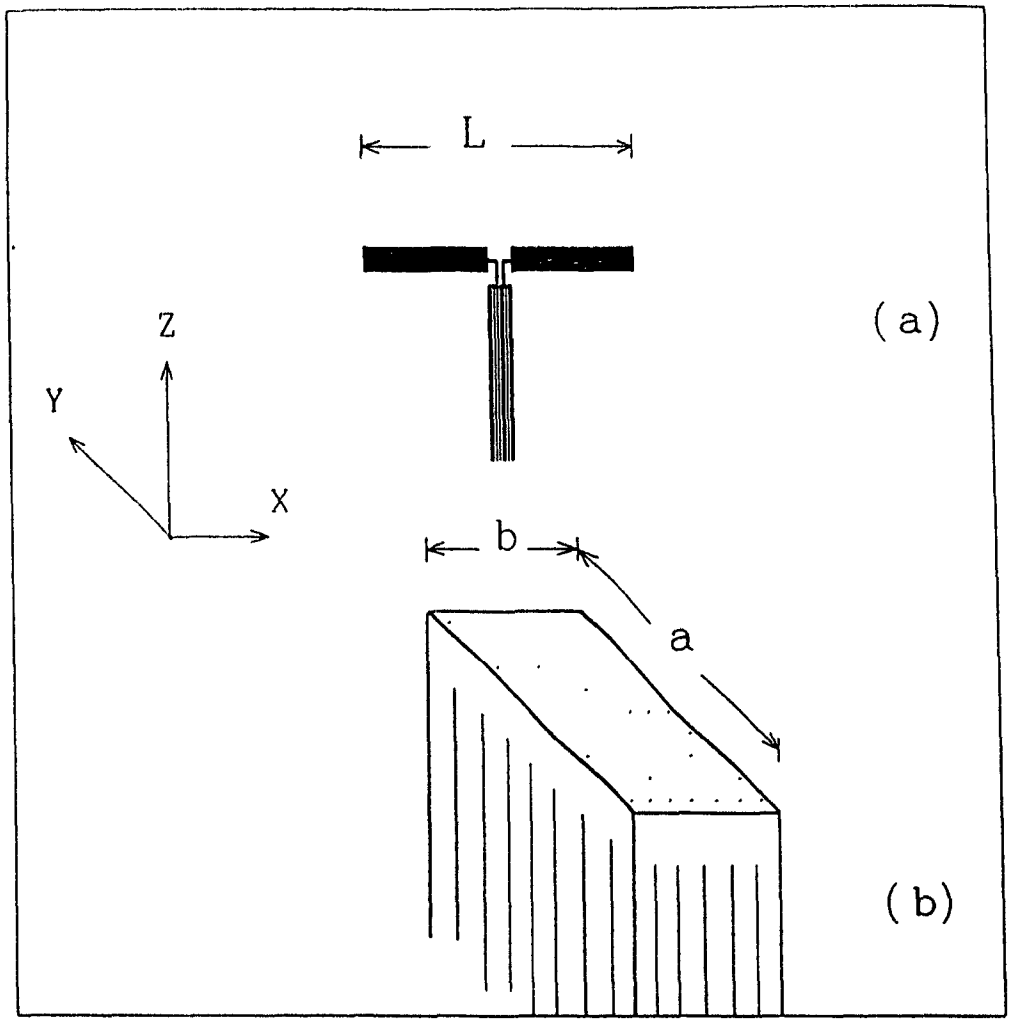

Figure (3.5): Probes used as examples of wire and aperture probes respectively.

a- Dipole probe, $L = \lambda/2$.

b- Open ended dielectric loaded waveguide. Aperture dimensions: $a = \lambda/2$ and $b = \lambda/5$. (λ =free space wavelength)

The dielectric loading the waveguide is assumed to have a dielectric constant, $\epsilon_r = 2.2$.

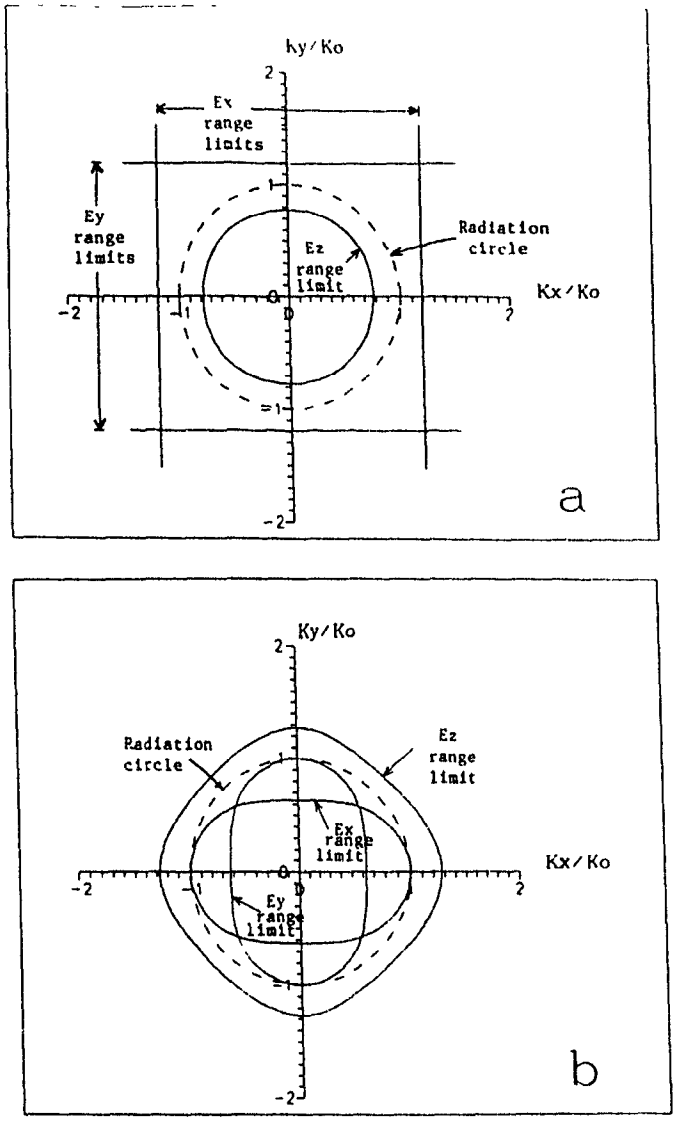

Figure (3.6): Measurement validity limits in the spectral domain for the three components of the electric field.

a- half wavelength dipole of Figure (3.5-a).

b- Open ended dielectric loaded waveguide of Figure (3.5-b).

The dashed circle in both above figures is the radiation circle, within which: $k_x^2 + k_y^2 \leq k_o^2$

By inspecting Figure (3.6), it is concluded that the dipole probe can measure the tangential field components (x,y) for wide range in the spectral domain which covers smoothly the whole radiation region in (k_x, k_y) and extends to the evanescent region. This is not the case for the normal (z) component, because of the singularity in the expression for $\vec{C}$ for $k = 0$, the boundary of the radiation region. The opposite holds for the results of the open ended waveguide as evident from the same figure.

3.4. Experimental Determination of the Vector Field Extraction Coefficients:

The logical approach in trying to measure the characteristics of a probe is, simply, to measure the output of the probe in a known field. This is usually not possible, because of the difficulty in establishing a *reference* field distribution. On the other hand, by inspecting equations (3.12) and (3.13), and referring to the derivation of these equations, it is evident that there are no approximations involved in relating the currents (electric or magnetic) on the probe surface to the field extraction coefficients. The only approximation is in evaluating the current distributions on the probe. The relation between the phasor radiation pattern of an antenna and the Fourier transform of the current distribution is well established [10,41]. One can, therefore, evaluate the current distribution in the spectral domain using a measured phasor radiation pattern and by substituting these values either in Equation (3.12) or (3.13) to evaluate either set of the field extraction coefficients.

The complex radiation pattern of the probe is conventionally used as the probe model to recover the radiation pattern of the antenna under test from the near field measurements[3,30,50] The only objection that can be raised is over the inability to measure the phase in the probe far-field accurately. The far-field measurement by definition involves large separation between the probe under test and the far-field probe, while the phase error is proportional to the error in the distance between the probe under test and the far-field probe, in wavelengths The difficulty is in allowing a large separation between the two probes to conform with the far-field assumption while keeping the phase accuracy within certain limits for that large separation.

In this work an alternative approach is suggested, using two identical probes. First, the current distribution on the first probe is considered as the unknown. The field generated by this distribution in the spectral domain can be evaluated using

equations (2.5) or (2.6). If planar scanning is performed using the second probe, for the field generated from the first probe, the output voltage can be predicted using equations (3.12), (3.13), (A-6) or (A-8). These relations are again related to the current distribution. A set of relations for each mode can be constructed such that:

$$v_{ox}(k_x, k_y) = cD(\vec{F}(k_x, k_y), d).v_i \qquad \ldots.(3.11-a)$$

$$v_{oy}(k_x, k_y) = cD(\vec{F}^*(k_x, k_y), d).v_i \qquad \ldots.(3.11-b)$$

where $D(\vec{F}(k_x, k_y), d)$ is a function of the spectral current distribution on the probe surface and the normal distance between the transmitting probe and the plane of measurement, c is a constant, and $\vec{F}^*(k_x, k_y) = \vec{F}(k_x, -k_y)$. The measurement of field extraction parameters is conducted, in this case, in an environment similar to that of the actual measurements.

The above procedure was applied in measuring the spectral domain electric current distribution of a dipole probe[40]. To simplify the measurement and the numerical processing, the dipole is assumed to radiate cylindrical waves and consequently, the receiving pattern is symmetrical around the dipole axis This comes from the approximation that the dipole arms are thin enough that the electric current is flowing only along the dipole axis. Considering Figure (3.7-a) for the dipole configuration, the current distribution along the dipole is $f(x)$ with Fourier transform $F(k_x)$ for unit input voltage.

The x component of the radiated electric field at a distance d can be expressed as an integral of cylindrical modes over k_x [7]:

$$E_x(x', d) = \int_{k_x} A(k_x) H_o^{(2)}(k_r d) e^{-jk_x x'} dk_x$$

where $k_r = \sqrt{k_o^2 - k_x^2}$ and $A(k_x)$ is the mode amplitude. The modal field can be expressed in terms of the spectral domain current distribution as:

$$E_x(k_x, d) = \hat{x} \frac{v_i}{j\omega\epsilon_o} F(k_x) H_o^{(2)}(k_r d) k_r^2$$

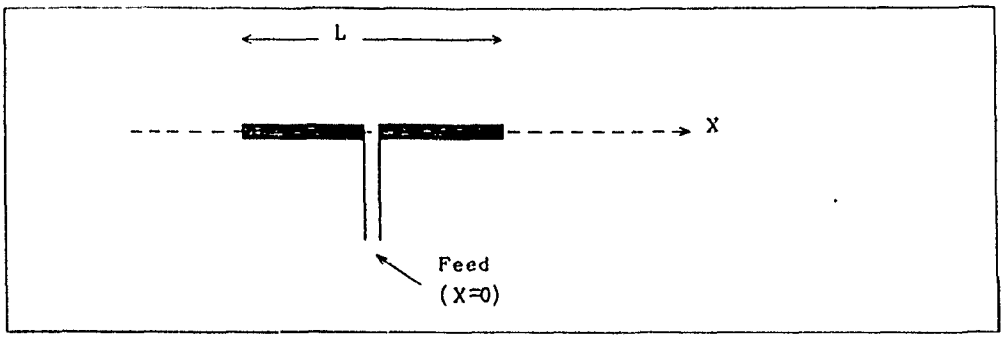

Figure (3.7-a): Dipole under test configuration. The dipole is described in Appendix (B) as probe #1.

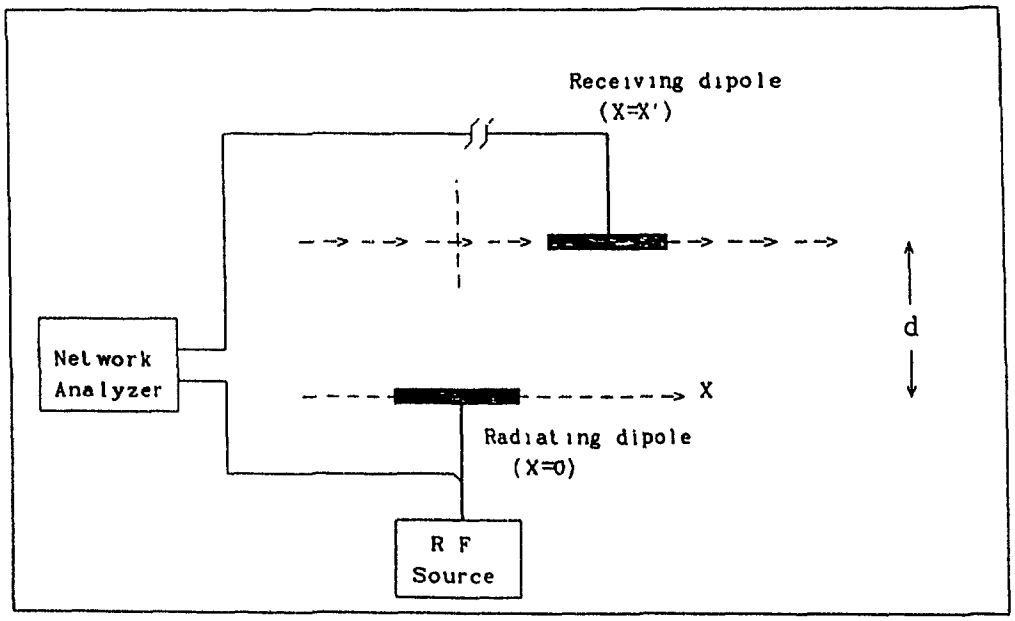

Figure (3.7-b): Configuration of measurement of field extraction coefficients of a dipole probe. The two dipoles are identical, and the receiving probe is scanned along the x'-axis.

By substituting the above relation into Equation (3.12-a) with the special case that the output voltage vector has a single component, and including all the constants in one constant, c :

$$v_o(k_x, d) = cF^2(k_x)H_o^{(2)}(k_r d)k_r^2 e^{-jk_x d} \qquad \ldots.(3.15)$$

The above relation is similar to Equation (3.14) from which the spectral domain current distribution can be evaluated using the inverse Fourier transform of the measured output voltage.

Measurements are necessary only along a line parallel to the two probes axes as shown in Figure (3.7-b), where the receiving probe is moved along the x' axis and the transmitting dipole is fixed at x=0. The separation distance between the two axes is d, and the output from the receiving probe is measured in amplitude and phase, relative to the input voltage at a regular sampling rate along the x' axis within a range which includes significant interaction between the two probes. The measurement was repeated for several values of d for comparison.

The output voltage, as a function of x' is Fourier transformed to get $v_o(k_x, d)$, which is shown in Figure (3.8). The measurement was performed at a frequency of 11.65 GHz. (λ = 2.575cm.), and two distances d of .5 and 2. cm., $\approx .2$ and $.8\lambda$ respectively. The interaction due to evanescent modes ($k_x > k_o$) is evident in the first case, while it is negligible in the second case. The current distribution function $F(k_x)$ can be evaluated using Equation (3.15). The distance d was increased in steps of $\approx .2\lambda$ until the distribution was nearly independent of the variation of d. This represents negligible multiple scattering between the probes. A distance of 2.cm was found to be enough for this purpose.

The current distribution function is normalized to unity at k_x=0., so that the constant c in Equation (3.15) can be evaluated. The current distribution function appears squared in Equation (3.15), which results in two values of that function. Therefore, analytical continuity was considered to choose one of them. The resulting distribution function is plotted in Figure (3.9) versus k_x using the d=2.cm. data. Even though there was no assumption of real-valued current distribution, the results have negligible imaginary parts. On the same graph, a numerically determined current distribution is shown. This distribution was calculated for the dipole probe under consideration using the method of moments[41].

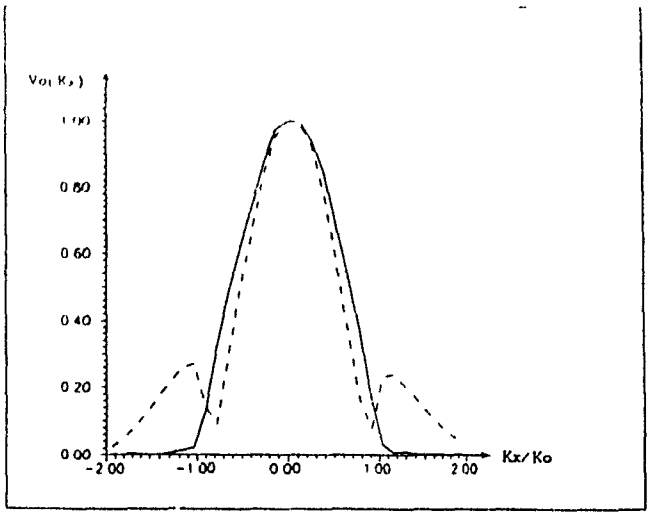

Figure (3.8): Inverse Fourier transform of the output voltage, for the moving dipole probe, versus the normalized tangential wave number k_x/k_o

Solid curve: distance d= 2 cm. (≈ .8λ).

Dashed curve: distance d= 0.5 cm. (≈ .2λ).

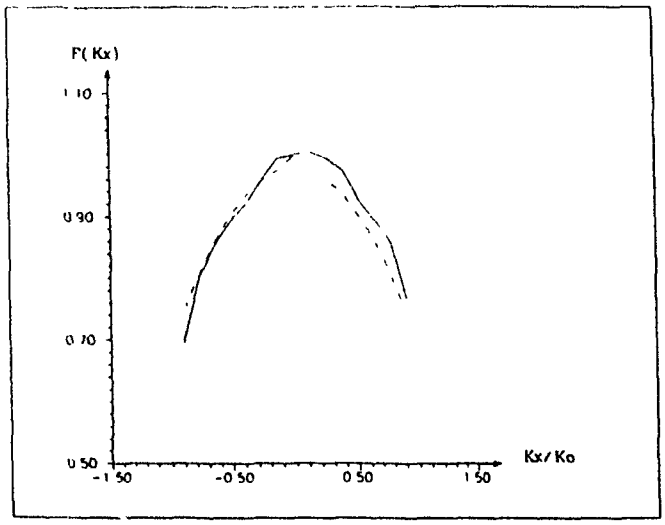

Figure (3.9): Axial electric current distribution on the dipole in the spectral domain (versus k_x/k_o).

Solid curve: Experimental results using distance d= 2 cm. data.

Dashed curve: Calculated using the method of moments.

In the above special case, some assumptions were used to facilitate the measurement procedure and subsequent processing. These included neglecting the cross-polarized currents and the effect of the feed and support structure. In general, it is necessary to perform a two dimensional planar scan, in the two orthogonal probe orientations, to be able to apply Equation (3.14). In this case, it is possible to find the two components of the equivalent current distribution. Equations (3.12) or (3.13) can then be used to evaluate the vector field extraction coefficients. Separate measurements and calculations would be necessary for each frequency of operation.

The choice of the type of current distribution model to represent the probe appears initially, from the above procedure, to be independent of the physical structure of the probe. The values of the field extraction coefficients, however, have to be the same, independently of that selection. This leads to the conclusion that in choosing, for example, electric current to represent an aperture probe, Equation (3.12) would be used to calculate the field extraction coefficients. However, the spectral domain current distribution has to be singular at $k_x = 0$, so that the resulting x and y field extraction coefficients will also be singular, as they are supposed to be. Choosing magnetic currents on the other hand, will result in non-singular spectral domain current distribution, and the singularity in the field extraction coefficients will emerge because of the singularity in equations (3.13-a) and (3.13-b). This leads to the conclusion that the choice of the type of current to represent the probe is an essential factor in obtaining a well-behaved spectral domain current distribution.

3.5. Comparative Discussion of the Vector Field Extraction Coefficients Approach:

The method developed here, of extracting field information from the measurement probe output voltage, does not differ in principle from that developed earlier under the name of *probe correction*. It was stated in sub-section (1.1.3), that all the field extraction techniques characterize the probe by its behavior as a radiator, and use the fields[50] or circuit[30] forms of the reciprocity theorem in relating that behavior to the probe performance in the planar measurement environment. The conventional purpose of the planar near-field measurement is to evaluate the far-field of highly directive antennas, while the general objective of the planar measurement here, is to map the equivalent currents at the aperture of the non-directive radiator under consideration, as indicated in Chapter Two. The method proposed here can also be used to evaluate the far-field radiation pattern from the extracted spectral domain electric or magnetic fields[41], while keeping in mind that the extracted fields, here, are the inverse Fourier transform of the space domain fields. It is necessary at this point to enumerate the features of the approach proposed here in comparison with the existing practice:

1. The measured probe voltage is described as a space vector (Equation (3.7)). This is linked to each field component at the plane of measurement by a proportionality constant, which is the field extraction vector for a certain mode. This will unify the two components of the measured voltage as one quantity, which enables defining the contribution of measurement errors on each field component by Equation (3.11). The definition is valid over the spectral domain, including the evanescent region. Accordingly, the probe performance can be determined, even for evanescent incident modes, once the field extraction coefficients are evaluated.

2. The probe is characterized here by the aperture electric or magnetic current distribution when radiating This permits the definition of the field extraction parameters over a wide range in the spectral domain, starting from analytically or numerically evaluated current distributions. This is an alternative to defining the probe by its phasor radiation pattern, which would enable extracting the field values only to within a limited area of the radiation circle The other advantage of this characterization, is that a link can be established between the radiation mechanism of the probe and its performance in the planar measurement environment. This link gives better insight into the field extraction process.

3. A unified approach is employed here for the extraction of the electric and magnetic fields. A unified approach is employed, also, in dealing with wire or aperture probes under the constraints specified in Section (3.3). This feature is necessary in field extraction since it was shown in Section (2.4) that it may be necessary to extract the magnetic field from the measured probe voltage if the radiator under test can be modeled by an equivalent electric current distribution.

4. The main advantage of formulations using S-paramaters is to account for multiple reflections between the radiator under test and the measurement probe. This advantage is not used in practice because of the complexity of the coupling between radiator and the moving probe[3]. The reverse scattering coefficients, consequently, are set to zero. Here, the assumption of neglecting the multiple reflection is posed as basic assumption, thus resulting in a simplified formulation.

5. The TE-TM decomposition[1] of the measured field is also a circuit concept. The characteristic impedance for each mode will differ for its TE and TM components. This concept is also not used here, because the modal characteristic impedance is not used to link the electric and magnetic fields. Maxwell equations are used for this purpose.

3.6. Concluding Remarks:

This chapter dealt with the problem of the extraction of field quantities from the measured field probe voltages. The problem was presented analytically first, to investigate the probe response for the three distinct cases:

i. A small probe.

ii. Plane wave incident field.

iii. The general case of unspecified probe and incident field.

The derivations are performed, in keeping with the previous chapter, for the planar measurement configuration, using the plane wave spectrum representation of the electromagnetic fields. The *vector field extraction coefficients* are introduced to model the probe for a single frequency of operation. Their use in finding the range of measurement validity in the spectral domain is demonstrated. The method of theoretically estimating the field extraction coefficients is detailed for fairly general wire and aperture probe configurations, and examples of measurement validity for two specific probes are demonstrated. It was concluded from these examples that a complete description of the electromagnetic field is not possible using a single probe type for the entire radiation zone of the plane wave spectrum. However, guidelines were established for probe selection for particular measurement tasks.

Realizing that a theoretical model of a probe might not be accurate enough to use as a basis of the field extraction procedure, a general method is suggested for measuring the field extraction parameters by scanning two identical probes. The experimental results are shown for the special case of a half wave-length dipole. This method can be extended to find an unknown probe from a known one. In this case, the unknown probe is a radiator under test for which the aperture current distribution is unknown, which is the problem dealt with in Chapter Two, while this chapter dealt with accounting for the known probe.

The features of the field extraction procedure employed here, are listed in comparison with existing *probe correction* procedures, which are used mainly to deal with highly directive antennas. It is concluded that, while all the procedures use the same principles, the procedure employed here is more powerful in predicting the probe performance in planar measurement by using its detailed electromagnetic behavior. In addition, it has been shown (see Figure (3.4)) that by using any probe, either the electric or the magnetic field can be determined using the appropriate set of field extraction coefficients.

It was shown in Section (2.4), that when a radiator is modeled by an equivalent electric current, it is necessary to measure the magnetic field components tangential to the plane of measurement, or the three electric field components, to be able to map the equivalent radiating sources. Similarly, it is necessary to measure the electric field components tangential to the plane of measurement, or the three magnetic field components, to be able to map the equivalent radiating magnetic currents It was also shown in Section (2.1), that the choice of the type of currents to represent the radiation is dependent on the nature of the antenna, or radiator, under test. By consulting the results of Section (3.3), it seems that a fundamental selection criterion can be employed for the type of probes to be used in the measurement: *A wire probe is a more appropriate choice for measuring fields radiated by aperture radiators, while an aperture probe is more appropriate for measuring the radiation from wire radiators*

The above criterion seems to be in conflict with the general practice of using aperture probes for near-field scanning of directive aperture antennas. By consulting Figure (3.6), it is apparent that both types of probes are adequate when only a finite range around the centre of the radiation circle in the (λ_x, λ_y) plane is considered, which is enough when a highly directive antenna is under test With a broad-beam radiator however, it is necessary to measure a broad range of spectral field components within the radiation circle, or even some part of the evanescent spectrum if the plane of measurement is close to the radiator In this case, the choice of the type of measuring probe is critical, and the above criterion should be employed towards that purpose.

The ideas developed in this and the previous chapters are used in the following chapter for designing measurements and the subsequent data processing to study particular antenna forms The external fields of three different types of radiators are investigated to apply and demonstrate the utility of the results, and because of the general interest in the three cases chosen.

CHAPTER FOUR

APPLICATIONS

In this chapter, the experimental work based on the theory introduced in the previous two chapters is reported. Three cases are considered as representative examples of non-directive radiators. These cases are of general interest, and their study is also of practical utility. A separate section is devoted to each case. It was shown in Chapter Two that the measurement configuration is highly dependent on the particular radiator configuration. The decisions and choices taken in this chapter for each specific case are discussed from that perspective. The chapter aims at establishing experience in conducting the measurements and in processing the results, with the objective of investigating possible efficient models to represent the radiators under test. It will be demonstrated that some conclusions can also be made about the nature of the radiation from the radiator under test Such conclusions might not have been possible without applying the theoretical and the experimental techniques introduced in this work. These conclusions are drawn taking under consideration also the available literature and current information dealing with such radiators

The work presented here falls into the major category of field measurements on a plane in the vicinity of the radiator. The field values are then extracted from the measured voltage using the principles discussed in Chapter Three, and finally, the extracted field values are processed to find the immediate field distribution, or the equivalent currents, on the radiator plane Other useful characteristics, such as the radiation pattern and the plane wave spectrum, are evaluated, whenever these characteristics can be used to gain more understanding of the behavior of the radiator. Such measurements assume that the behavior of the measuring probes is adequately understood, and can be modeled mathematically, so that the extraction of the field quantities from the measured voltage is possible In these measurements, dipole probes are employed and their description is detailed in appendix (B)

In addition to the above described *main stream* line of measurements, several measurements were conducted to confirm certain assumptions, to gain an initial idea about the field structure, or to compare field calculations with measurements.

The experimental facility used, which includes a precision tri-axial scanner for volumetric near-field measurements is described in Appendix (C). In order to meet the requirements of these measurements, considerable modifications were made to the system to improve stability, accuracy and dynamic range.

The computer programs used in processing the measurement data to produce the results shown in this chapter, as well as the other programs used throughout this thesis are described in appendix (D).

In the following sections, three types of radiators are dealt with. The first one is an approximation of an infinite open ended microstrip edge, which is a sub-wavelength radiator with two dimensional field structure. The second is a rectangular microstrip patch operating around resonance frequency, which is still small in size, but has a three dimensional field structure. The third radiator is a horn cluster of a type used as a feed for a satellite reflector antenna, with multiple wavelength aperture dimensions. The first two cases represent attempts to gain more understanding of the field structure around these radiators. In the third case, however, an effort is made to obtain practical, application oriented radiator model through the planar near-field scanning and the utilization of the equivalent current model.

The fields and currents that this thesis deals with are single frequency time harmonic, for which the field and current distributions are defined by a phasor space variable. In the experimental results presented here, the amplitude and phase of the measured and calculated fields and currents are available, but in most of the cases, only amplitude data are presented The phase information, however, is essential in the definition of the field structure, but it has the predictable nature of regressive phase proportional to the distance from the radiator. This behavior can be observed in the phase maps that are presented in this chapter. Most of the conclusions drawn from the experimental work are, therefore, based on the amplitude field and current distributions behavior.

4.1. Microstrip Edge Field Probing:

The infinite microstrip edge configuration, Figure (4.1-a), has been considered analytically in the past[51]. The major interest in the literature, however, has been in an accurate internal model for the edge. By internal is meant the edge behavior as seen from the feed point of view rather than the field in the space outside and around the edge. The reason for treating the problem this way is that most of the research efforts are directed towards obtaining a model for the edge equivalent lumped parameters, i.e. the input impedance of the edge looking from the feed point. In addition, the external field behavior is an open boundary problem, for which an accurate analytical solution

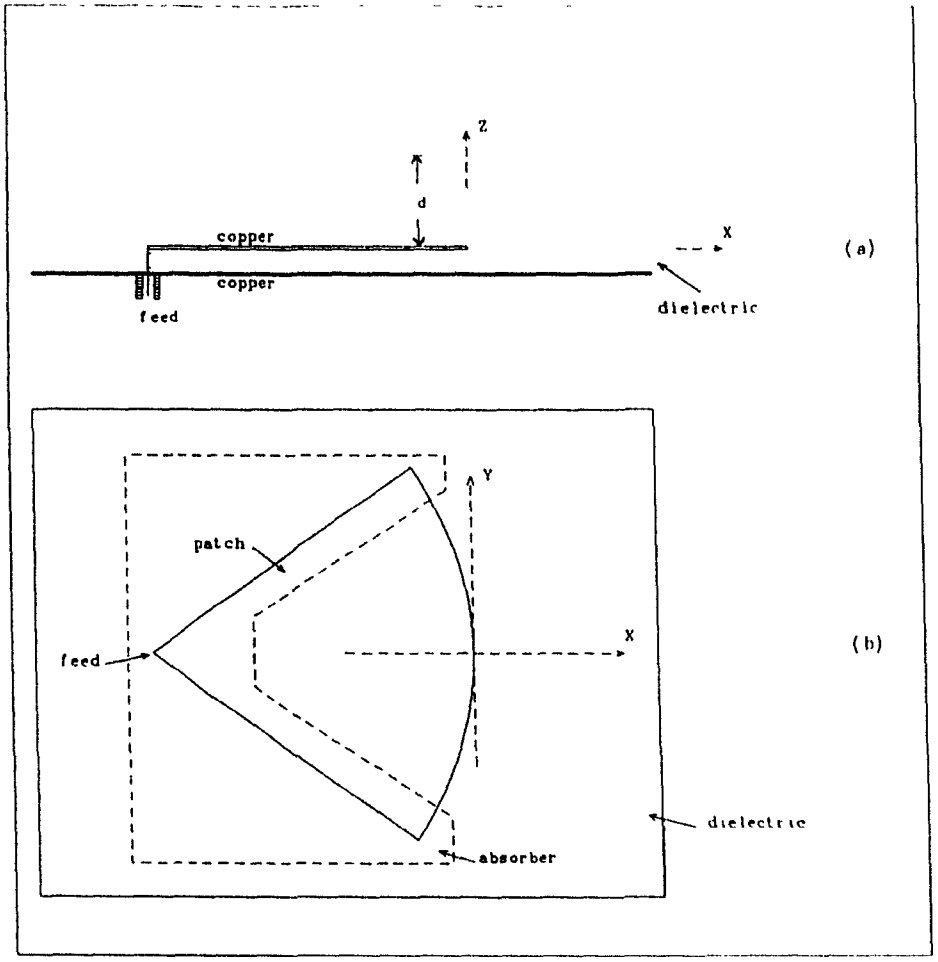

Figure (4.1): Experimental approximation of an infinite microstrip edge.

a) Side cross-sectional view. The field inside the patch is excited by the feed, and the microstrip edge is located at $x=z=0$. The geometry is ideally unchanged along the y-axis. The dielectric used as substrate is RT/Duroid 5880, with dielectric constant of 2.2 and thickness of 0.7 mm.

b) Top view of the experimental approximation The exterior field is expected to resemble that of an infinite edge at points close to the origin ($x=y=z=0$.). The location of the feed at the centre of the circle sector is expected to achieve a uniform field structure along the circular edge. The dashed line indicates the area covered with absorbing material

The dimensions are not shown to scale. The circular sector patch has 14.0 cm. radius and the sector angle is 70° The dielectric substrate has x and y dimensions of 257x204 mm. respectively. The distance between the feed point and the substrate edge is 3 cm.

The line measurements are carried out along lines parallel to the x-axis and with z distance of d.

does not exist currently, and the numerical methods dealing with such a problem are not yet well developed. The existing analytical approximation, internally, is the substitution for the edge by a shunt reactance to account for the fringing field at the edge, and a resistance to account for the radiation and the launched surface wave[52]. This model, however, is good enough to produce a fairly acceptable approximation of the edge when used in the context of modeling the microstrip antenna internal behavior. The edge is modeled externally by replacing it by an equivalent magnetic current line placed along the edge[53,54] It is attempted to devise some experiments to gain more understanding of the field behavior outside the edge, and to examine the limitation of these experiments. The techniques, presented here, can be used to study other radiators or scatterers, with two dimensional field structure, such as slits, strips or long wires.

4.1.1. Experimental Implementation of the Microstrip Edge:

Figure (4.1-b) shows an experimental realization of an approximate infinite microstrip edge. The structure, which is a circular sector patch is printed on an RT/Duroid 5880 dielectric ($\epsilon_r = 2.2$, thickness 0.7 mm., with conductive backing. The patch is fed through the back at the circle center in expectation that placing the feed at this point will result in the propagation of circular wave-fronts under the patch, which would illuminate the circular edge of the patch uniformly. This assumption has to be verified experimentally as will be shown later. To avoid radiation from the feed point and the straight edges, microwave absorbing material was placed over these edges. This material was grooved along these edges to avoid direct contact of the absorber with the edge. This is intended to reduce loading the straight edges excessively, thus enhancing the circular nature of the aforementioned wave-fronts. The location of the absorbing material is indicated by the dashed line in Figure (4.1-b). The only edge exposed to the air is the circular one, which is expected, at close distances, to resemble the behavior of an infinite straight edge The range of distances from the edge for which this expectation is valid has also to be determined experimentally.

The advantage of such a configuration is that it is of a reasonable size, and that only a single feed point is needed The obvious limitation is that the field has to be probed only close to the edge to resemble infinite edge behavior, and therefore, no direct measurement of the far-field can be carried out.

4.1.2. Model Confirmation and the Experimental Procedure:

It was first necessary to confirm that the field is uniform along the microstrip edge, both in amplitude and phase. Once this is established, it can then be assumed that there is uniform illumination of the edge indicating that the field inside the patch has circular wave-fronts originating from the feed, as was expected The test is accomplished by scanning a probe in a plane parallel to the patch surface, with the probe very close to that surface (1 mm from probe centre to the patch surface), and reading the probe output amplitude and phase at each point The probe used was the longitudinal short monopole probe #3 described in Appendix (B), with the receiving element aligned along the z-axis. The advantage of using this probe is its small size, which allows detailed field mapping and little interaction between the probe and the edge The fact, indicated in Appendix (B), that the reading of such a probe is unreliable for evaluating the actual field quantities, does not contradict its use in this case, since the objective here is to check the uniformity of the field along the edge rather than evaluating it The planar scan was performed for different frequencies within the X-band (8-12 GHz) The results of one of these scans are shown in figures (4.2-a) and (4.2-b) showing the amplitude and phase respectively at 10.2 GHz The results for other frequencies are similar, except for a change in the signal level and phase, possibly due to the varying mismatch between the patch and the feed line The uniformity of the field amplitude and phase, for fixed distances from the edge line, is evident from the above figures. It will be noted that the actual scans are along straight lines parallel to the edge tangent at y=0. This is an approximation to the curved edge for small ranges of y

After gaining some confidence that the edge is uniformly illuminated, it is possible to perform some measurements to reveal some of the infinite edge characteristics using the above described sector patch. One of the objectives is to determine the map of the field surrounding the edge and of the far field. This cannot be performed by direct measurement, because the infinite edge behavior is restricted to the proximity of the edge (at small z values in Figure (4.1)) as stated earlier It is possible, however, to measure the field close to the edge using a probe with a well defined model, and to transform the field values towards or away from the edge and to the far-field using the techniques described in chapters Two and Three In addition, only line measurements are necessary along lines parallel to the x-axis of Figure (4.1), instead of planar measurements, because of the assumed field uniformity along the y-axis. The concern in this case, is that for small distances between the patch surface and the line of

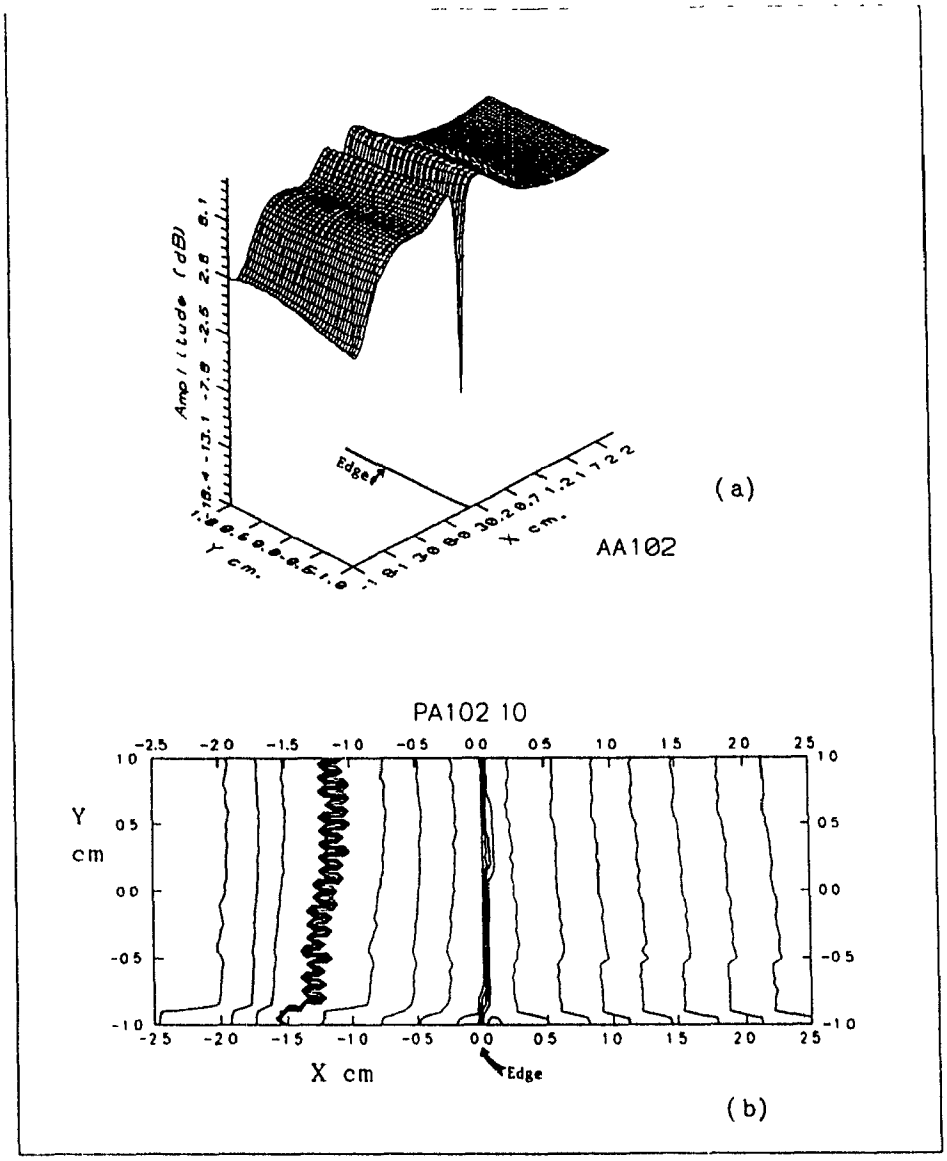

Figure (4.2): Experimental validation of the infinite edge approximation.

Longitudinal monopole (probe #3, Appendix (B)), is scanned over a plane parallel to the patch plane at a distance of 1 mm. from the patch surface. The probe output voltage is shown here, which is approximately proportional to the z component of the electric field distribution.

a) Relative amplitude distribution in dB.

b) Constant phase contours, with 45° contour interval.

The results indicate uniform amplitude and phase excitation of the edge (x=0) within -1.0 <y< 1.0.

measurement, the interaction between the probe and the patch may disqualify the results for subsequent calculations. If the distance, on the other hand, is too great, the infinite edge assumption will eventually fail The approach used is to perform measurements at varying distances from the patch surface, and examining the calculated far-field from each measurement. The far-field should be independent of the line of measurement distance when the infinite edge approximation holds.

The probe used in the measurement was the short dipole probe #2 described in appendix (B), oriented along the x-direction (line of measurement) This has been chosen because of the small size, so that there is minimum interaction between the probe and the edge, and also, because the field values extracted from the measured voltages are insensitive to the approximations in the probe model The probe was scanned at y=0, x=(-4.,4.) cm., in 1 mm. steps, with different z-axis distances ($=d$) ranging from 0.2 cm. to 1.5 cm. between the line of measurement and the patch surface. This was performed at an operating frequency of 11.6 GHz. ($\lambda \approx 2.59$cm.). The results of some of these measurements are shown in Figure (4.3). The edge coordinate in this and the following figures is $x=z=0$.

4.1.3. Processing and Presentation of the Measurement Results:

The mapping of the immediate field, or the equivalent currents, over the patch is performed using the methodology established in Chapter Two The inverse Fourier transform of the measured field is evaluated, and then, Figure (2 4) is used to set the range of tangential wave number (k_x) in the spectral domain that can be used towards calculating the equivalent currents using Equation (2 5-a) The spectral variable (k_y) is set to zero in this equation as a consequence of the two dimensional nature of the configuration. The magnitude of the plane wave spectrum of the measured field, extracted from the measured probe voltage, is shown in Figure (4.4) for different distances of the line of measurement indicated The decay of the evanescent modes ($|k_x/k_o| \geq 1$) can be observed in this figure as the distance is made larger The results for the immediate x-component of the electric field, which is proportional to the y-component of the equivalent magnetic current, versus x-coordinate, are shown in Figure (4.5), for two distances (d) of the line of measurements Secondary lobes are observed in the immediate field results, which can be attributed to the truncation of the plane wave spectrum. The larger immediate field amplitude resulting from the d=0 2cm. data is affected by the inclusion of the contribution from the evanescent modes, and because of the smoothing of the other figure as a consequence of spectrum truncation, which will spread the calculated immediate field energy over a larger region around the edge.

The evaluation of the far-field in this case was performed using the far-field approximation[41], from the equivalent line magnetic sources aligned along the y-axis. Because of the two dimensional structure of the radiator, the spatial Green's function for the source is a Hankel function of the second kind, $H_0^{(2)}(k_0|r-r'|)$. In the far-field, the Hankel function can be approximated to be proportional to $e^{-jk_0|r-r'|}/\sqrt{r-r'}$. The far-field approximation considers only the phase variation of Green's function, therefore, the far-field can be expressed as follows:

$$E_\theta(0) = \hat{\theta} A \int_{-\infty}^{\infty} M_y(x') e^{jk_0 \sin\theta x} \, dx \qquad \ldots.(4.1)$$

where θ is the angle between r and the z-axis, $E_\theta(0)$ is the far field electric field, A is constant that includes the radial field dependence, and $M_y(x')$ is the equivalent magnetic current source at z=0., which is proportional to the x-directed immediate field at the patch surface.

By inspecting the above equation, it is obvious that the far-field can be calculated for this configuration directly from the plane wave spectrum of the measured electric field as follows:

$$F_\theta(0) = E(k_x) \quad , \quad k_x = k_0 \sin\theta \qquad \ldots.(4.2)$$

Figure (4.6) shows the normalized radiation pattern calculated using the d=0.5 cm. measurement data.

To have an idea about the field behavior in the area surrounding the microstrip edge, the discussion in Section (2.6) is recalled, in which an explanation was given for the drawbacks of using the plane wave spectrum for near-near field transformation. Figure (4.7) shows the x component of the electric field calculated using aperture integration, or in other words, integrating the infinite line magnetic current along the x-axis. Equation (2.1) was used in evaluating the exterior electric field, with $J_s = 0$, and the dyadic Green's function was derived considering the fact that the field due to the infinite line current has a Hankel function of the second kind ($H_0^{(2)}(k_0 r)$) radial dependence. This field distribution was calculated using the data for d=0.5 cm. ($\approx .2\lambda$).

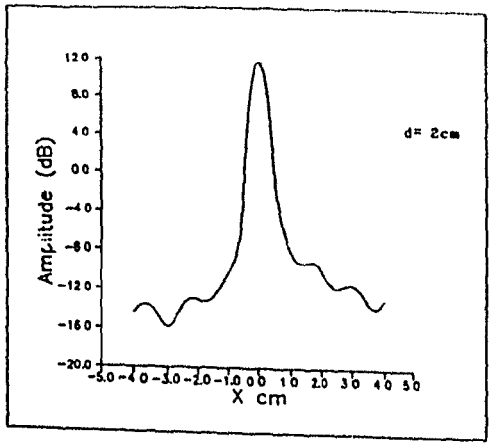

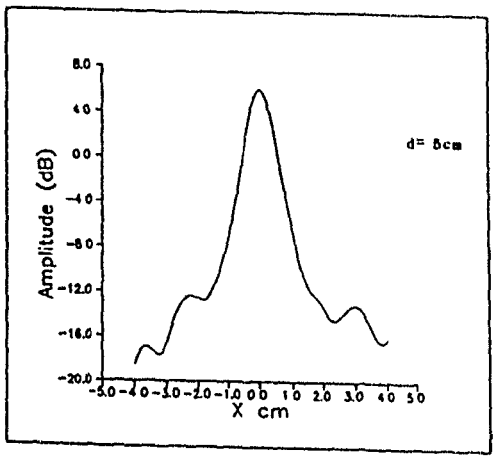

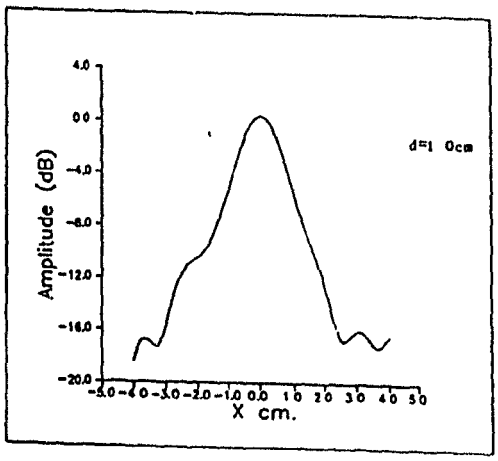

Figure (4.3): Measured probe output voltage versus x probe position, for the distances d=.2,.5 and 1. cm. indicated ($\approx 0.08, 0.2$ and 0.4λ).

Dipole probe #2 described in Appendix (B) is used in these measurements aligned along the x-axis to couple with the x-component of the electric field.

Phase information is also available from these measurements.

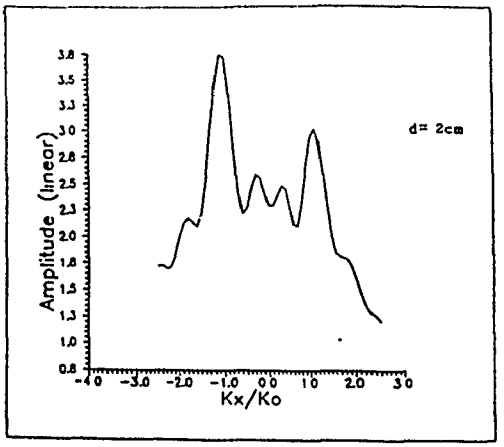

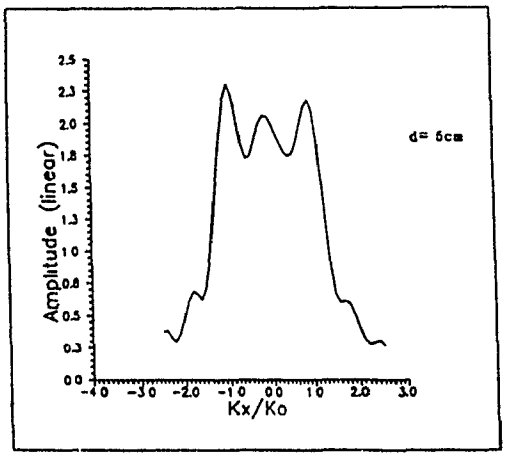

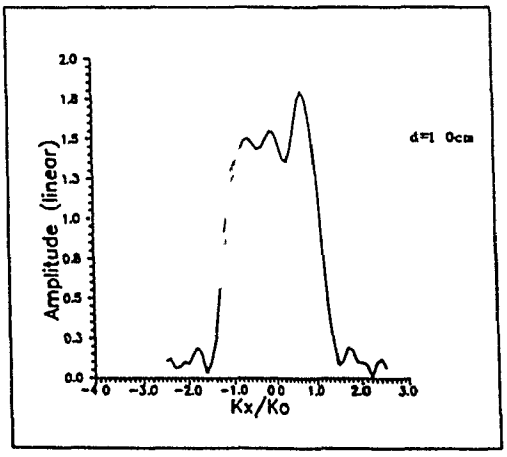

Figure (4.4): Linear amplitude of the x-component of the electric field in the spectral domain normalized to k_o. These field distributions are extracted from the phasor voltage measurements in Figure (4.3), with the distances d used in these measurements indicated. The phase information is also available.

The probe #2 model presented in Appendix (B) is used in the electric field extraction from the measured voltages.

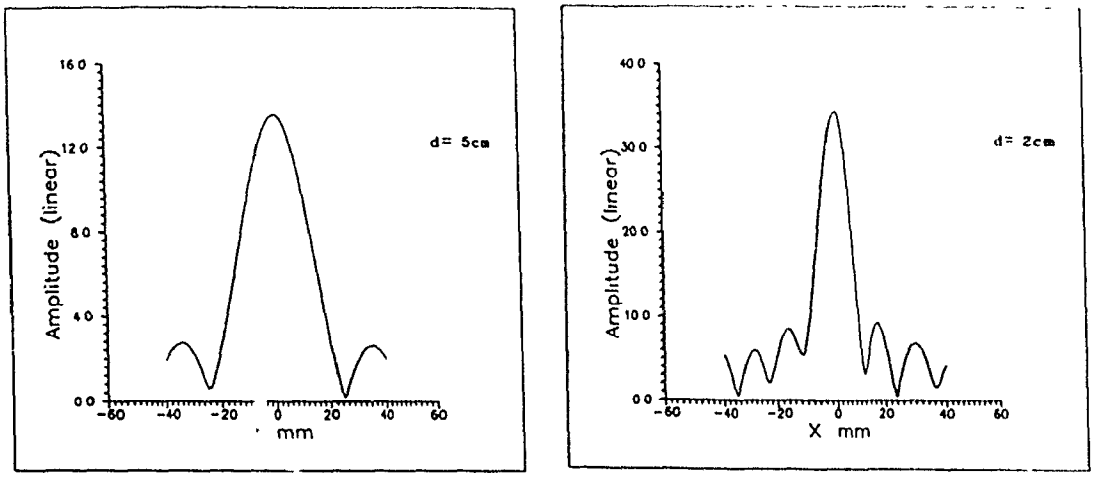

Figure (4.5): Relative linear amplitude of the x-component of the immediate electric field (z=0) in the space domain. These results were calculated from the measurements with distances d indicated. Phase information is also available from these calculations. This distribution is proportional to the y-directed line equivalent magnetic current.

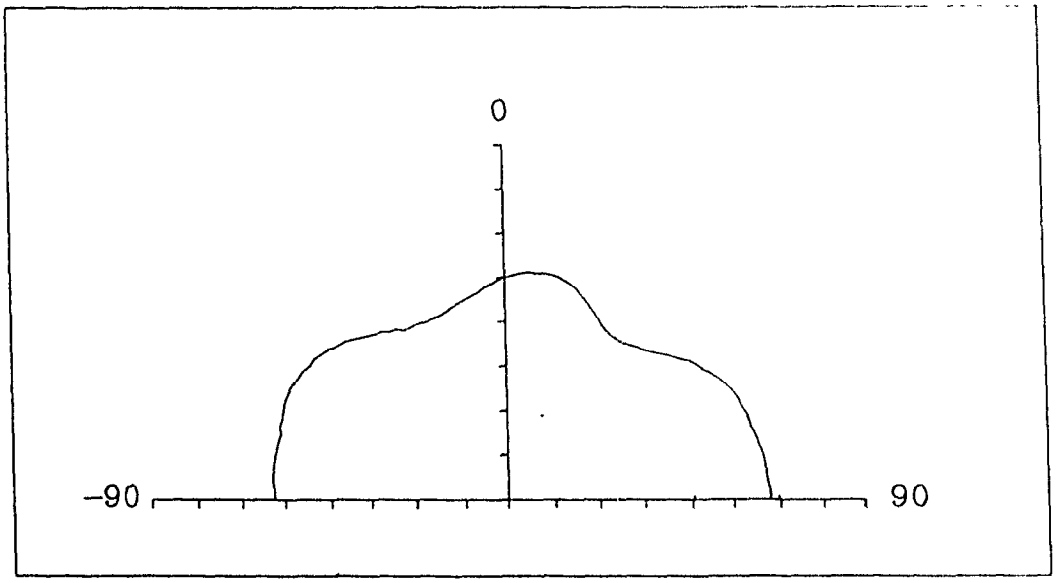

Figure (4.6): Far-field radiation pattern of the microstrip edge calculated from the phasor equivalent magnetic current distribution of figure (4.5). The d=0.5cm. measurement data is used in these calculations. Zero degree in this pattern corresponds to the positive z-axis and 90 degrees corresponds to the positive x-axis.

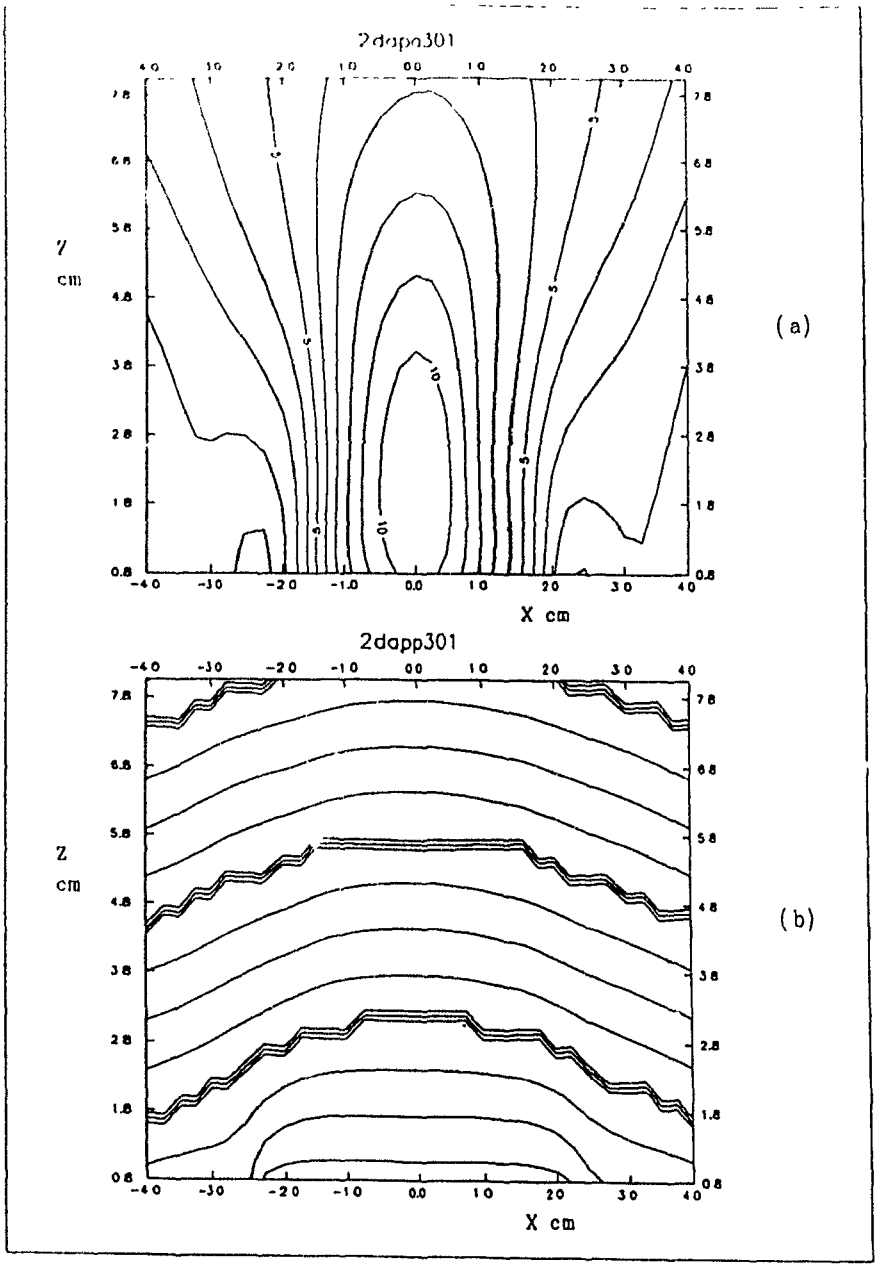

Figure (4.7): Calculated x-component of the electric field in a plane x-z (y=0), in an area surrounding the microstrip edge. The electric field is calculated at each point by integrating the contribution of the equivalent magnetic current lines. The d=0 5 cm. set of measurement data is used to obtain these currents.

a) Linear relative amplitude contour map, with contour interval of of unity and maximum contour of 10.

b) Phase contour map, with 90° contour interval.

4.1.4. Comments:

The advantage of probing the field in the vicinity of the approximate microstrip edge, and the subsequent use of the techniques of chapters two and three, is strengthened by the fact that there is no way of directly measuring the near or far-field for such a radiator. Although the problem of characterizing the external field for an infinite edge has no important application, it has a significant advantage for studying other configurations where a microstrip edge is the source of radiation, such as the microstrip patch antennas and microwave printed circuits. This section has established a methodology of dealing with the measurement of the external field of a microstrip edge and characterizing the field around it

The major conclusion drawn using the results of these experiments is that approximating the microstrip edge as a line magnetic current located along the edge is a fairly good one when only a single edge exists. This is evident by inspecting the immediate field of Figure (4.5), which proves that the source of radiation is centered at the edge, and the far-field radiation pattern of Figure (4.6), which shows that the radiation pattern versus ϕ is nearly uniform, indicating that there is only one line source of radiation, otherwise, there would be maxima and minima due to the interaction between the sources. The other observation from the experimental results, is that the effect of surface waves could not be measured in the region external to the dielectric using the available hardware and probes. This does not mean that the surface wave has absolutely no effect on the microstrip edge field, since it propagates within the dielectric and it will cause secondary radiation when it encounters an obstacle within, or the edge of the dielectric substrate. This latter phenomena has been detected experimentally, and will be shown in the next section.

4.2. Microstrip Patch Antenna Field Probing:

Microstrip, or printed patch antennas have gained widespread use as radiating elements for array antennas Their principle of operation seems straightforward, but the accurate analysis and prediction of their performance is a difficult task that occupies a significant amount of the current literature on antennas[55,56]. While their internal behavior can be approximated as a cavity with lossy walls, with the loss in the walls contributed by the radiation and the surface wave launching[54], the external behavior is rather complicated and partly described in the literature The reason is the unavailability of effective analytical tools for dealing with the open boundary around the patch edges. These edges consist of the transition from the patch and the conductive backing enclosing the substrate, to an open boundary replacing the patch, and the further complexity of the external interaction between the edges This has led to the development of numerical techniques of dealing with the microstrip radiator, using, in principle, the method of moments[57].

Experimental confirmation of the numerical results is based mainly on the agreement between the numerically predicted resonant frequency and input impedance with measured values The fact that this kind of a radiator is of narrow bandwidth, or resonant, implies that the input impedance is influenced mainly by the fields inside the patch which accounts primarily for the stored energy The region exterior to the patch, which the immediate, near and far fields of the patch are parts of, is only loosely coupled to the internal field under the patch surface The model confirmation, therefore, using only the input impedance measurements, may be unreliable when the external behavior of the patch is of major interest, especially when considering that the characterization of the external behavior is of primary importance in defining the coupling between the patch and the surrounding elements and the radiation pattern of an array.

The external behavior of a patch model can be confirmed using the radiation pattern measurement, but since the microstrip patch is a weak radiator with an inherently large supporting structure, direct measurement of the far-field would be corrupted by the scattering from the surrounding objects and the secondary radiation from the substrate edges. This latter statement is demonstrated by Figure (4.8) which shows significant radiation from the substrate edge which would certainly contribute to a measured far-field radiation pattern. The patch and the substrate is the same one used in the later experiments in this section Williams *etal.*[58] have considered this effect and managed to measure the far-field of a microstrip patch with considerable accuracy using information gained from the measurements of the radiation pattern in the back of the conducting

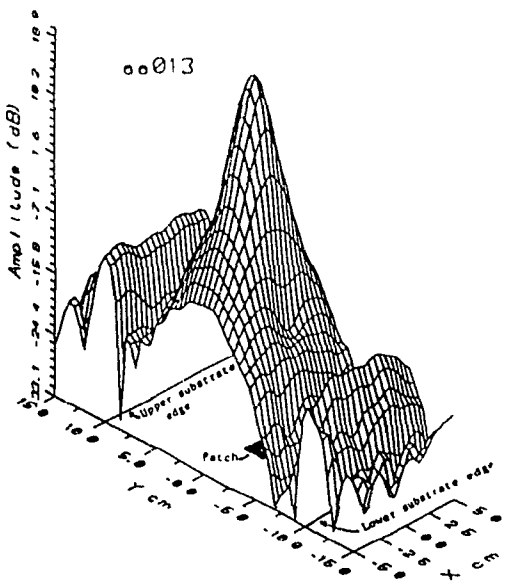

Figure (4.8): Demonstration of the secondary radiation from the substrate edge of a microstrip antenna. The antenna used in this experiment is that of Figure (4.10) operated at 11.65 GHz. Dipole probe #1 in Appendix (B) is utilized and oriented to couple mainly with the ρ-component of the electric field, with the distance d=1 cm. between the antenna and scanning planes.

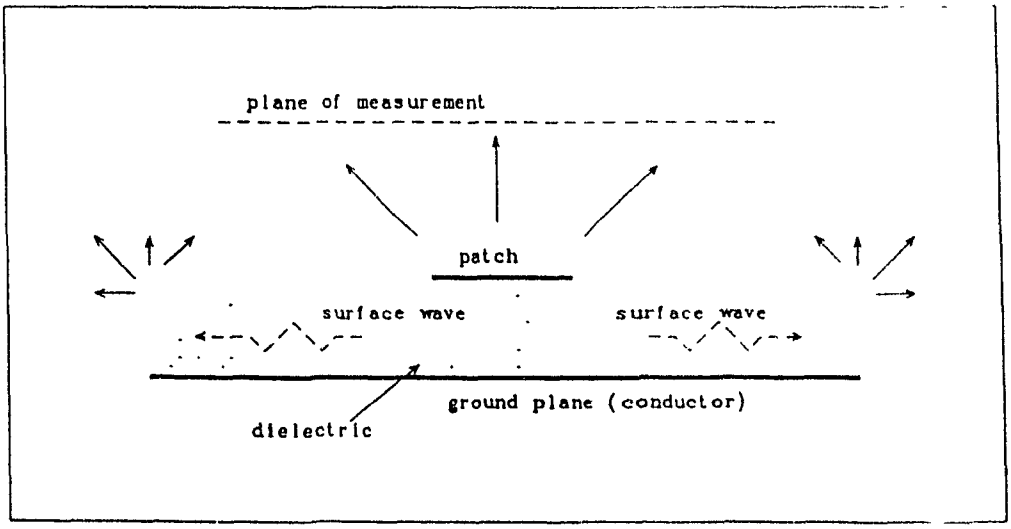

Figure (4.9): The plane of measurement and its dimensions are chosen such that the measured fields will be mainly contributions of the microstrip patch. This will weaken the effect of secondary and stray radiation from the dielectric substrate edges and from the supporting structure, on the final measurement results.

ground plane backing the substrate. This technique imposes restrictions on the supporting structure and considers only one secondary radiation phenomenon. In addition, only the radiation pattern can be recovered for this case In this section, the external behavior of a microstrip patch is examined by probing the field in the vicinity of the patch, where the field is dominated by the contribution of the patch itself, to obtain an equivalent current model that represents the external field of the patch. The planar measurement offers in this case a unique advantage of the ability to measure close to the patch, while avoiding the contribution from the secondary radiation sources, as demonstrated by Figure (4 9) In the alternative cylindrical or spherical measurements, the patch and the supporting structure has to be enclosed by the surface of measurement, which makes the contribution of the these sources unavoidable. Further reduction of the effect of the secondary radiation is affected by the truncation of the equivalent radiating sources plane as discussed in Section (2 7)

The planar probing of the field close to the microstrip radiator has the additional advantage of the possibility of transforming the field back towards the patch surface, giving a quantitative idea about the immediate field around the radiating patch, within the limitations discussed in chapters two and three. This will facilitate the use of the techniques, described here, for locating and measurement of fields surrounding other kinds of microstrip structures, such as discontinuities and junctions, which gives an idea about the, usually undesired, radiation from them In the following sub-sections, the experimental procedure is described with a presentation of the experimental results.

4.2.1. Description of the Microstrip Radiator and Preliminary Investigations:

The rectangular patch used in the experiment is shown in Figure (4.10). The patch is printed on RT/Duroid 5880 microwave dielectric substrate, $\epsilon_r = 2.2 \pm .02$, and thickness 0.7 mm., with conductive backing, or ground plane. The patch was designed to resonate at 11.6 GHz. using the formulation given by Munson[52], which is used also in locating the feed point to give proper matching with the 50Ω feed line The patch is designed to radiate a main, y-polarisation and a cross, x-polarization in the boresight direction. In the following experiments, the frequency of operation is chosen such that maximum radiated power in the boresight (z) direction for the main polarized component of the radiated field results. Using the monopole probe #3 of appendix (B), the immediate field component normal to the surface of the patch is scanned to obtain a contour plot of that component as shown in Figure (4 11) This figure shows asymmetry of the modes excited inside the patch. This can be attributed to the relative thickness of the patch

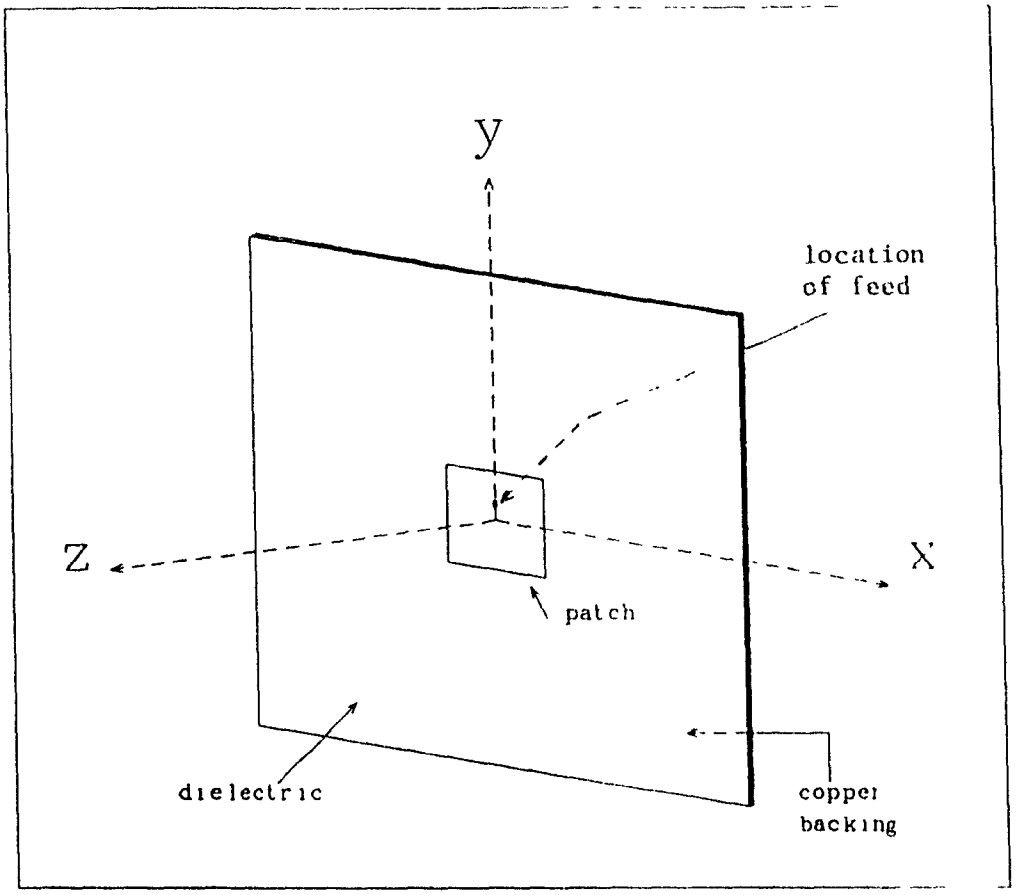

Figure (4.10): Rectangular patch microstrip antenna used in the experiments. The patch designed dimensions are 13.4x8.9 mm. in the x and y respectively to resonate at 11.65 GHz. The substrate x and y dimensions are 25.7 cm. and 20.4 cm. respectively. The substrate dielectric is RT/Duroid 5880 (dielectric constant of 2.2) with 0.7 mm. thickness. The patch is probe fed through the substrate copper backing at the point x=0. and y=2.5 mm. This is supposed to match the feed probe to the 50Ω feed line at 11.6 GHz.

The origin of the coordinate system (x=y=z=0) is located at the centre of the patch surface which coincides with the centre of the rectangular substrate. This figure is not drawn to scale.

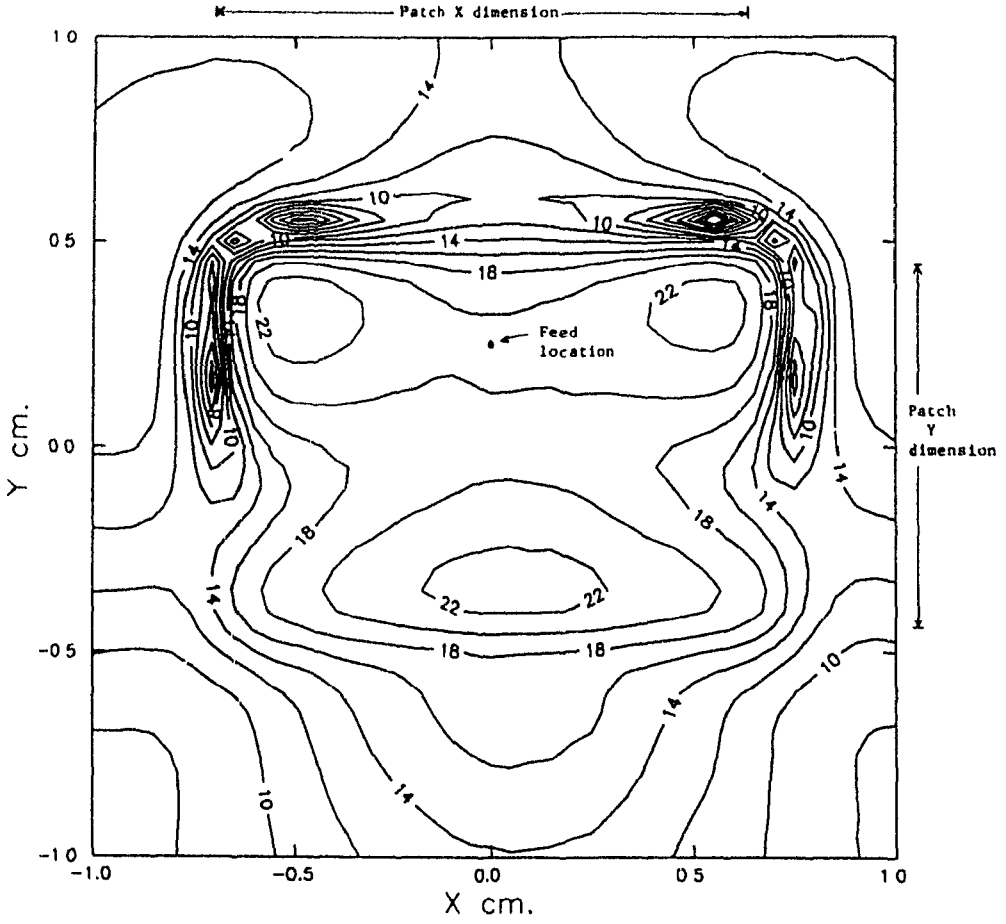

Figure (4.11): Contour plot of the relative amplitude of the z component of the electric field measured in dB in the proximity of the patch surface at 11.65 GHz. Contour level interval is 2 dB and the maximum contour level is 22 dB. Phase information is also available from the measurement. Monopole probe #3, Appendix (B) is used in the measurements, with the monopole element aligned along the z-axis. The output voltage of the probe is approximated as proportional to the electric field component normal to the microstrip patch plane, within the limitations discussed in Appendix (B).

The distance between the patch and scanning probe centre is 1.5 mm. The patch is located within an area described as: $-6.7 \text{ mm.} < x < 6.7 \text{ mm.}$ and $-4.5 \text{ mm.} < y < 4.5 \text{ mm.}$, as indicated.

(.03λ) which is three times thicker than the maximum thickness for which a patch internal field can be approximated by that of a two dimensional cavity. This was not of major concern in this work, since the interest is in measuring the patch exterior field as it actually exists.

Some planar measurements were conducted during early stages of this work close to the patch, within one wavelength, using measured probe data of Section (3.4) for field extraction from probe #1 output voltage. The measured field data was transformed into the spectral domain, and the far-field radiation pattern was calculated from the spectral domain representation[41]. The Fourier transforms of the main and cross polarized measurements are shown in Figure (4.12) versus the normalized tangential wave numbers, and the consequent radiation patterns are shown in Figure (4.13). The problem of calculating the radiation pattern directly from the spectral representation of the field, is demonstrated in these figures by noticing the irregular behavior of the spectral representation at $k_x = k_y = 0$, and the radiation pattern at the boresight direction. This is due to the non-directive nature of this radiator, which leads to the significance of coupling and truncation errors described in Section (2.7). This necessitates the employment of the equivalent currents approach towards defining the field exterior to the patch. The consequent work based on the evaluation of the equivalent currents representation is shown in the next sub-section.

4.2.2. Determination of Equivalent Currents and External Fields:

The measurements of the co-polar, (y), and the cross-polar, (x), components of the field at close proximity to the surface of the patch (2 mm $\approx .08\lambda$), are shown in Figure (4.14). These pictures give a qualitative idea about the immediate field structure of the patch. Further elaboration using this data is unreliable due to the proximity of the probe to the patch. The probe used in these and the following experiments is the 0.9 cm. balanced dipole probe #2 of Appendix (B). These figures can be compared to those obtained be Levine[15], taking attention that they are presented here in dB scale.

Planar scans on planes parallel to the patch surface were conducted, with progressively larger distances of 0.5, 1 and 2 cm., ($\approx 0.2, 0.4$ and 0.8λ) for the operating frequency of 11.68 GHz. The electric field values were extracted from the probe #2 output, using the probe model of Appendix (B) and the theory presented in Chapter Three, after inverse Fourier transforming the measured voltage. The equivalent magnetic current model is chosen to represent the patch for two reasons; First, the patch can be physically described as an aperture radiator that can be replaced by equivalent magnetic currents. The use of electric current sources will cause the dispersion of the equivalent currents over larger area as stated earlier. This necessitates the measurement of the tangential

electric field to the plane of measurement to gain a well conditioned evaluation of the sources over a wider range of modes as demonstrated by Section (2.4). The second reason is the fact that the dipole, i.e wire, probe is used in the measurement for its practical advantage The electric field components tangential to the plane of measurement are transparent through the measured voltage for the entire radiation circle and extend to the evanescent region as demonstrated in Section (3 3)

The maximum tangential wave numbers employed in the inversion are estimated using Figure (2.4) Considering the first set of measurements at a distance of 2λ, shown in figures (4.15-a) and (4 15-b), the maximum reliably measured tangential wave number $k_{t max}$ is approximately $1.8k_o$, which implies the possibility of using some vanescent modes towards the evaluation of the equivalent sources. The results of the calculation of equivalent magnetic currents are shown in Figure (4 16) using this maximum wave number Figure (4 17) shows the equivalent magnetic currents using a larger $k_{t max}$ of $2k_o$, which exceeds that determined by the criterion used for reliable measurement in Section (2 4), but shows that the employment of a larger range of evanescent modes can reveal further details of the immediate field structure, but with larger quantitative uncertainty

The evanescent modes cannot be employed reliably in the other two measurements (surface of measurement distances of 0.4 and 0.8 λ, respectively), as evident from Figure (2 4). The two measurements, however, gave similar equivalent magnetic current distributions at the patch surface. This indicates that the multiple reflections between the patch and the measuring probe are negligible. Figure (4 18) shows the equivalent magnetic currents using the 1λ distance of the plane of measurement. This magnetic current data can be used to calculate the near and far-fields radiated from the patch. The reactive fields surrounding the patch cannot be calculated from these currents because of the exclusion of the evanescent modes when calculating them.

The electric field was calculated from the magnetic current distribution of Figure (4 18), at a plane 10 cm away from the patch plane for both polarizations. The magnetic current is integrated over a truncated aperture of 8 cm.X 6 cm. on the patch plane, using Equation (2 1). The resulting fields are shown in Figure (4.19), compared with the electric field measured at the same plane using the short dipole probe #2 raw measurement data, which are assumed, for the distance involved, to be approximately proportional to the incident electric field. The distance of 10 cm. ($\approx 4.\lambda$) falls into the far-field region of the radiator according to Section (1.4).

The near-field of the patch is evaluated in a similar fashion from the equivalent magnetic current distribution. Figure (4.20) shows the main polarized field calculated on a plane (y-z) perpendicular to the patch plane, compared to measured values on the same plane. This plane passes through the near and far-field regions of the patch.

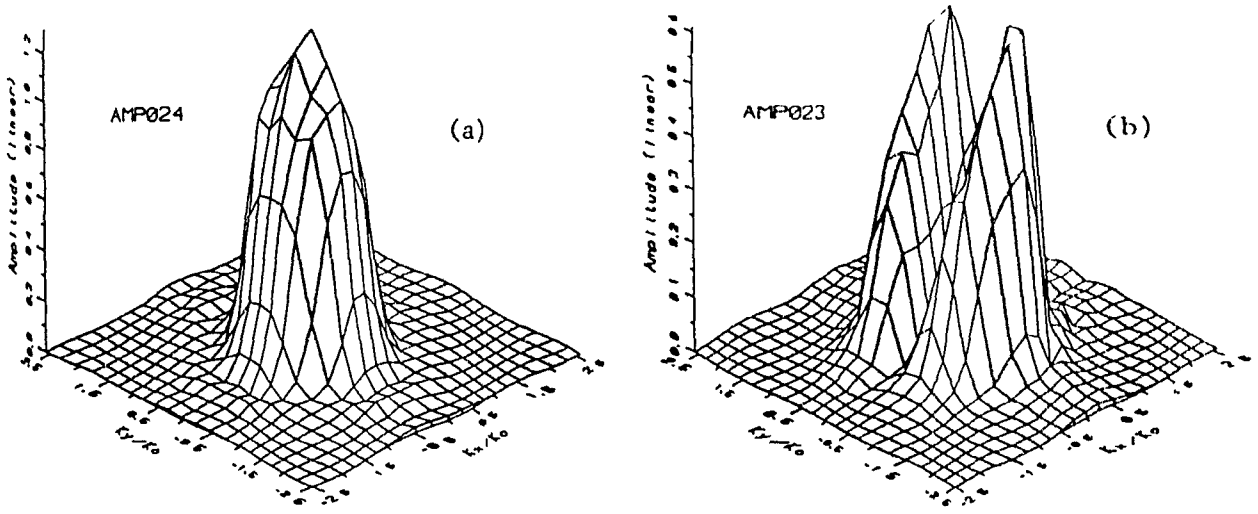

Figure (4.12): Planar measurements were carried out at 11.65 GHz., with a distance d=1.0 cm. between the patch and measurement planes, and 10.x10. cm. dimensions of the plane of measurement. Dipole probe #1 is used in these experiments. The surface plots shows the relative linear amplitude in the normalized spectral domain of:
a- Main polarized (y) component of the electric field distribution.
b- Cross polarized (x) component of the electric field distribution.

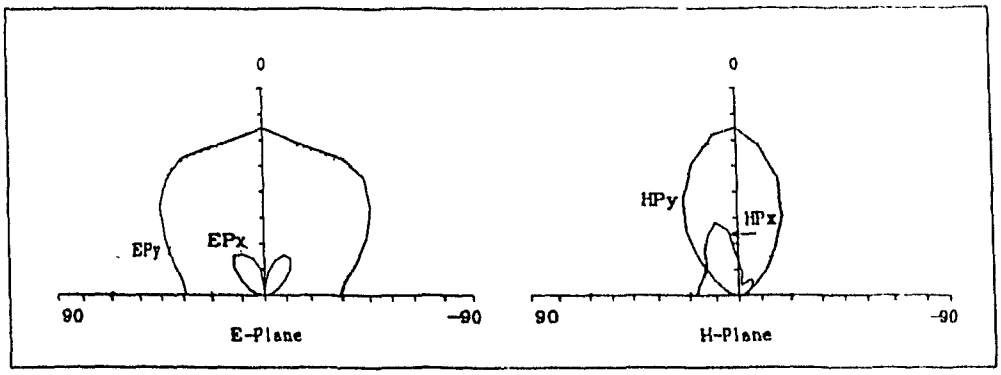

Figure (4.13): Sections of the far-field radiation pattern evaluated from the spectral domain field distributions of Figure (4.12).

EPy= Main polarization component in the E-plane (y-z).
EPx= Cross polarization component in the E-plane.
HPy= Main polarization component in the H-plane (x-z).
HPx= Cross polarization component in the E-plane.
(**HPx** is shown here multiplied by 10)

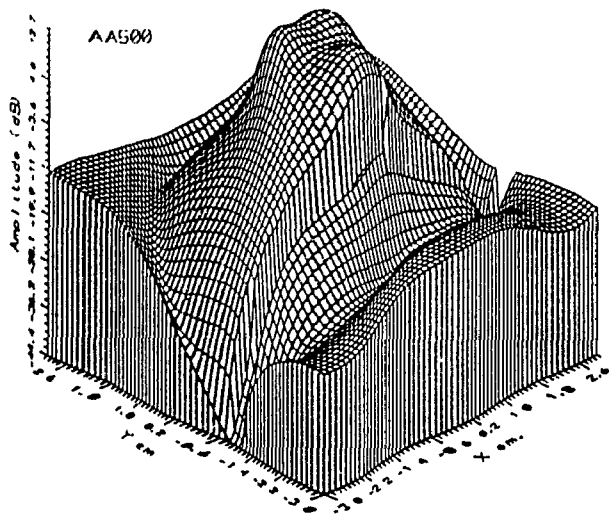

(a)

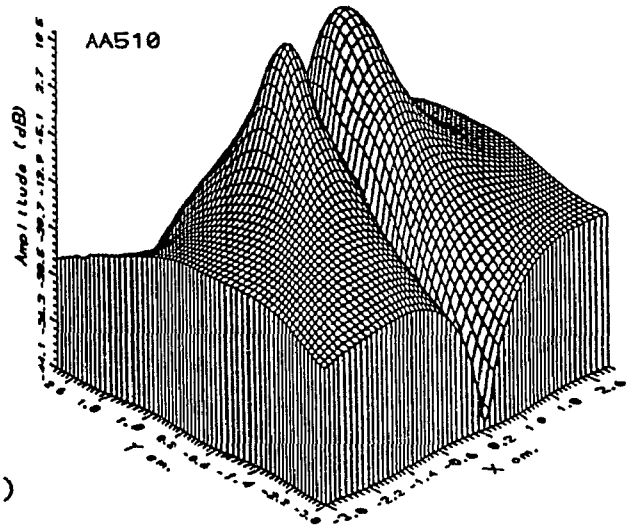

(b)

Figure (4.14): Measurement at a plane close to the microstrip patch plane:

a) Dipole probe #2, Appendix (B) oriented along the y axis to couple with the main polarized electric field component.

b) The same dipole oriented along the x axis to couple with the cross polarized electric field component.

Only amplitude data (in dB scale) is shown here, but the phase data is available from the same measurement. The distance d between the microstrip patch and measurement planes is 0.2 cm. ($\approx 0.08\lambda$) at 11.68 GHz.

The irregular behavior of part (a) of this figure between y=-0.7 cm. and -1.3 cm. is due to equipment failure during scanning, which is tolerated here because no further calculations were made using this data.

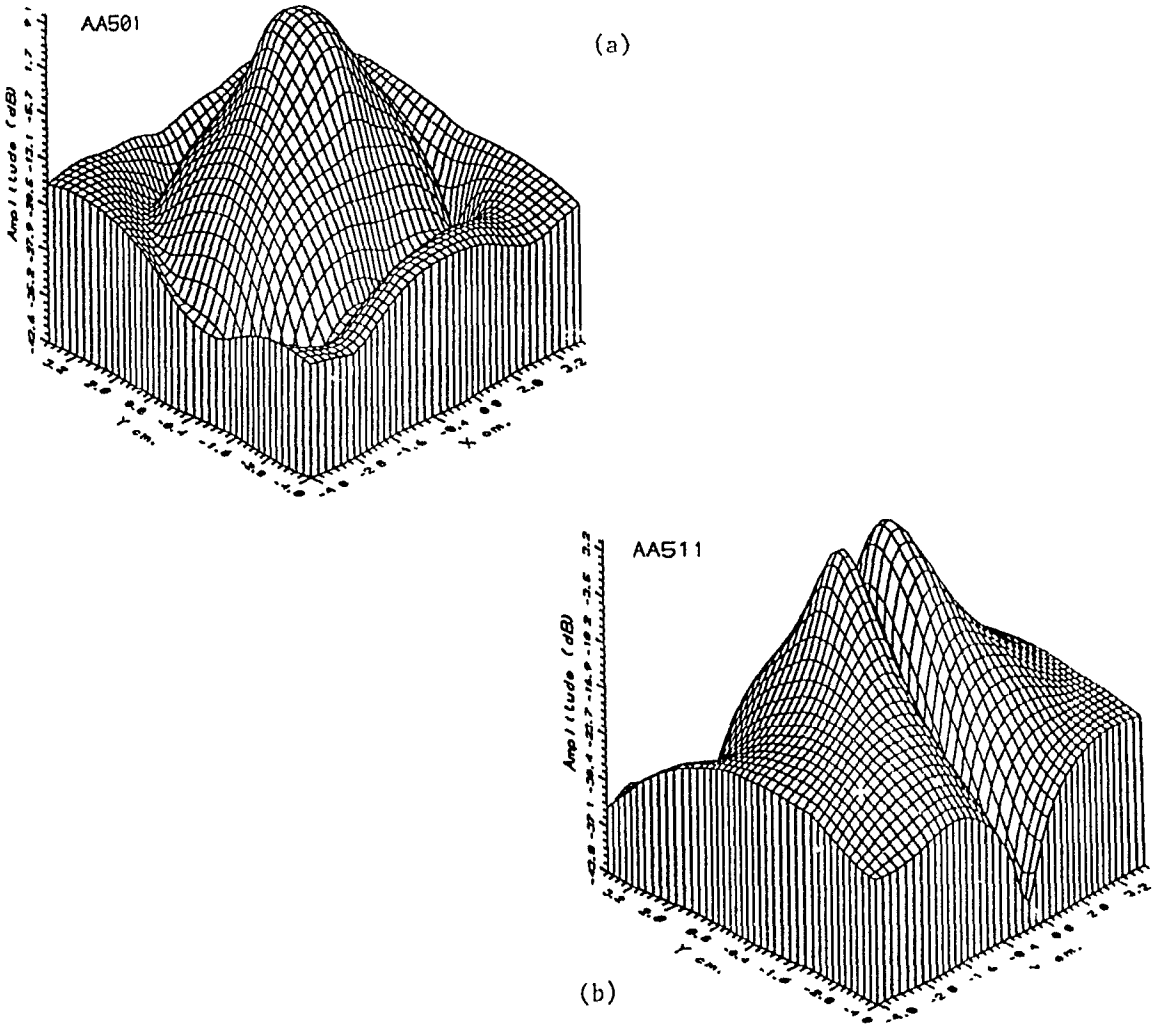

Figure (4.15): Planar measurement at a z distance between the microstrip patch and measurement planes ($=d$) indicated. The output amplitude is shown here in dB scale, and the dipole probe #2 is used in this and all the remaining measurements, and the frequency of operation is 11.68 GHz.

a) d=0.5 cm. ($\approx 0.2\lambda$) main polarization.
b) d=0.5 cm. cross polarization.

(continued next page)

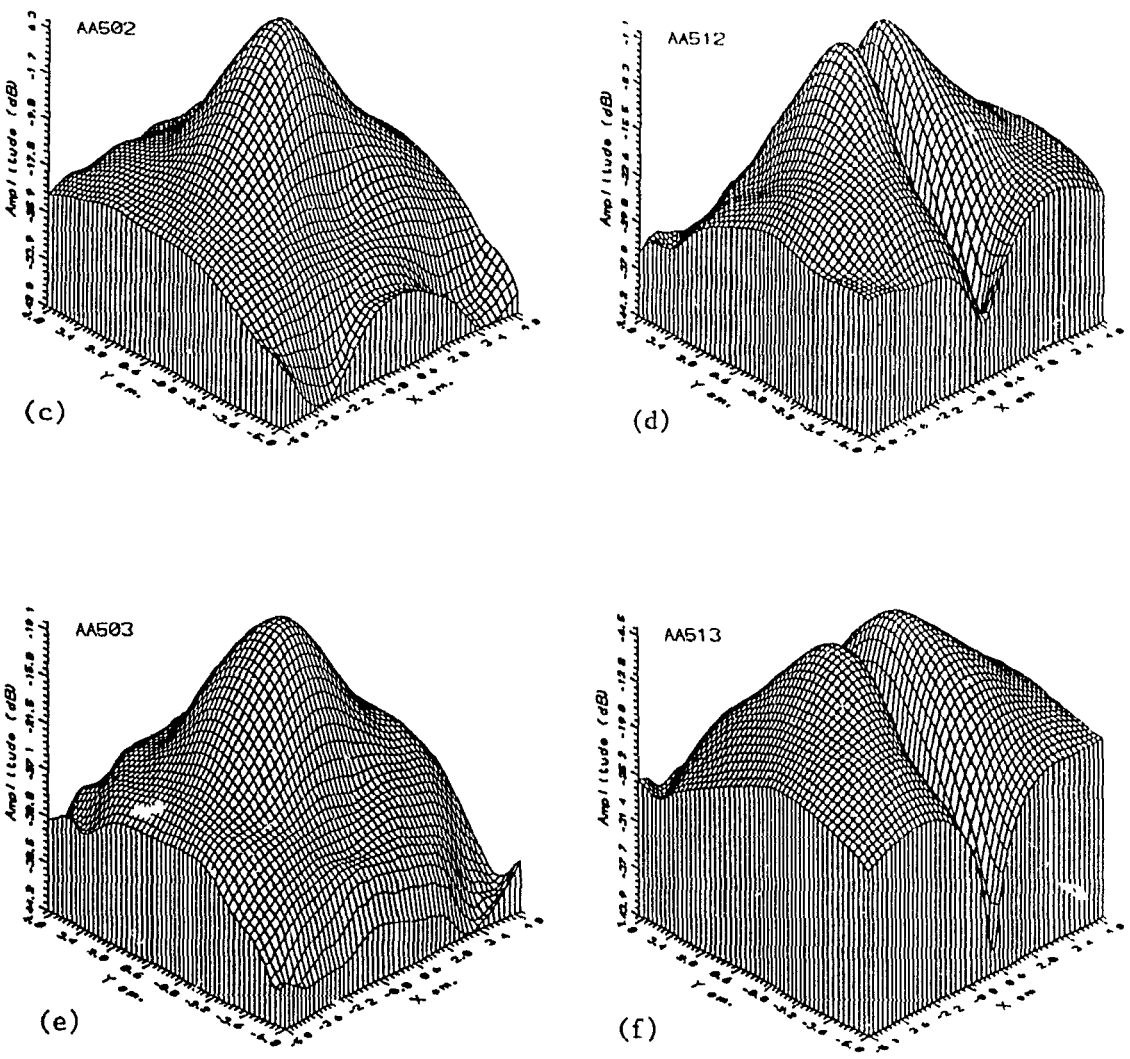

Figure (4.15):

c) d=1.0 cm. ($\approx 0.4\lambda$) main polarization.
d) d=1.0 cm. cross polarization.
e) d=2.0 cm. ($\approx 0.8\lambda$) main polarization.
f) d=2.0 cm. cross polarization.

The main and cross polarization indicates the orientation of the dipole probe element along the y and x axis respectively.

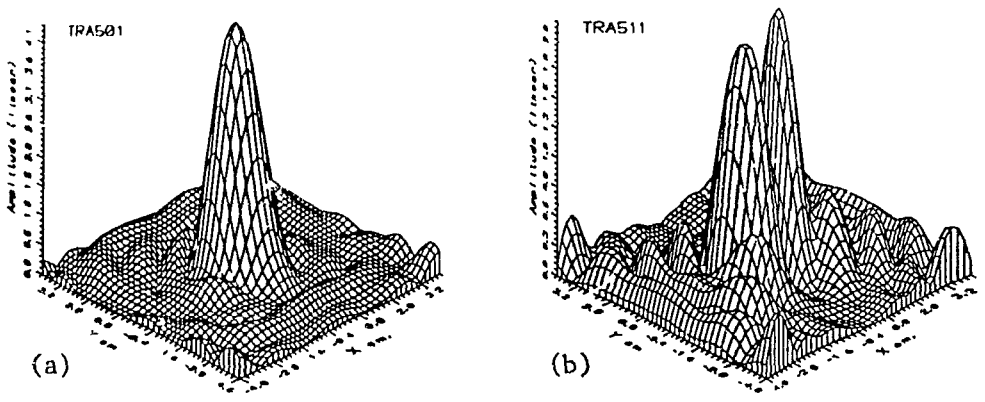

Figure (4.16): Equivalent radiating magnetic currents at the microstrip patch plane. Amplitude distribution is shown here in linear scale. The spectral domain was truncated to include only modes with $k_t = \sqrt{k_x^2 + k_y^2} \leq 1.3k_o$ (i.e. $k_{tmax} = 1.3k_o$).

a) Main polarization (x component of the current distribution).
b) Cross polarization (y component of the current distribution).

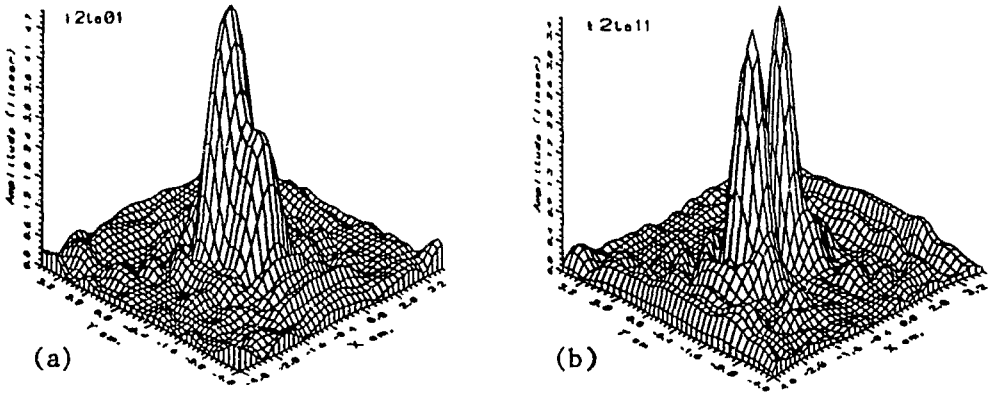

Figure (4.17): Same as figure (4.16), but with $k_{tmax} = 2.0k_o$.

a) Main polarization.
b) Cross polarization.

The result in the above figure should be compared to the immediate field measurement of figures (4.14-a) and (4.14-b).

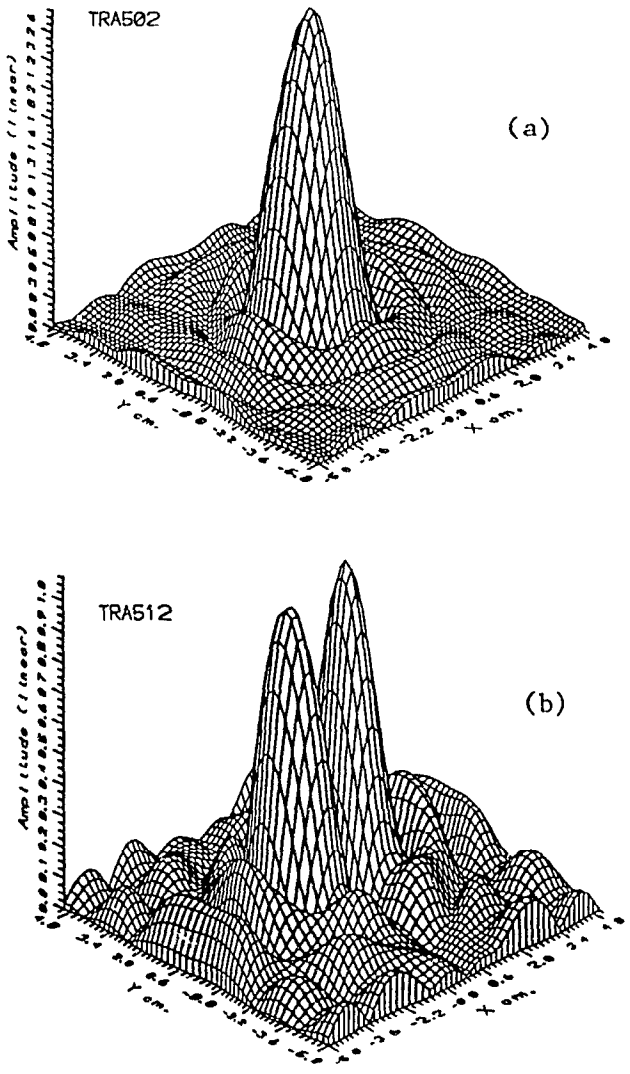

Figure (4.18): Amplitude distribution of the equivalent magnetic currents at the microstrip patch plane. These currents are calculated from the measured amplitude data of figures (4.15-c) and (4.15-d) and the corresponding measured phase data. The spectrum is truncated in the calculation such that $k_{tmax} = k_o$.

a) Main polarization
b) Cross polarization.

These currents are utilized in calculating the exterior electric field of the microstrip patch in the next two figures.

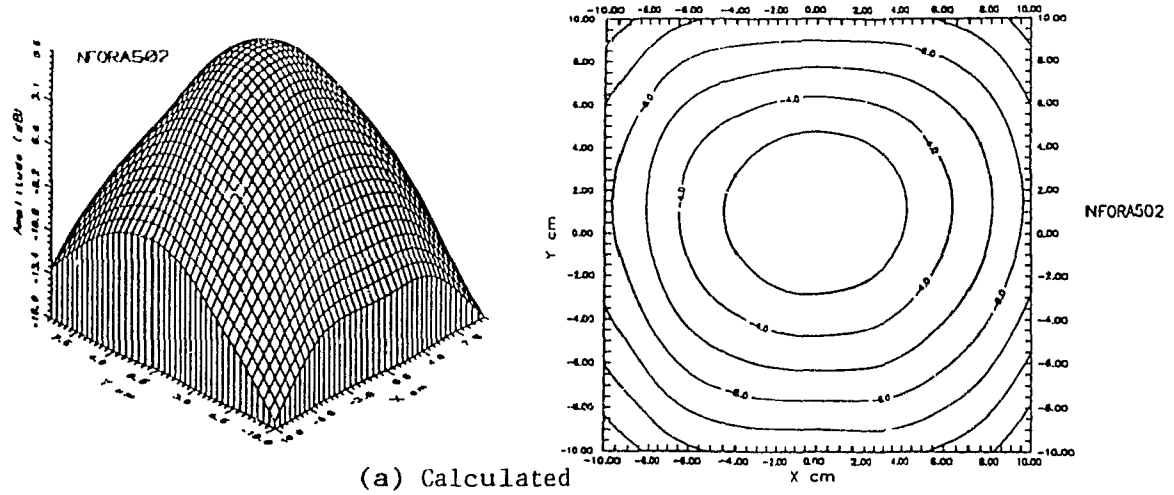

(a) Calculated

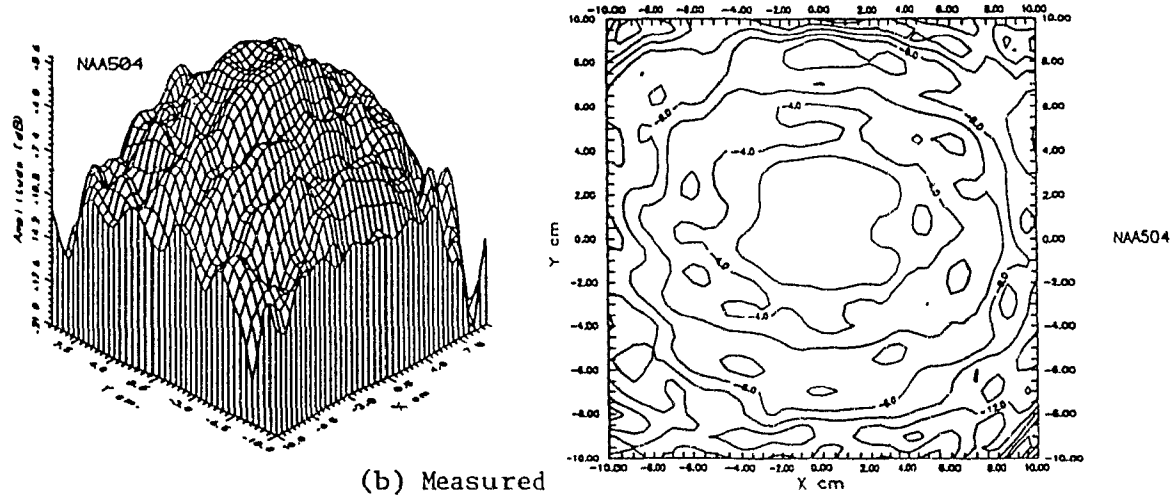

(b) Measured

Figure (4.19). Surface and contour plot of the normalized electric field distribution at a plane 10 cm away and parallel to the microstrip patch plane.

a) Main polarized (y) component calculated from the equivalent magnetic current distribution of Figure (4.18), with the current distribution truncated to within -4 cm $<x<$ 4 cm. and -3 cm $<y<$ 3 cm

b) Main polarized component measured directly with dipole probe #2, appendix (B), oriented along the y-axis.

Contour maps have maximum contour level of 0 dB and 2 dB contour intervals.

(continued next page)

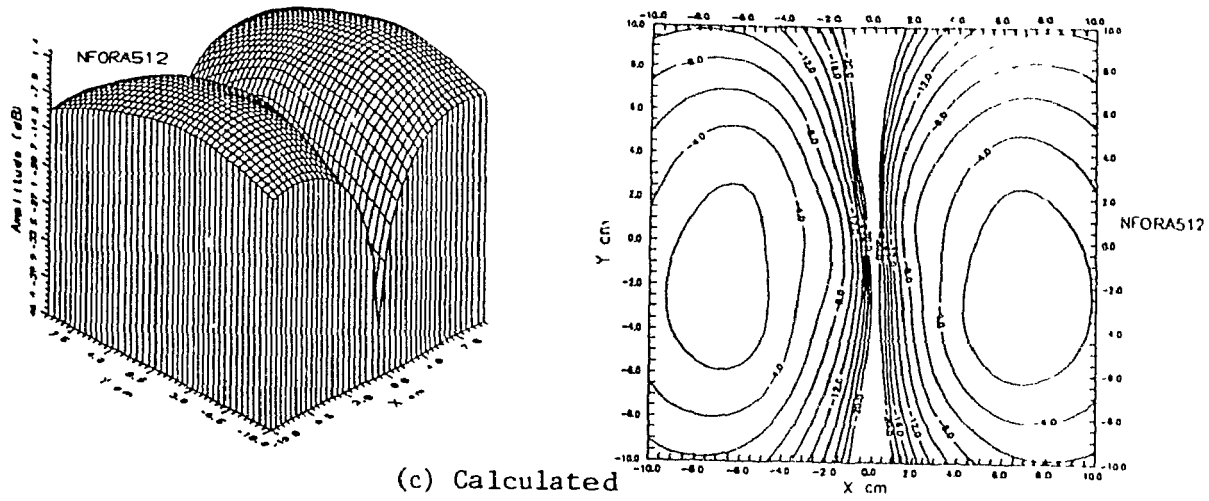

(c) Calculated

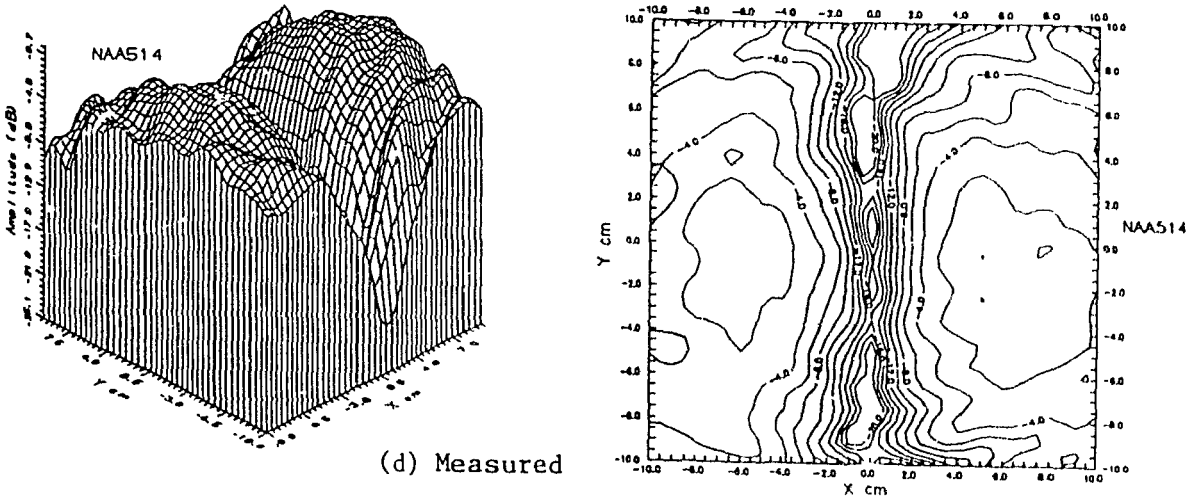

(d) Measured

Figure (4.19):

c) Cross polarized (x) component calculated from the equivalent magnetic current distribution of Figure (4.18), with the current distribution truncated to within -4 cm. $< x <$ 4 cm. and -3 cm $< y <$ 3 cm.

d) Cross polarized component measured directly with dipole probe #2, Appendix (B), oriented along the x-axis.

Contour maps have maximum contour level of 0 dB and 2 dB contour interval.

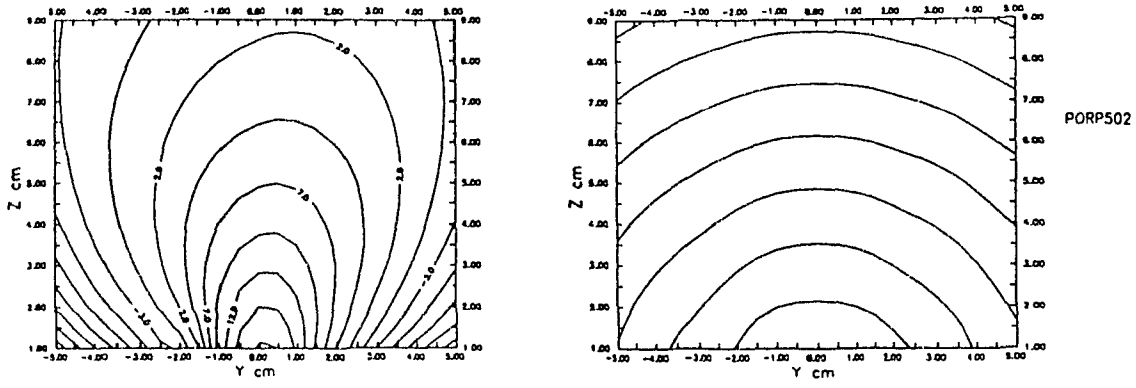

(a) Calculated

Amplitude

Phase

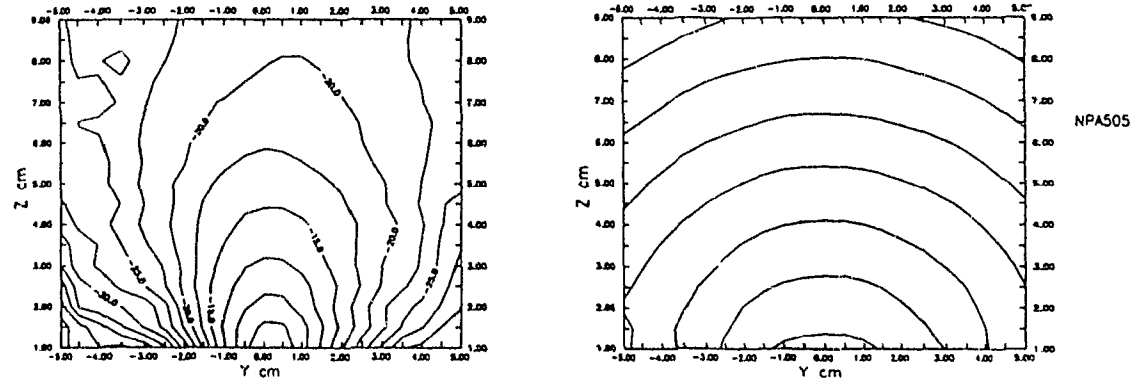

(b) Measured

Figure (4 20): Main polarized electric field distribution at the y-z plane ($x=0$). The microstrip patch centre is $x=y=z=0$ as shown in Figure (4.10).

a) Calculated from the equivalent magnetic current of Figure (4.18) truncated to within -4 cm. $<x<$ 4 cm. and -3 cm $<y<$ 3 cm. Maximum amplitude contour is 17 dB and the contour interval is 2.5 dB. Phase contour interval is 180°

b) Measured directly with the dipole probe #2, Appendix (B) oriented along the y-axis. Maximum amplitude contour is -5 dB and the contour interval is 2.5 dB Phase contour interval is 180°

4.2.3. Comments:

Comparison between figures (4.14) and (4.17) shows that the utilization of the evanescent modes has revealed qualitatively correct information about the immediate field structure of the patch The existence of evanescent modes in the measured fields has been usually attributed to the multiple scattering between the probe and the radiator, which will cause the distortion of the measurement, and consequently, coupling between the evanescent and the radiation region of the plane wave spectrum The above figures prove that, for the case under consideration, the effect of this distortion is less significant than the actual evanescent modes contribution of the radiator external fields

Figure (4.19) shows the resemblance between the far-field calculated from the equivalent current model of the radiator, and that measured directly, in and around the region of peak field values The equivalent current model is evidently superior in defining the electric field at regions where it has a lower level, for which the measured field is highly corrupted by noise. This can be attributed to the error filtering gained by spectral and space domain truncations described in Section (2 7).

The same above argument applies to the results shown in Figure (4 20). In this case, the directly measured field is unreliable at the two extremes of the r-z plane of measurement. In the lower region, which is close to the patch, the probe averaging effect might distort the space description of the field (third case in Section (3 1)), while this effect is not as significant in the upper region, far from the radiator (second case in Section (3.1)) However, the measurement in this region is corrupted by noise because of the low field level in that region This leaves the middle region of the plane described above for qualitative comparison of the results shown in Figure (4 20)

In comparison with the single edge results of Section (4 1), it can be observed from the results of Figure (4 20), that the radiated fields from this patch are not different in nature from these originating from a small aperture, and the edge radiation is not detectable. This may be attributed to the small dimensions (in wavelengths) of the patch

4.3. Horn Cluster Field Probing:

The third radiator considered is a horn cluster of a type used as a feed for satellite reflector antenna It consists of eleven individual horns with co-planar apertures, as shown in Figure (4.21) The horn cluster is an illuminating feed for a reflector antenna on board a communication satellite designed to have a certain footprint, or illumination pattern, on the earth surface The footprint is determined by the combination of field structure of the feed and the shape of the reflector surface The measurement of the exterior field quantities of this feed structure can be useful in two aspects in checking the cluster performance in keeping with the design, and in collecting information that will facilitate the subsequent design of the reflector surface shape using measurement based data

In this section, an objective is set to model the feed, so that the field on an arbitrary reflecting surface can be calculated efficiently. The field is measured in a plane close to the feed, where the tangential electric field distribution is localized enough, so that reasonable plane dimensions can be chosen. The techniques of chapters Two and Three are then used to extract the electric field quantities, to transform then into an equivalent magnetic current distribution on the aperture plane and to look into ways of modeling the feed from this information Field measurements at distances close to the potential location of a reflecting surface are then performed for comparison with the field calculated using the feed model, and thus to evaluate its accuracy

It can be argued that it might be sufficient to use the radiation pattern, measured using a conventional far-field range, to represent the feed in the context of its interaction with the reflecting surface The sensitivity of the measured far-field phase to the measurement errors because of the large distances involved was indicated in Chapter Three. The phase of field components on a reflector surface is the principle factor in determining the far-field of the antenna systems[59] In addition, the field in the far-field region is dominated by a single point (k_x, k_y) in the plane wave spectrum of the radiated field[10], while this is not necessarily true for typical distances between a feed and a reflector surface Thus, the objective is to find a feed model from the measurements that can predict the field in the near-field region of the feed, where the reflector is located, rather than the far-field.

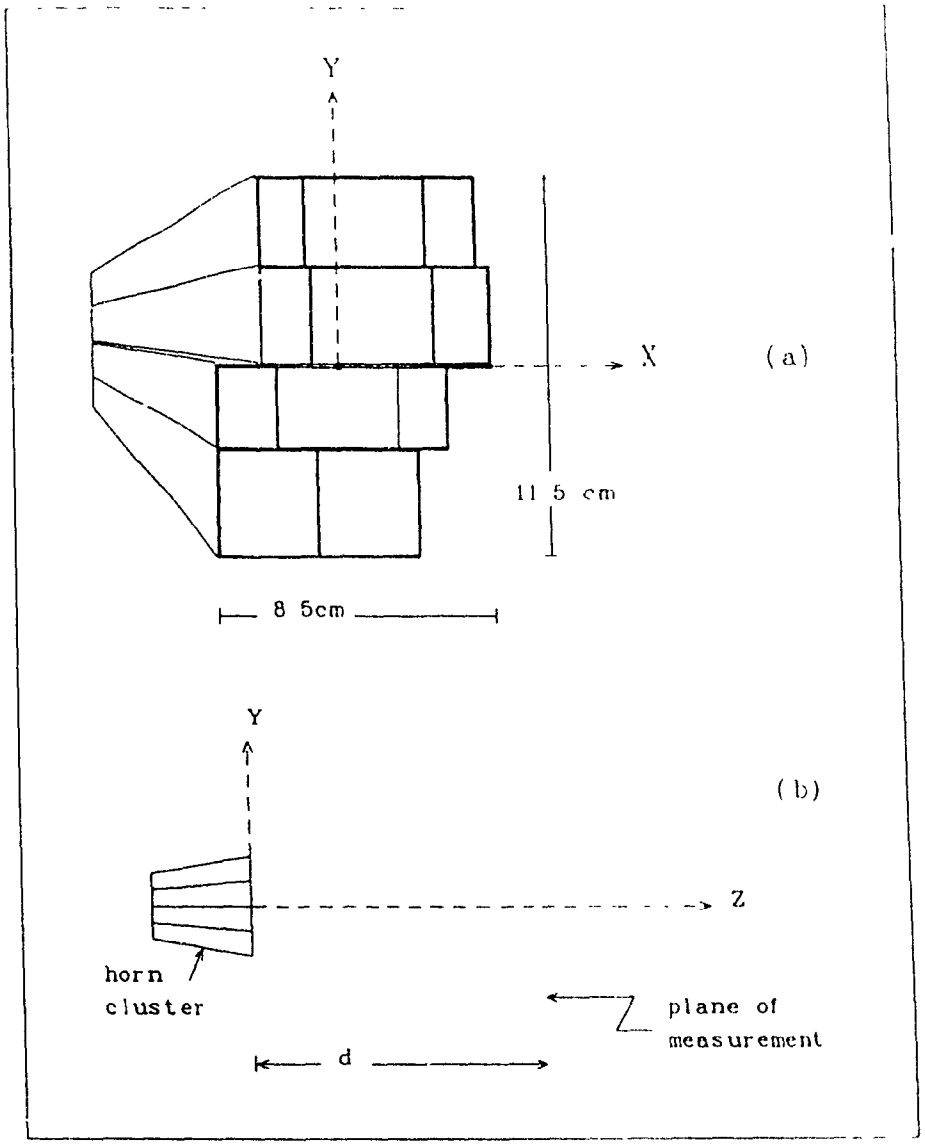

Figure (4.21):

a) Schematic diagram of the feed horn cluster The cluster consist of eleven horns with co-planar aperture. The aperture plane (z=0) is drawn to scale and the origin (x=y=z=0) is chosen arbitrarily at a point on the aperture plane indicated.

The aperture electric field has x and y main and cross polarization components respectively

b) Planar measurement configuration: The location of the plane of measurement (z=d) relative to the horn cluster.

4.3.1. Description of the Experimental Procedure:

Initially, a few exploratory measurements were taken with a low spatial sampling rate, in order to gain some information about the field structure around the horn cluster, and to define the dimensions and distance of the plane of measurement d from the horn's apertures. The measurements were conducted at an operating frequency of 11.6 GHz, ($\lambda = 2.58$ cm). The criterion used to choose the size of the plane of measurement was to include all the area for which the magnitude of the measured field is higher than -30 dB referenced to the peak. Naturally, the larger the distance d, then, the multiple scattering between the horn cluster and the probe will be lower, but larger dimensions of plane of measurement are required. These dimensions chosen are also influenced by the size of the scanner available. The resulting choice from these preliminary measurement was a distance d=5 cm ($\approx 2\lambda$), and plane of measurement with 60 cm x60 cm dimensions. The field sample spacing was 0.6 cm ($\approx .23\lambda$). It is evident, from the definition of the Nyquist rate in Section (2.5), and the fact that the evanescent field modes have decayed sufficiently at a two wavelengths distance from the radiator[3], that a 1.29 cm field sampling rate is enough to collect complete information about the measured field. The over-sampling is chosen to produce smooth measured field structure maps at the plane of measurement.

The field was measured using the short dipole probe #2 described and modeled in Appendix (B). The same probe is used to measure the field at a distance d of 80 cm from the horn cluster aperture, on a plane of dimensions 80 cm x80 cm at 1 cm field sampling intervals (d=60 cm for the cross-polarized measurements). The latter set of measurements was intended for comparison with the electric field calculated from the equivalent magnetic currents at the horn cluster aperture (and is generally in the region where a reflector would be placed). All these measurements were repeated for two probe orientations, co-polar (r) and cross-polar (x), as dictated by Section (2.4) as necessary for the evaluation of the equivalent magnetic current distribution.

Figure (4.22) shows the amplitude of the measurements at d=5 cm, for both probe orientations in dB scale. The phase was also measured at the same points. These data are used as the starting point in the evaluation of a model for the horn cluster.

4.3.2. Measurement Data Processing and Presentation of Results:

Four possible modeling procedures of the horn cluster were examined here:
1. The use of contributions from each horn individually to calculate the external field by simple superposition. This representation proved unsuccessful, but is briefly documented here as a useful experience.

2. The utilization of the spectral domain representation extracted from the measurements to calculate the space domain exterior field of the radiator. It was shown in Section (2.6) why such an approach may involve sampling problems when attempting to calculate the field directly from the plane wave spectrum.

3. The direct integration of the space domain measured data at the plane of measurement. The limitations encountered with this approach will be specified here.

4. The use the horn cluster aperture field distribution, evaluated through measurements, to describe the external field. This approach has shown good results and is detailed in this section.

1. It was thought, in the early stages of dealing with this horn cluster, that each individual horn might be considered as an isolated horn with a fundamental cosine aperture distribution[41]. It was assumed accordingly, the horn cluster aperture field could be replaced by the contribution of each individual horn depending on its location, dimensions and excitation level. The shape of that contribution would be determined from the horn's dimensions and structure, but the relative excitation level is the unknown quantity. The individual excitation level of each horn must be determined to obtain the model for the cluster. The following procedure was followed for that purpose.

The field quantities for each horn were described in the spectral domain by inverse Fourier transforming a normalized space domain field of the assumed aperture distribution. The horn cluster spectral domain field is the sum of the contributions from each individual horn. The measured field is already available in the spectral domain. Ideally, under the above stated assumption, the spectral domain field calculated from the contribution of separate horns, given the proper excitation level, must equal the measured spectral domain field. The following over-determined system of linear equations was accordingly constructed.

$$A\ e = m$$

where: A is an over-determined matrix with each element a_{ij} being the contribution of the horn j with unit excitation to the spectral domain field component i, e is the unknown array of each individual horn excitation, and m is an array containing the spectral domain field components. This system has no exact solution when m is substituted for by the measured spectral domain field m. An approximate value of e can be found by minimizing the norm of a residual array r, defined as:

$$r = A\ e - m$$

where: e is the approximation of e.

The QR decomposition[60] was used to solve for e in the above equation by minimizing the $L2$ norm of r. The values of the resulting horn excitations were inspected together with the values of the residual array element r. The failure of the assumption of treating the horn cluster as individual horns was indicated by the fact that the values of a significant number of the residual array elements were smaller, but of the same order of magnitude as the measured field spectral components. This conclusion will be asserted later when the horn cluster aperture field distributions calculated from the measured field are inspected. The above effort, even though it did not yield a practical result of providing a simple model of the cluster with a small number of parameters, indicates the significant effect of mutual interaction between the adjacent horns, and the need of further study of the interaction mechanism to improve the design performance prediction.

The spectral domain field data is used in evaluating the space domain immediate electric field, or the equivalent magnetic currents, at the horn cluster aperture. This is done in a way similar to Section (4.2), by transforming the plane wave spectrum back to the aperture plane, and Fourier transforming, to obtain the space domain equivalent currents. Figure (4.23) shows the resulting electric field at the aperture plane for both polarizations. The location of the main polarized electric field peaks and the geometrical centre of each individual horn are indicated on this figure, which shows clearly that they do not coincide. This would not be the case if an individual horn aperture field structure were not changed due to the interaction of the adjacent horns. This explains the failure of modeling the horn cluster as individual co-planar horns.

2. The application of spectral domain representation of the field has proved useful in evaluating the field at the radiator aperture, or alternatively, the equivalent radiating magnetic currents for this case. The evaluation of the near-field *directly* from the spectral domain representation, however, proved unsuccessful. The spectral domain measured electric field is transformed forward to 80 cm, from the horn cluster aperture plane, and the space domain field is evaluated by Fourier transforming these spectral component. The resulting field map is shown in Figure (4.24), which shows that the evaluated field is extremely noisy. This is attributed to the oscillatory nature of the Fourier transform kernel, which leads to the under-sampling problem described in Section (2.6). This problem did not arise when calculating the aperture fields of Figure (4.23) evidently, for the reasons described in the same section.

3. The field exterior to the plane of measurement, away from the radiator, could be evaluated using Huygens-Fresnel principle. This can be implemented by replacing the space domain measured electric field tangential to the plane of measurement by equivalent magnetic current distribution[7], and evaluating the contribution of this distribution at any point using Equation (2.1) or (2.2). The problem with this approach is

that when the field value at a point is calculated an integration of the whole plane of measurement is required, e.g around 10,000 points for the measurement of Figure (4 22), which makes this approach inefficient The other problem, as mentioned in sub-section (1 1.1), is that the field extraction from the measurement probe data is possible in the spectral domain only, unless certain assumptions are made about the measured field and the probe, as detailed in Section (3 1) This means that the extracted field is already available in the spectral domain The direct integration of the measured field will also exclude the error reduction advantage of the spectral and space domain truncations of the equivalent radiating currents, as can be concluded from sub-section (2 7 2)

4 Finally, from the above discussion, it is concluded that integration over the space domain might be performed better at the radiator aperture plane using equivalent currents which are calculated from the measured field In this case, the field distribution is *localized* on and around the aperture, and a fewer number of points need to be integrated For the case under consideration, only 465 integration points were needed to evaluate the field at any point exterior to the aperture plane This method has proved to be effective, and provided excellent resemblance to the measured field values in the near-field region This is demonstrated by Figure (4 25), where the electric field calculated at 80 cm. away from the horn cluster aperture plane is compared to the measured one The electric field in this figure was normalized to zero dB at point x=y=0

In addition to the cross-sectional plots at a distance d from the radiator, it is possible to compute the field at any specified geometry using the equivalent current model, such as at a plane containing the boresight axis of the radiator Thus, in Figure (4 26) are shown the main polarization (x-component, amplitude and phase contours) of the electric field over a y-z plane calculated from the truncated equivalent radiating magnetic currents, and compared with directly measured data The electric or magnetic fields can be similarly evaluated at any point in the space $z>0$ The only exception is the reactive region of the exterior field (fractional wavelength values of z), where the contribution of the evanescent field is significant and observable, because of the exclusion of the evanescent modes in the equivalent currents calculations

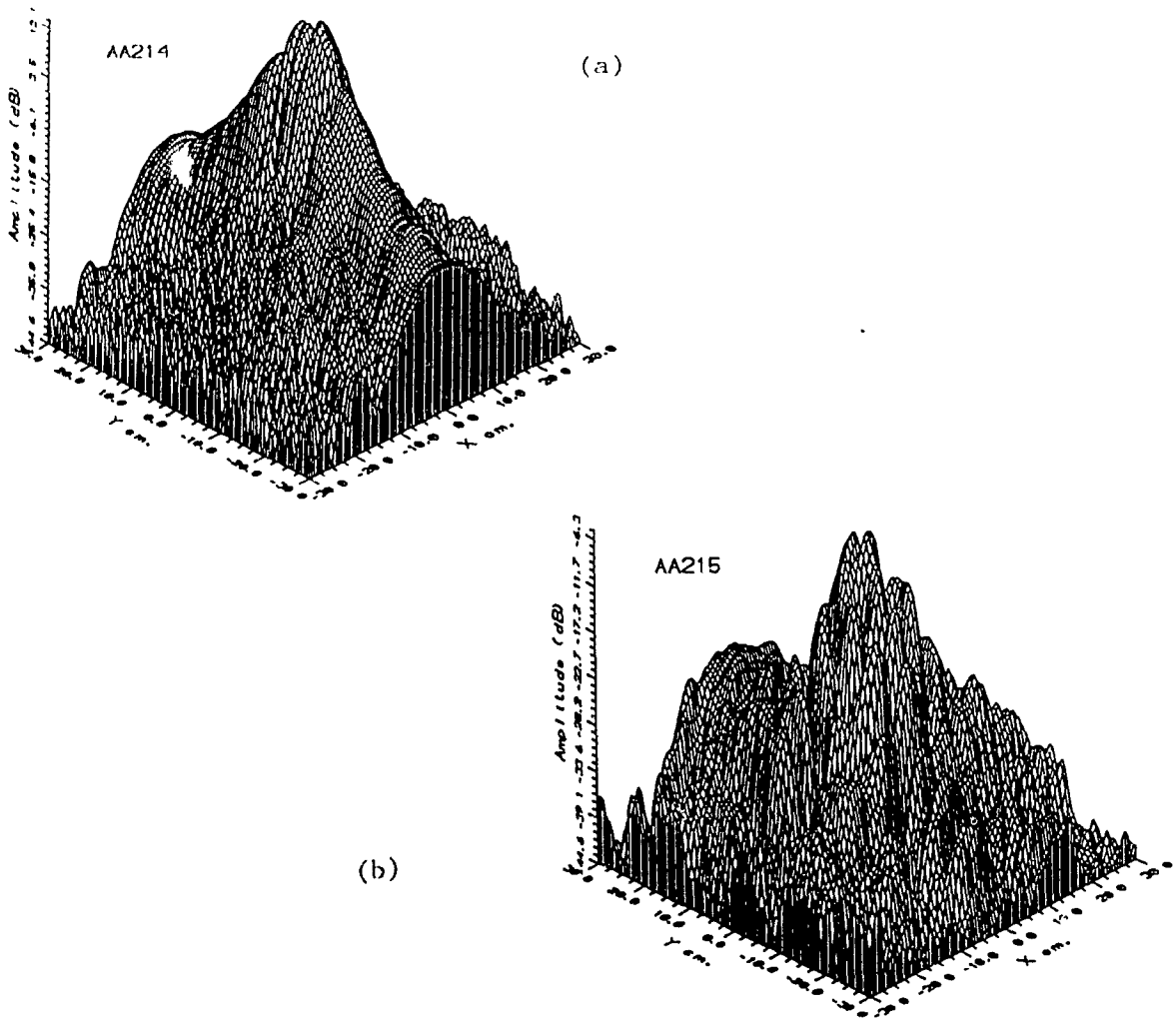

Figure (4.22): Planar near-field measurement data at a distance between horn cluster aperture and measurement planes of d=5.0 cm $\approx 2\lambda$ at 11.6 GHz. Dimensions of the plane of measurement are 60 cm.x 60 cm., and the sample spacing is 0.6 cm. Dipole probe #2, Appendix (B), is used in these measurement and the output voltage amplitude of the probe is shown here in dB scale. Phase data is also available from these measurements.

a) Dipole probe oriented along the x-axis (main polarization measurement).

b) Dipole probe oriented along the y-axis (cross polarization measurement).

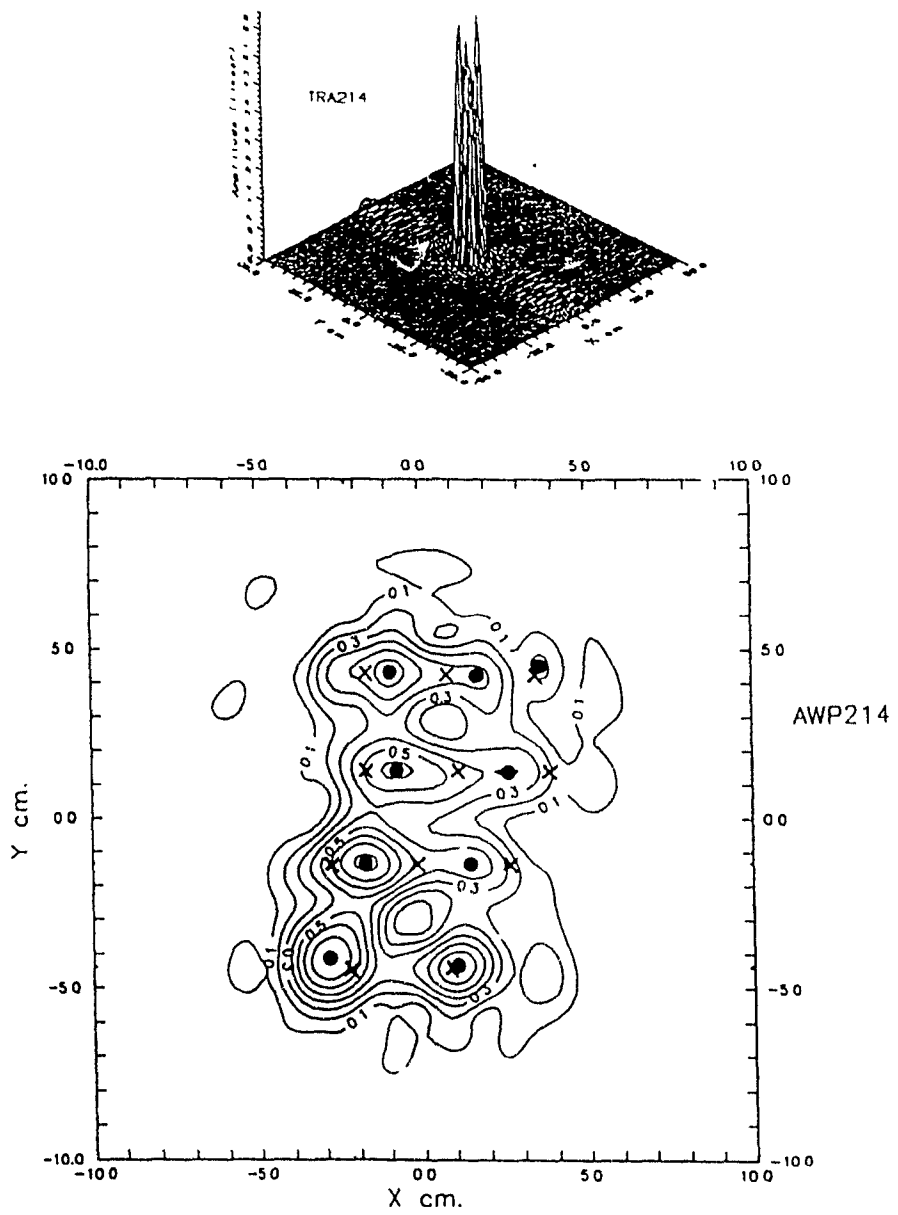

Figure (4.23-a): Relative linear amplitude of the main polarized aperture electric field distribution (x-component), or the equivalent radiating magnetic current distribution (y-component) at the aperture plane. These currents were calculated from the amplitude data of Figure (4.22) and the corresponding phase data. The contour map has maximum contour level of 0.8 and contour interval of 0.1. In the same map, the locations of the amplitude peaks are indicated by darkened circles (●), and the geometrical centre of each individual horn is indicated by a cross (X).

(continued next page)

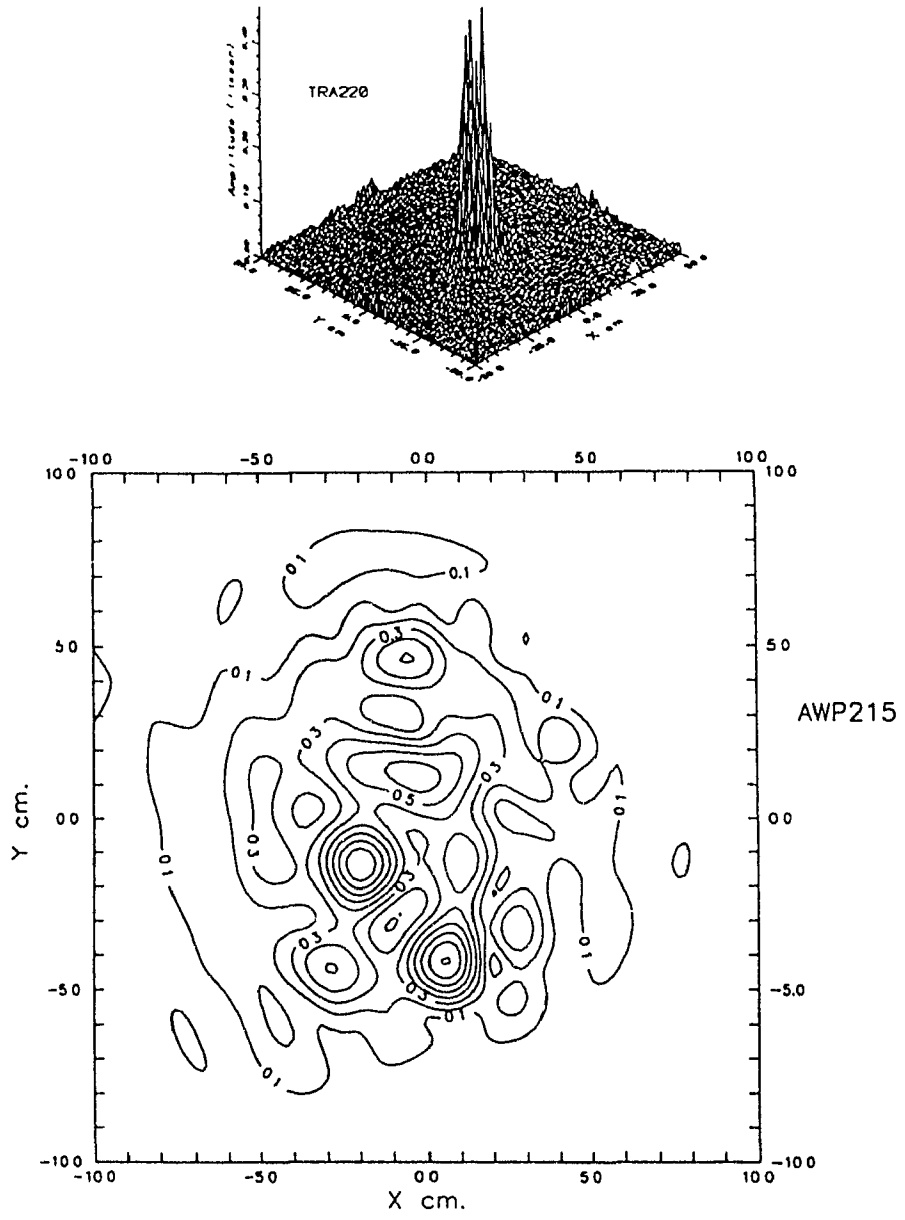

Figure (4.23-b): Similar to Figure (4.23-a), but for the cross polarized aperture field or equivalent magnetic current distribution. The spectral domain was truncated in calculating both parts of this figure to include only the radiating modes ($k_{tmax} = k_o$). The surface plots demonstrate clearly the localized nature of the fields around the physical aperture.

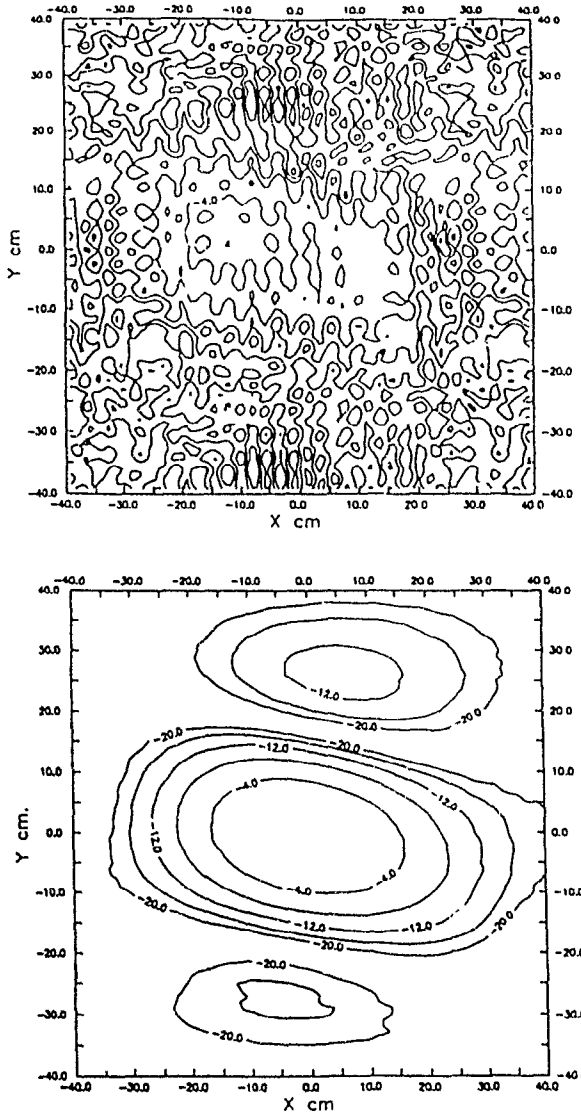

Figure (4.24): Demonstration of the under-sampling problem encountered when calculating the exterior field directly from the spectral domain

a) Main polarized electric field distribution calculated by transforming the spectral domain components into a plane z=80 cm and then, Fourier transforming into the space domain. The spectral domain under-sampling is affecting an extremely noisy field distribution (smoothing of the contour map was necessary in this case)

b) The same field distribution measured at the same plane using dipole probe #2, Appendix (B) oriented along the x-axis This distance ($d \approx 31\lambda$), and the small size of the probe, justified assuming that the probe output voltage is proportional to the main polarized electric field component.

Maximum contour is 0 dB and the contour interval is 4 dB in both maps.

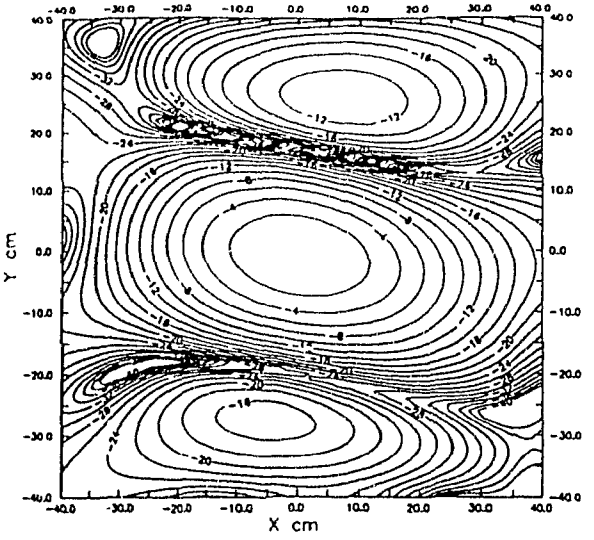

NFORA214 (a) Calculated

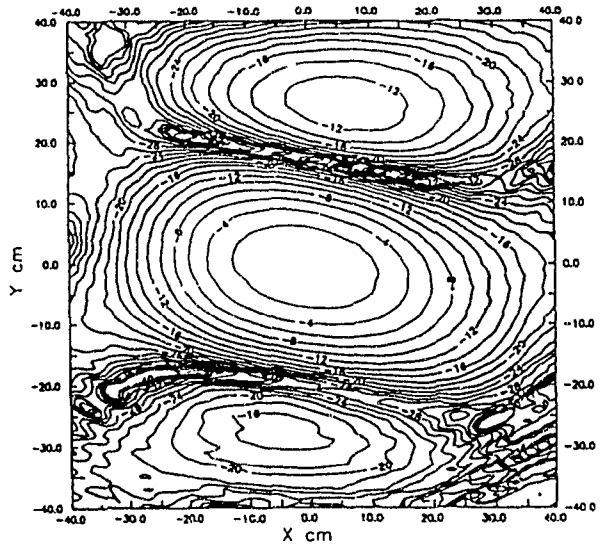

NAA213/2 (b) Measured

Figure (4.25): Comparison between the exterior electric field distribution calculated from the aperture equivalent radiating magnetic current and the directly measured one:

a) Main polarized normalized electric field at a plane z=80 cm., calculated from the equivalent currents of Figure (4.23-a) and the corresponding phase data. The equivalent current plane was truncated to within -7 cm. $<x<$ 7 cm. and -15 cm $<y<$ 15 cm.

b) The normalized electric field distribution measured at the same plane using dipole probe #2, Appendix (B) oriented along the x-axis.

Both maps have maximum contour levels of 0 dB and contour interval of 2 dB. The peaks in the two maps are co-located within 1 cm^2 and the amplitude differences between the calculated and measured values are 0.19 dB and 0.38 dB for the upper and lower peaks respectively.

(continued next page)

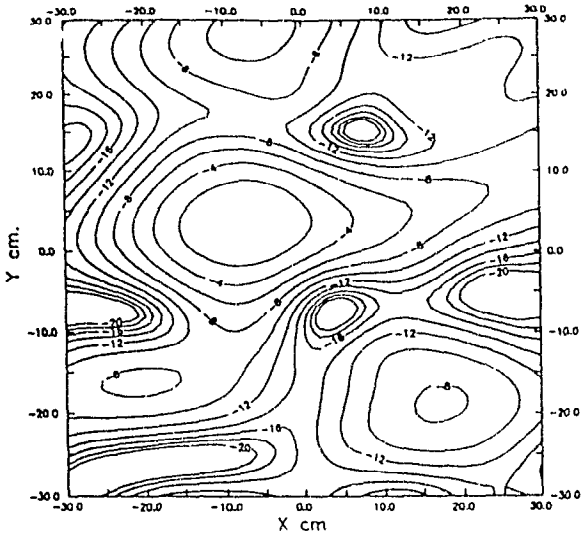

(c) Calculated

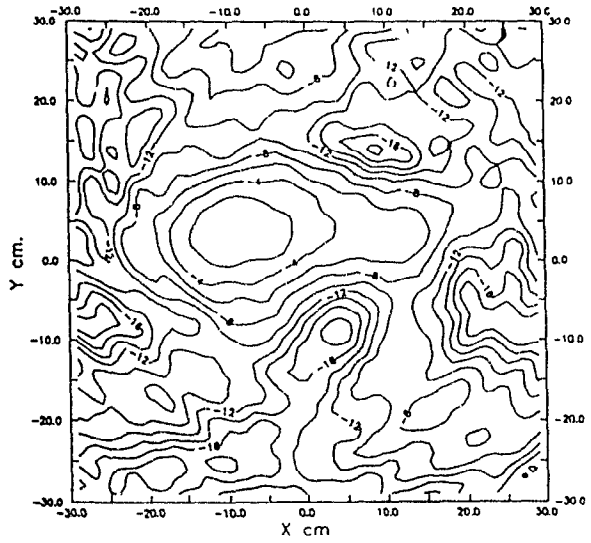

(d) Measured (with smoothing)

Figure (4.25):

c) Cross polarized normalized electric field at a plane z=60 cm , calculated from the equivalent currents of Figure (4.23-b) and the corresponding phase data The equivalent current plane was truncated to within -7 cm. $<x<$ 7 cm. and -15 cm. $<y<$ 15 cm

d) The normalized electric field distribution measured at the same plane using dipole probe #2, Appendix (B) oriented along the y-axis. This map had to be smoothed because of the noisy nature of the original one

Both maps have maximum contour levels of 0 dB and contour interval of 2 dB. A quantitative comparison was inconceivable because of the noisy nature of the directly measured cross polarized electric field

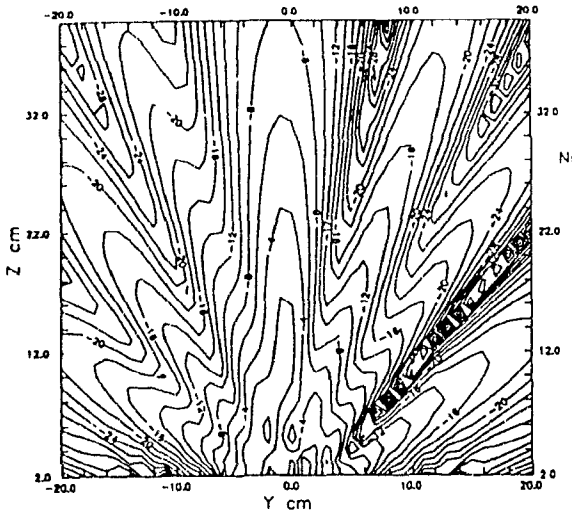

(a) Calculated

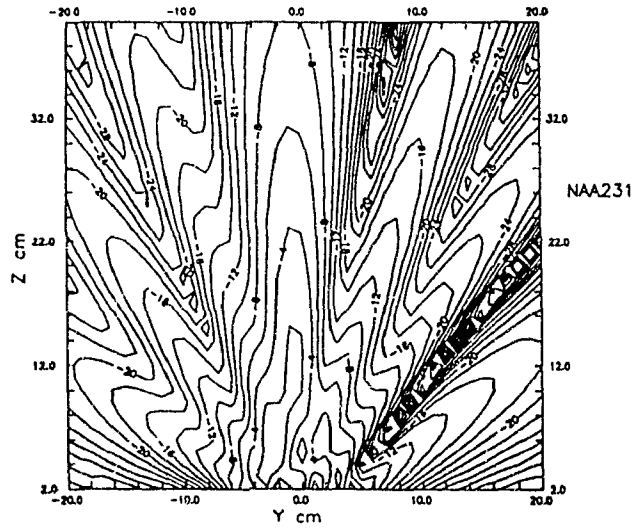

(b) Measured

Figure (4.26): Comparison between the calculated and measured main polarized electric field distribution on y-z plane (x=0).

a) Normalized electric field amplitude calculated from the equivalent currents of Figure (4.23-a) and the corresponding phase data. The equivalent current plane was truncated to within -7 cm $< x <$ 7 cm. and -15 cm. $< y <$ 15 cm.

b) Normalized electric field distribution measured at the same plane using dipole probe #2, Appendix (B) oriented along the x-axis.

Both maps have maximum contour levels of 0 dB and contour interval of 2 dB.

(continued next page)

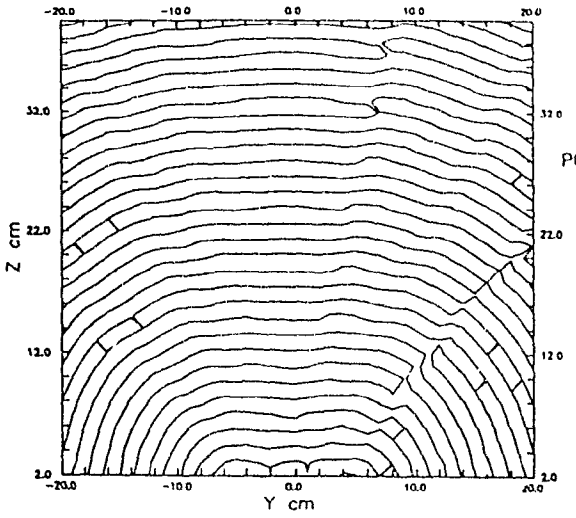

PORP230 (c) Calculated

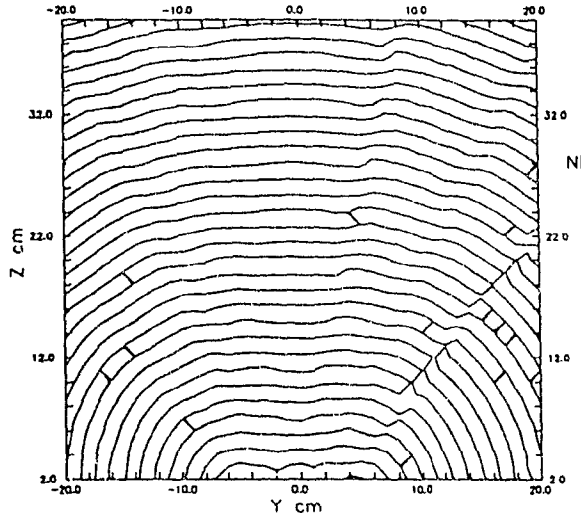

NPA231 (d) Measured

Figure (4.26).

c) Calculated electric field phase map associated with the amplitude map of part a of this figure.

d) Measured electric field phase map associated with the amplitude map of part b of this figure.

Both maps have 180° contour interval.

4.3.3. Comments:

The calculated results in Figures (4.25) and (4.26) have shown good agreement in locating and evaluating the peaks of the electric field, between the directly measured electric field, and that calculated from the measurement based equivalent magnetic currents The latter approach, however, shows superior performance in defining the field values in regions of low field level and close to the nulls Two reasons can be given to explain this superiority

1 The equivalent currents are calculated from measurements on a plane close to the radiator ($d \approx 2\lambda$) This implies that the field strength is higher at this plane, compared to that of the 80 cm ($\approx 31\lambda$) plane, where the direct measurements are performed. The measurement errors, discussed in Section (2 7) are not, in general, dependent on the location of the plane of measurement, which results in operating the measuring instruments at higher signal-to-noise ratio at the (2λ) plane This is demonstrated by inspecting the relative values of the measured probe voltages. The relative peak measured voltage is 14.89 dB at the (2λ) plane, while it is 1 07 dB at the (31λ) plane for the main polarization measurements of Figures (4.22-a) and (4 25-b) respectively.

2. The more important reason is the error filtering resulting from the spectral and space domain truncations associated with the utilization of the equivalent currents model. The equivalent currents shown in Figure (4.23) are calculated from measurement on a plane of 60 cmx60 cm. dimensions, and the sample spacing of 0 6 cm., at an operating frequency of 11 6 GHz , which corresponds to intrinsic wave number, k_o, of 2.43 rad/cm The spectral domain is truncated to include only the propagating modes, ($k_x^2 + k_y^2 \le k_o^2$), and the equivalent currents on the horn cluster aperture were truncated to within a rectangular plane of 14 cm.x30 cm x and y dimensions, respectively. These values substituted into Equation (2.27) give an estimated 17 dB random error reduction, and 9.33 dB spectral error reduction. As detailed in sub-section (2 7.2), the error power reduction is the ratio of error power normalized to the original radiator power in the equivalent radiator model, to the error power in the measured plane wave spectrum normalized to the original spectral domain field of the radiator. The peak error reduction in the spectral domain component $k_x, k_y = 0$, is estimated from the discussion associated with Equation (2.28) as 9 33 dB

The capability of having a reliable horn cluster model, using the equivalent aperture magnetic current distribution, enables the evaluation of the exterior electric or magnetic fields using equations (2.1) or (2.2) respectively This capability enables calculating the field incident on any assumed reflector surface to evaluate the combined antenna system performance, using a measurement based feed model.

4.4. Concluding Remarks:

The determination and use of the equivalent currents as a model of non-directive radiators was demonstrated in this chapter. The approach employed in dealing with the three cases discussed is quite similar, and can be summarized as extracting the field values in the spectral domain from the measurement probe output voltage, mapping the current distribution at the radiator plane, and finally evaluating the field exterior to that radiator using the mapped currents (amplitude and phase) as the radiating sources. Each case, however, had different objectives, and the results and conclusions drawn are particular to each.

In dealing with the microstrip edge, the objective was to study the immediate field structure around the edge and the far-field behavior. Examining the results leads to the conclusion that for the purpose of the external field evaluation, the edge model as a line of magnetic current along the edge is a good approximation of a single edge.

The second case, dealing with microstrip patch radiator, has lead to two conclusions: First, that the use of the evanescent modes can be useful in mapping the current distribution. These modes are usually accounted for in the literature, but the measurement of their physical existence and their use have not been reported previously. The second conclusion is that it was possible to model this radiator through the measurement of the local field around the patch, while minimizing contributions from scattering and secondary radiation from the supporting structure of such a radiator, which is usually large relative to the radiator size.

The third case, which studied the horn cluster, has demonstrated two issues. First, is that the effect of mutual interaction between the individual horns, which this radiator is made up of, significantly changes the radiation behavior of each horn. This was evident from the fact that the mapped equivalent current distribution peaks at the aperture plane did not coincide with the geometrical centres of these horns. This is a case which demonstrates the need to carry out exploratory measurement to achieve understanding of the behavior of a complete radiator, on which a theoretical model can then be based. The second issue is the ability to model this radiator, using the equivalent radiating magnetic currents at the aperture. This provides reasonable quantitative accuracy and the advantage of filtering out a significant amount of measurement errors.

The mechanical structure of these radiators shows that the planar near-field scanning is, mechanically, the most convenient compared to cylindrical and spherical scanning schemes. Literature published so far[3] indicates that the planar near-field measurement is restricted to dealing with directive antennas. This conclusion was based on the use of the spectral domain representation of the radiated field. The previous two chapters of

this thesis, however, have shown how to evaluate and use the equivalent currents model of a general radiator, from planar near-field measurements This chapter has shown that this model has successfully facilitated the use of planar near-field scanning in dealing with non-directive radiators

CHAPTER FIVE

CONCLUSIONS

This chapter forms a review of the thesis, followed by a discussion of the three main issues dealt with in this work, namely: the immediate field or *equivalent radiator current mapping*, *radiator modeling* and the problem of *field extraction* from the measurement probe.

The results of this research are evaluated here, and the claims of contributions of this thesis, which are listed in Section (1.5), are re-iterated. At the end, proposals are made for new areas of investigation arising from these contributions.

5.1. Review:

The review of the state of the art, in Chapter One, demonstrates that much of the work in near-field measurements previously dealt with large, highly directive antennas. It was also stated that small electromagnetic radiators usually have relatively large supporting structures. This indicated the geometrical advantages of the planar near-field scanning scheme in dealing with such radiators. The necessity for detailed understanding of the measurement probe behavior was also emphasized. It was then shown that the theoretical work in this thesis deals with an operator equation of the form $Ix = b$, which can *either* describe a forward *or* an inverse problem. This theoretical approach was used complementing the interpretation of the raw measured data for characterizing the radiation behavior of the radiator.

In Chapter Two, the theoretical principles, upon which the characterization and modeling of the radiator are based, are discussed. A conclusion is reached, which is to represent the radiator *either* by electric *or* magnetic equivalent currents distribution, with the choice depending on the nature of the radiator under consideration. The relationship between the equivalent currents and the field quantities in the plane of measurement is established in the spectral domain. This is followed by an estimation of the validity range, in the spectral domain, of these relations. These ranges were estimated in consideration of the sensitivity to measurement errors. It was found that the resolution depends on the type of the measured field and the type of the currents representing the radiator.

The design of the planar measurements is also discussed. It is concluded that the choice of measurement parameters must be based on the experience gained from preliminary exploratory probing of the field around the radiator, and on the objectives of the measurement. It is shown that a direct evaluation of the near-field quantities from the plane wave spectrum leads to computational difficulties. It is suggested, therefore, that the near-field should be calculated from the integration of the contribution of the equivalent currents at the radiator aperture instead. This is followed by discussing the sources of errors in the planar measurement of non-directive radiators. It is found that the utilization of the equivalent currents model of the radiator will significantly reduce the effect of the measurement errors. The amount of this reduction in peak and r.m.s errors, is estimated.

Chapter Three deals with the influence of the measuring probe on the measurement, and develops the formulation for the extraction of the field values from the measured probe output voltage. In addition to the general case, it is possible to distinguish two special cases for which this extraction can be simplified. The general case, under planar near-field measurement environment, is the principal subject of the chapter. The probes are classified into two types: wire and aperture. Relationships between their output and the measured electric and magnetic field are established. These relations are based on proportionality constants developed here, namely the *Vector Field Extraction Coefficients*. The theoretical evaluation of these coefficients, for both types of probes, is elaborated on, with specific examples. An outline for an experimental procedure for determining these coefficients is also proposed, and has been applied experimentally to the case of a $\lambda/2$ dipole. The chapter includes also a comparison between the described field extraction procedure and the commonly called *Probe Correction techniques* described in existing literature.

Chapter Four deals with experimental work based on the theory presented in the previous chapters. It contains three sections, each dealing with a specific type of radiator, namely, an approximation of an *infinite microstrip edge*, a *microstrip rectangular patch* and a *horn cluster with co-planar apertures*. In each case, preliminary measurements are described to test certain assumptions and/or to gain an initial idea about the radiator field structure. These were followed by planar measurements, from which the equivalent radiating sources were *mapped*. These mapped sources are used to draw conclusions specific to each radiator, which are useful for characterizing its radiation behavior. In addition, their use as a model for external field calculations is demonstrated. In essence, Chapter Four shows that the theoretical work, that the previous chapters had dealt with, can be applied to the three cases considered. In all cases the objectives were to *characterize* and *model* the radiators under test.

5.2. Evaluation of the Results and Conclusions:

In what follows, an evaluation of the contribution of this investigation is carried out and conclusions are drawn accordingly. These are classified according to either of the two major objectives of this thesis, which are the *Characterization* and the *Modeling* of non-directive radiators. The problem of *Field Extraction* from the probe measured voltage, also dealt with at length in this thesis, is also discussed here.

5.2.1. Radiator Characterization:

The *characterization* of a radiator, here, is the qualitative definition of the radiation mechanism of the radiator. This concept crystallized in this thesis into the idea of high resolution space domain mapping of the immediate field, or of the equivalent currents. Some conclusions about the radiation mechanism can be drawn from the resulting maps, and can be useful for diagnostic and theoretical purposes. The following conclusions can be identified:

1. The major part of Chapter Two dealt with the issue of radiator characterization, where the choice of the proper field components to measure for high resolution equivalent current mapping is established. After selecting the field to be measured, it was concluded, through taking the effect of noise into consideration, that the attainable resolution depends on the distance between the plane of measurement and the radiator aperture plane, as shown in Figure (2.5). It can be concluded from observing this graph that the evanescent modes, which add the high resolution details to the equivalent current map, can only be used if the distance between the measurement and radiator aperture planes is of the order of 0.1λ or less.

2. The close aperture to measurement plane distance may impair the accuracy of the mapping, because of the possibility of strong mutual interaction between the measuring probe and internal field of the radiator. The field maps, nevertheless, can be indicative of the radiation mechanism of the radiator. Referring to Figure (4.5), the experimental results show that the peak of the mapped current coincides with the location of the microstrip edge. More important demonstrations are the ones shown in Figures (4.16) and (4.17), which demonstrate that the employment of the evanescent modes reveals further details of the immediate field structure of the microstrip patch under consideration. The mapping of the horn cluster aperture electric field shown in Figure (4.23-a) was essential in concluding that the mutual interaction between the horns has changed the aperture field structure of the individual horns. This is obvious from noting that the field peaks

do not coincide with the geometrical centres of the horn's apertures. These applications of the planar near-field measurements were useful for *characterizing* the radiatic ' mechanism of non-directive radiators.

3. The limited resolution of the methods proposed in Chapter Two can be increased by employing assumptions about the radiating sources as was mentioned in Section (2.2). These may be used to formulate a well-posed relation between the measured field and a high resolution equivalent current (often called Regularization of the problem). For example, the electric field over and tangential to the patch can be set to zero, and this information can produce higher resolution of the mapped currents. The difference between such an approach and that employed by this work, is that the mapped equivalent currents, such as those shown in Figures (4.5), (4.17) and (4.25), are modified only by smoothing. The results from such regularized formulation may give higher resolution of the currents, but can depart qualitatively from the reality. It is suggested here that a smoothed equivalent currents map can be produced, using the techniques described, and can be used to judge the validity of higher resolution maps In addition, the same smoothed map can be used to judge the validity of field measurements in close proximity of the probe to the radiator, such as the one shown in Figure (4.14).

5.2.2. Radiator Modeling:

Radiator *Modeling*, as one of the objectives of this work, involves quantitative definition of parameters from which the external field values can be calculated. The following conclusions are indicated about the approach employed by this thesis:

1. The model chosen as a source of the external field is the equivalent current distribution at the radiator aperture. The experiment design and the calculation of the equivalent currents is similar to that used in equivalent current mapping. The only difference is that the evanescent modes are not utilized in these calculations, for two reasons. first, the plane of measurement should not be located close to the radiator, for which the measurement of the evanescent modes is unreliable as can be observed by the graphs in Figure (2.4) The second reason is that the evanescent modes are necessary only for the mapping of the immediate field, and they are *invisible* in the "near-field" or the far-field regions defined in Section (1.4). Their calculation is, therefore, unnecessary when the two latter regions are of interest.

2. It was concluded in Section (2.6) that the direct evaluation of the "near-field" from the measurement results, in the spectral domain, is numerically impractical because of the oscillatory nature of the integrand involved. This fact was demonstrated by Figure (4.24) for a practical case. The direct integration of space domain measured data to evaluate the "near-field" is, also not feasible. As was explained in sub-section (4.3.2),

this approach does not permit the deconvolution of the probe response, which is performed in the spectral domain, and will involve integration of an excessively large number of data points to evaluate a single near-field point, as was demonstrated in the same sub-section. This suggests the equivalent radiating currents to be the practical model from which the "near-field" can be calculated for the radiators considered in this work.

3. It has been suggested[13,14] that an equivalent current model can be employed as follows: The field can be measured at a set of exterior points using a probe with a known model, and the equivalent currents can be presumed to be located on and around the physical aperture of the radiator. Consequently a set of linear relations between the output voltages of the probe and the equivalent currents expanded into sub-domain basis functions, can be established From these relations the equivalent currents can be evaluated using the measured probe voltages The difference between that approach and the one adopted by this thesis, is that the use of planar measurement will guarantee gathering the full information about the radiating field of the radiator, with a specified sampling rate as detailed in Section (2.5), which is not the case for the other approach for an unspecified pattern of measurement points. The other (and more significant) difference is that the method proposed here includes the mapping of the field at the radiator plane without a pre-assumption about the field structure, and thereafter, the current is truncated for improved error reduction and numerical efficiency. In the other approach, the measurement errors and the original field will contribute to the evaluated equivalent currents on an equal basis. This might abolish the error reduction feature of the equivalent current model In addition, there is no guarantee that the field will be localized around the aperture Aperture field maps like the ones of Figures (4 18) and (4.23) can indicate to what extent the equivalent current plane can be truncated.

4. The application of planar near field measurement was limited to highly directive antennas in the past[3]. The significance of the truncation error and the distortion of the measurement spectral domain data has made the calculation of the external field of non-directive antennas impractical if they were carried out using such data, as was shown in sub-section (2.7.1). On the other hand, planar near field scanning proved geometrically mechanically convenient for measuring small radiators (usually non-directive) with large supporting structure and avoiding secondary radiation from other sources . This fact is demonstrated by Figure (4 9) and by observing the geometrical shapes of the radiators considered in this thesis The calculation of the external fields using the truncated equivalent current model has reduced the effect of this error on such a calculation. The total error power and the peak error magnitude are reduced by this truncation as was established in sub-section (2.7.2). The calculations, for

which the results are outlined in sub-section (4.3.3) for the horn cluster radiator, had estimated that both spectral peak error and the spectral error power were reduced by about 9 dB, and the random error power was reduced by 17 dB.

The mechanism of error reduction by truncating the aperture equivalent current is similar to the Time Gating error reduction technique[61] used in antenna measurements. In this technique, the output voltage of a probe is measured at certain point for a certain operating frequency range, and this is transformed into the time domain in which the signal originating from the antenna or scatterer under test is localized within a finite time window, whereas the contribution to the probe output from other sources is distributed all over the time domain. The error reduction is achieved, in this case, by truncating the time domain to within a window where the contribution from the radiation source under test is dominant. The same logic is used here, except that the truncation is in the space domain, and frequency scanning is replaced by space scanning.

In the author's opinion, this feature of the equivalent current model of the radiator is the most useful one, because it combines the practicality and the geometrical convenience of the planar near-field scanning with the ability to deal with non-directive radiators. The experimental results shown in Figures (4.19), (4.20), (4.25) and (4.26) demonstrate the success of the equivalent current model of the radiator (derived from planar measurements) for calculating the field quantities at non-assymptotic distances.

5. There might be reasons to suggest that, although the equivalent current model has given accurate exterior field calculations for wide angular range off boresight, the model might not be reliable in producing the accurate field quantities for extreme off boresight angles (close to 90°) A simple explanation is that the planar scanning, as dictated by its geometry, does not collect information about the radiator field for these angles. A more rigorous explanation, as was stated in sub-section (2.7.1) in the discussion associated with Equation (2.23), is that the spectral domain electric field might be singular for $k_z = 0$, if the actual radiating source on the aperture plane has electric current components. The truncation of the equivalent currents plane, in essence, resulted in reduced coupling between this singularity and the rest of the spectral domain components of the field. The singularity, however, cannot be dealt with numerically, and the field calculations for the region where the contribution of this singularity is dominant might not be accurate. In the far-field, the angles close to 90° off boresight correspond to $k_z = 0$, where the singularity in the actual field might exist. This limitation was not noticable in the cases studied here, when comparing the field calculated from the equivalent current model and that measured directly as shown in figures (4.20) and (4.26), but might be significant for other radiators.

5.2.3. Field Extraction:

The extraction of field quantities from the output voltage of the scanning probe is one of the key issues of this work. Furthermore, the measurement of non-directive radiators requires the knowledge of the scanning probe behavior over a wide range in the spatial spectral domain. It is important to establish probe selection and design criteria, and to model the probe properly to examine the extent to which the field information is transparent through the probe output.

The methodology of field extraction used in this thesis uses the same principles as most of the commonly known *probe correction* procedures, since it extracts the field from the spectral domain measured voltage. However, in the formulation here the *Vector Field Extraction Coefficients* are introduced. The main feature of these is that they allow a link between the probe performance under planar measurements and its electromagnetic behavior. Other aspects are detailed in the following:

1. The measured voltage data is considered as a vector, which allows examining the probe performance with taking the measurements of the two polarizations into account. This facilitates defining measurement validity limits, using Equation (3.11), as shown in Figure (3.6) for the cases of a half wavelength dipole and an open ended dielectric loaded waveguide.

2. The *Vector Field Extraction Coefficients* exist for the three field components as implied by Equation (3.9), and the coefficients for each component are shown in equations (3.12) and (3.13) for a wire and an aperture probe, respectively. It was stated in the discussion following these equations that by using the duality of Maxwell's equations, the same expressions for the coefficients, interchanged between the wire and aperture probes, can be used for extraction of the magnetic field components as demonstrated by Figure (3.4). This unified approach of dealing with both types of fields is a very important result of this work, since it enables the selection of the proper type of probe for high resolution measurement of the field components. The form and existence of singular behavior in the expressions of the Vector Field Extraction coefficients of equations (3.12) and (3.13), implies that the use of wire and aperture probes will result in high resolution measurement of the components tangential to the plane of measurement of the electric and magnetic fields respectively. This result led to a selection criterion for the probe type for high resolution immediate field or equivalent current mapping as stated in Section (3.6).

3. The probe model used in this thesis assumes that the electric current or the aperture electric field distributions are known at the probe plane. This thesis, however, does not enter into the problematics of the theoretical determination of these distributions. In Section (3.4), however, an experimental procedure was outlined and applied to the

modeling of a dipole probe. The methods used in the equivalent current mapping as described in Chapter Two and applied in Chapter Four can also be used for the experimental determination of the electric current or the aperture electric field distribution of a probe with an unknown model (radiator under test) using a probe with a known model.

5.3. Future Work:

This research has produced results which, in addition to their own usefulness, can also serve as basis for new investigations. The following enumerates some potentially promising directions which might be pursued.

1. Study of measurement simulation. A quantitative idea about the absolute values of the measurement errors are difficult to obtain from the experimental work, because of the difficulty in measuring the input errors to the measured data. This suggests the employment of simulated radiators and, consequently, simulated measured data, with controllable input errors. The simulation would be more accurate when considering the experience gained by the experimental work of this thesis, where some of the phenomena observed can be included and considered in the simulation. The results of such simulation are useful for exploring different kinds of radiator and supporting structure schemes, and will enable the generalization of the conclusions of this work.

2. Study of numerical deconvolution of truncation error: It was demonstrated by Equation (2.23) that the truncation of the plane of measurement is in effect a convolution of the spectral domain field, with a spectral domain window. The same equation indicates that by a convenient deconvolution process, the spectral domain field information can possibly be extracted from the measurement. This suggests that a planar measurement, over a smaller region than suggested by Section (2.5) can be used to evaluate the spectral domain field if a well-posed deconvolution process can be implemented. In addition, it was shown that the truncation error is caused by the coupling to the singularity of the original spectral domain field at $k_z = 0$. This coupling can be reduced by truncating the measured field using low side-lobes window functions, such as a two dimensional Hanning window. The use of such a window function will reduce coupling to the field singularity, but unfortunately, will locally smooth the spectral domain field because of the wide main-lobe in the spectral domain response of such window function.

3. Determination of a model with minimal amount of measured parameters. The truncated equivalent current distribution at the radiator plane was suggested here as a model from which, the exterior fields can be calculated. This model, in spite of its accuracy, may not be the one that minimizes the information required to represent the exterior field. An added efficiency of storage and calculations can be effected if a model can be suggested with a smaller number of parameters. One can not be specific at this stage, but it seems that a link between the measurement based model proposed here and a geometrical optics model of a radiator, if established, might be useful for that purpose. This would combine the accuracy of the equivalent current model and the simplicity of the calculation of the exterior field using a geometrical optics model

4. In depth study of the theoretical current distributions of probes. In the context of the field extraction from the measured voltage, it was stated that the probe was modeled by the current distribution on the probe aperture when radiating The evaluation of this distribution theoretically or numerically needs to be examined more thoroughly for that purpose. Other ideas proposed using the results of Chapter Three need to be examined, such as the use of two kinds of probes for a high resolution measurement of electric and magnetic fields (Section (3.3))

5. Application of the developed measurement techniques: Although, the main interest of this thesis was in establishing a measurement methodology, the experimental work on specific radiators in Chapter Four may have facilitated further study of these radiators, such as:

a. The technique of approximating an infinite edge used in Section (4.1) can be applied other kinds of radiators or scatterers with a two dimensional structure, such as slits, edges or long wires Similarly, the techniques of Section (4.2) can be applied to study the radiation from other planar structures such as printed boards and microstrip line discontinuities and junctions.

b. A field map similar to that shown in Figure (4.11) can be used to calculate the electric current distribution over the patch. This requires an accurate and high resolution measurement of the electric field normal to the patch (E_z in Figure (4.11)) which is the only component over the patch conducting surface. This requires the utilization of a smaller probe than the one used in obtaining the results shown in that figure. This, however, would be more practical if a larger microstrip patch (i.e. lower resonance frequency) is considered

c. An aperture field map similar to that shown in Figure (4.23) can be used to study the interraction mechanism between adjacent or close horns (or any other radiating elements). Such a study would complement previous research[62,63] that used volume field distribution measurements for that purpose.

d. Finally, as was stated at the end of sub-section (4.4.3), the measurement based model of the refelector antenna feed tested in Section (4.3) could be used to predict the performance of the whole antenna system. The validity of such a conclusion should be tested by comparing a predicted performance using the presented feed model combined with the reflector surface, and actual measurement on a complete antenna system. Such an effort would run parallel to work already proposed that uses direct measurement of the fields of the feed incident on a notional reflector surface[64].

APPENDIX (A)

EVALUATION OF THE VECTOR FIELD EXTRACTION COEFFICIENTS

The evaluation of the vector field extraction coefficients is detailed here. These coefficients are defined by equations (3.9) and (3.10), and the derivations here are conducted with reference to Figure (3.3) and the assumptions posed in Section (3.3).

The probe orientation is defined here as the direction of an arbitrary axis of the probe that lies within the plane of measurement. The quantities below are described in the spectral domain unless otherwise stated. The probes are considered here as radiating and receiving for which the superscripts a and b respectively are used to indicate the corresponding fields and currents.

A.1. Wire Probe:

Referring to Figure (3.3-a), with the probe initially oriented along the x direction, the wire probe is linked to the measuring instruments through a coaxial line with inner radius a and outer radius b. A uniform radial electric current sheet to be assumed injected into the transmission line such that:

$$\vec{J}_r^a(r) = \hat{r}\frac{1}{Z_t 2\pi r} \qquad (A-1)$$

This current is the circuit equivalent of applying a unit input voltage. Z_t is the probe input impedance at this location of the current sheet, and r is the radial distance from the line center. The resulting current distribution on the radiating elements of the probe can be expressed as:

$$\vec{J}_s^a(x,y) = \hat{x} f_x(x,y) + \hat{y} f_y(x,y)$$

which is assumed to be known from the electromagnetic analysis of the probe or by some reasonable approximation. Fourier transforming the above relation:

$$\vec{J}_s^a(k_x,k_y) = \hat{x} F_x(k_x,k_y) + \hat{y} F_y(k_x,k_y)$$

The tangential modal magnetic field can then be defined for $z<0$ using the boundary condition[7] $J_s = -2\hat{z} \times H$ as:

$$\vec{H}_t^a(k_x,k_y) = -\hat{x}F_y(k_x,k_y)/2 + \hat{y}F_x(k_x,k_y)/2 \qquad \ldots.(A-2)$$

Considering a single mode (k_x,k_y) incident electric field on a receiving probe, the incident field can be replaced by an equivalent magnetic current for $z>0$[7]:

$$\vec{M}^b(k_x,k_y) = 2\vec{E}^b(k_x,k_y)\times\hat{z} = 2\hat{x}F_y^b(k_x,k_y) - 2\hat{y}E_x^b(k_x,k_y) \qquad \ldots.(A-3)$$

The open circuit output voltage for this mode at the same point on the transmission line is $V_{ocx} = V_x(Z_l+Z_t)/Z_t$, which defines the radial electric field in the transmission line as:

$$F_r^b(r) = -f\frac{V_x(Z_l+Z_t)/Z_t}{\ln\left(\frac{b}{a}\right)r} \qquad \ldots.(A-4)$$

where Z_l is the load (measuring instrument) impedance at this point of the transmission line. Using the reciprocity theorem[7] to link the interchanged sources and fields:

$$\int\int_S (\vec{F}^a.\vec{J}^b - \vec{H}^a.\vec{M}^b).dS = \int\int_S (\vec{E}^b.\vec{J}^a - \vec{H}^b.\vec{M}^a).dS \qquad \ldots.(A-5)$$

Substituting for fields and currents:

$$-\int_{-\infty}^{\infty}\int_{\infty}^{\infty}\vec{H}_t^a e^{-j(k_x x+k_y y)}\,\vec{M}^b e^{-j(k_x x+k_y y)}dxdy = 2\pi\int_a^b \vec{J}_r^a(r).\vec{E}_r^b(r)rdr$$

Both sides can, then, be evaluated using equations(A-1), (A-2), (A-3) and (A-4), yielding:

$$V_s = -Z(F_xE_x + F_yE_y)\delta(k_x,k_y) \qquad \ldots.(A-6-a)$$

To evaluate the probe output voltage when oriented along the y-axis, axis transformation is utilized to obtain:

$$V_y = -Z(-F_y^* E_x + F_x^* E_y)\delta(k_x, k_y) \qquad \ldots (A-6-b)$$

where $Z = Z_t Z_t / (Z_t + Z_t)$ is set to 1 for normalization since it is independent of the mode variables, $F_x^*(k_x, k_y) = F_x(k_x, -k_y)$ and $F_y^*(k_x, k_y) = F_y(k_y, -k_x)$. The Dirac delta function is a consequence of integration and will be neglected, because it has no effect on the final results.

Since $\nabla . \vec{E} = 0$ around the probe (which is a source free region), then for an incident mode (k_x, k_y):

$$k_x . E_x + k_y . F_y + k_z . E_z = 0 \qquad \ldots (A-6-c)$$

from which E_z can be evaluated. Inverting the above relations, the vector field extraction coefficients for a wire probe, will be:

$$\vec{C}_x = \frac{1}{\Delta}(\hat{x} F_x^* - \hat{y} F_y) \qquad \ldots (A-7-a)$$

$$\vec{C}_y = \frac{1}{\Delta}(\hat{x} F_y^* + \hat{y} F_x) \qquad \ldots (A-7-b)$$

$$\vec{C}_z = \frac{1}{\Delta}\left(\hat{x} \frac{-k_x F_x^* - k_y F_y^*}{k_z} + \hat{y} \frac{k_x F_y - k_y F_x}{k_z} \right) \qquad \ldots (A-7-c)$$

where $\Delta = F_x F_x^* + F_y F_y^*$

A.2. Aperture probe:

In determining the vector field extraction coefficients for the aperture probe shown in Figure (3.3-b), the current density is injected as in Equation (A-1) to correspond to excitation by a unit input voltage. The resulting aperture field can be determined using numerical methods or approximations. By Fourier transformation the aperture field for the mode (k_x, k_y):

$$\vec{F} = \hat{x} F_x + \hat{y} F_y$$

To satisfy the radiation condition, the modal radiated electric field is described for $z<0$ as:

$$F^{m}(x,y,z) = F^{m}(k_x,k_y)e^{-j(k_x x + k_y y + k_z z)}$$

from which the modal tangential magnetic field can be determined using the source free Maxwell equations $\nabla \cdot \vec{F} = 0$ to find the third component of the aperture field, and $\nabla \times \vec{F} = -j\omega\mu\vec{H}$ to find the magnetic field. When the probe is receiving, similar treatment for the incident electric field and transmission line radial electric field is affected as in the case of the wire probe. After substituting the fields and currents into Equation (A-5), the normalized output voltages from the probe for the x and y probe orientations respectively, are:

$$V_x = \frac{(k_x^2+k_y^2)F_x + k_x k_y F_y}{k_z}E_x + \frac{(k_y^2+k_z^2)F_y + k_x k_y F_x}{k_z}E_y \qquad \ldots.(A-8-a)$$

$$V_y = -\frac{(k_x^2+k_z^2)F_y^* - k_x k_y F_x^*}{k_z}E_x + \frac{(k_y^2+k_z^2)F_x^* - k_x k_y F_y^*}{k_z}E_y \qquad \ldots.(A-8-b)$$

Adopting the same treatment that led to Equation (A-7), the vector field extraction coefficients for an aperture probe are:

$$\vec{C}_x = \frac{1}{k_o^2\Delta}\left(\hat{x}\frac{(k_y^2+k_z^2)F_x^* - k_x k_y F_y^*}{k_z} - \hat{y}\frac{(k_y^2+k_z^2)F_y + k_x k_y F_x}{k_z}\right) \qquad \ldots.(A-9-a)$$

$$\vec{C}_y = \frac{1}{k_o^2\Delta}\left(\hat{x}\frac{(k_x^2+k_z^2)F_y^* - k_x k_y F_x^*}{k_z} + \hat{y}\frac{(k_x^2+k_z^2)F_x + k_x k_y F_y}{k_z}\right) \qquad \ldots.(A-9-b)$$

$$\vec{C}_z = \frac{-1}{k_o^2\Lambda}(\hat{x}(k_x F_x^* + k_y F_y^*) + \hat{y}(k_y F_x - k_x F_y)) \qquad \ldots.(A-9-c)$$

APPENDIX (B)

DESCRIPTION OF THE MEASUREMENT PROBES

While many types of probes were experimented with throughout this work, only three types were used in the measurements. These probes are described in this appendix, with the specific considerations taken in dealing with them indicated.

B-1. Probe #1:

This probe is a dipole with an unbalanced coaxial feed shown in Figure (B-1) The balanced feeding of the two arms of the dipole is achieved through the use of a *balun* structure. This structure is implemented by fabricating two longitudinal slots of approximately quarter wavelength at the end of the semi-rigid coaxial feedline shell Both dipole arms are connected to the shell on the opposite sides of the slot, one arm being connected to the central conductor of the coaxial line The matching mechanism of this structure is detailed elsewhere[41] This probe was fabricated for previous work in near-field measurements, and was utilized at the early stage of the work described in this thesis

This probe was used in the experimental work described in Section (3.4), and its spectral domain electric current distribution is shown in Figure (3 9), for 11 65 GHz operating frequency. The unsymmetry in the probe current distribution is obvious from that figure. The experimentally evaluated current distribution is used in evaluating the far-field radiation patterns of Figure (4 12)

This probe is convenient for near-field measurement, especially if the measured current distribution of the probe is well established Reducing the length of the dipole arms to reveal more detailed field structure, however, may not be practical, because the open and relatively large matching structure may result in unpredictable model of the dipole in near-field measurement environment.

B-2. Probe #2:

The balanced dipole of Figure (B-2) is introduced as a short dipole, with simple feed. Each arm of the dipole is connected to a separate semi-rigid coaxial cable with a fixed electrical length. The signal from each dipole arm is combined using a 0 - 180° microwave power splitter/combiner (*Anaren* model (30058)), operating in the 8 0 to 12.4 GHz bandwidth. The sum port of this combiner is terminated with a matched load.

The simplicity of the feed structure facilitates the assumption of a simple model of the probe, and the utilization of a broad-band power combining device enables the use of this probe over a broad frequency range

The current distribution on the radiating dipole arms is approximated to be triangular for operating frequencies at which the total dipole length is equal or less than a quarter wavelength When the dipole aligned on the x-axis, with a length L, the electric current distribution is

$$I(x) = \hat{x}\left(1 - \frac{2}{l}|x|\right)$$

The Fourier transform of this distribution is:

$$I(k_x) = \hat{x}\frac{L}{2}\,sinc^2(k_x l/4)$$

which can be used to extract the field quantities from the dipole output voltage as demonstrated in Section (3 3).

In this work, this probe was used in most of the measurements from which the equivalent current model was evaluated. Because of the small size of the probe, it was possible to use it in field mapping within a moderate distance of the radiators. The field structure at such a distance is assumed to be smooth enough that the averaging effect of the probe is too small to change the mapped field structure.

B-3: Probe #3:

The third probe used is a short longitudinal monopole of Figure (B-3). This probe was used to map the field normal to the plane of measurement. The small size of the probe has two implications The first implication is that the field can be assumed to be measured at a point. The resulting field map, therefore, can qualitatively resemble the field structure The second implication is that the output power of the probe is low relative to that of the other two probes This probe is used, therefore, in measurement in the proximity of he radiators, where the field strength is high.

The model of this probe is not as simple as its structure. The coaxial feed, the exterior shell in particular, is part of the receiving surface of the dipole, which complicate the model of the probe. Field measurements using this probe are used mainly to gain some idea about the immediate field structure, or to prove the uniformity of the field amplitude and phase as in Figure (4.2).

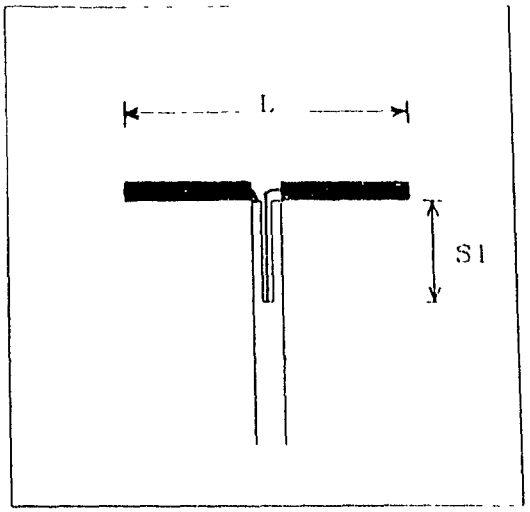

Figure (B-1). Probe #1; *balun* matched $\lambda/2$ dipole. The dipole element length, L, is 1.38cm., and the radius is 1.mm The slot length, Sl, is 1.cm., and the radius of the coaxial feed is .6mm.

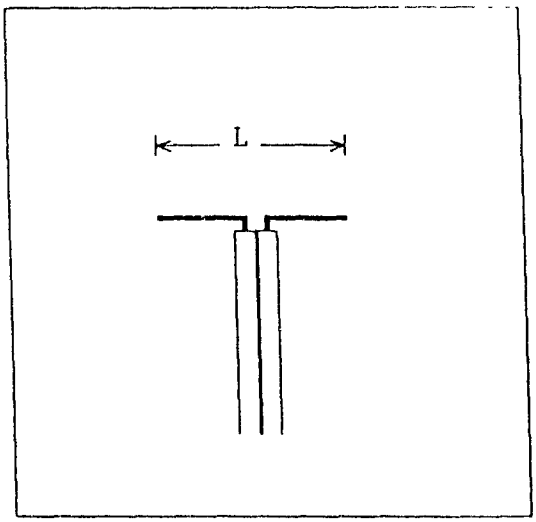

Figure (B-2): Probe #2; Balanced fed short dipole. The dipole element length, L, is .9cm., and the radius is .15mm. The radius of each coaxial feeds is .6mm.

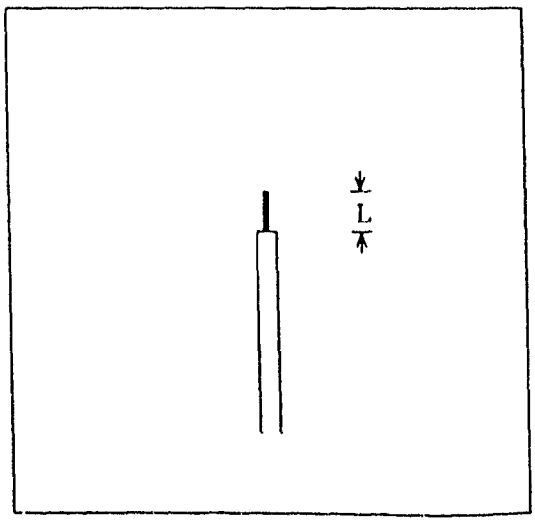

Figure (B-3): Probe #3; Longitudinal short monopole. The monopole element length is 1.mm., and radius .15mm. The feed radius is .6mm.

The above three figures are not drawn to scale.

APPENDIX (C)

DESCRIPTION OF THE EXPERIMENTAL FACILITY

The experimental work, described in chapters Three and Four, was conducted using the near-field scanning facility in the Antennas and Microwaves Laboratory, Department of Electrical Engineering, McGill University. This facility is, in principle, a tri-axial probe positioning system contained within a microwave anechoic chamber. The probe output and a reference signal from the input of the radiator under test are channeled to a microwave vector network analyzer for phasor field measurements. This facility is based on an existing system[65,66,67]. However, considerable modifications were made to the system to improve stability, accuracy and dynamic range, and will be mentioned here.

C.1. Probe Positioning System:

A schematic outline of the probe positioning part of the measurement system is shown in Figure (C-1), and the following description is referenced to this figure.

The probe movement is effected using a Modulynx motion control system. This system consist of three stepping motors, driver circuits and microprocessor control circuits. Each motor moves the probe along a rectangular coordinate axis, x, y or z. The translation of the motors angular rotation into linear movement along each axis is accomplished using precision lead screws. The probe can be located anywhere within a $1m^3$ cubic volume allowing three dimensional field scanning. A pedestal is used to hold the antenna or the radiator under test in a fixed, but adjustable, position relative to the scannable volume. In this work, the probe position coordinates are specified relative to a point of origin that is located on the radiator under test. The origin point is indicated on the figures describing each specific radiator that this thesis dealt with, specifically in figures (3.6), (4.1), (4.10) and (4.21)

The control over the probe movement, or in other words, over the stepping motors angular position, speed or acceleration is carried out using computer controlled stepping motor interface card (IODOO5A). The system is interfaced to the controlling computer (Hewlett Packard Vectra PC compatible) through a General Purpose Interface Bus (GPIB) board. The probe movement commands originate from the computer as the first step in measuring the probe output at a specified location.

Stepping motors can only move on fixed angular increments The design of the rotational to linear movement ratio allows a minimum increment of probe position of .02 mm. along each axis. For an operating frequency of 11.6 GHz , this increment corresponds to $7.75 \times 10^{-1}\lambda$.

The signal from the probe is linked to the network analyzer through RG53/U X-band rectangular waveguide. The connection between the moving probe and the network analyzer input port is effected using a movable linkage utilizing six waveguide rotary joints. This allows the freedom of probe in three dimensional movement within the scanning volume.

C.2. The Measuring Instruments:

A block diagram of the measuring instruments is shown in Figure (C.2), and the following description is referenced to this figure.

The microwave signal is generated by a Marconi instruments Type 6058A microwave signal source, amplified to approximately 5 watts using a Varian VTX 2679 B2 Travelling Wave Tube (TWT) amplifier This output power is necessary to produce a measurable field intensity around the radiators under test. The philosophy of this system is to use a relatively high operating power as a trade off against the high cost and possible non-linearity of high sensitivity receivers, as well as to operate over a wide dynamic range above the ambient noise level.

The TWT amplifier output is delivered to the radiator using a combination of waveguides and flexible coaxial cables depending on the measurement configuration Part of the radiator input signal is guided to the network analyzer as a reference signal through a 20 dB directional coupler. The measuring probe output is linked to the signal input of network analyzer through the waveguides and the rotary joints It was verified by the author that a significant immunity of phase measurement to frequency instability is achieved when the directional coupler that samples the radiator input is located close to the radiator. This will give nearly equal electrical length to the signal path and the reference path, and the change in that length contributed by the operating frequency and temperature fluctuation will tend to cancel at the network analyzer input The operating frequency is monitored by a Hewlett-Packard 5350A Microwave frequency counter, from which, the output frequency is reported to the computer through the GPIB-bus.

The vector network analyzer in the facility is a Hewlett-Packard model 8410A with a 8411A harmonic converter. The 8-12.4 GHz. frequency range setting is utilized in the experiments throughout this work. The network analyzer includes a plug-in module that displays the amplitude and phase of the signal channel relative to the reference channel.

The problem with using this module in an automated measurement is that the phase reading is unstable or even useless when the relative signal amplitude is low, and for phase values close to ±180 degrees. In addition, the range of phase measurement of the network analyzer becomes reduced as the signal amplitude get lower. This problem was solved by reading the amplitude and phase of an auxiliary I F outputs from the network analyzer (frequency= 278kHz) using a Hewlett-Packard 3575A Gain-Phase meter. This meter has D.C. outputs proportional to the relative amplitude and phase of the I.F. signal, with a stable phase measurements over the entire amplitude range.

The amplitude and phase information are transferred to the computer from the Gain-Phase meter D.C output using two Keithley 195A digital multimeters which are interfaced to the computer through the GPIB bus The measured amplitude is read in dB scale.

In summary, during the sequence of measuring the probe output at a point, first the computer gives a command to position the probe at a certain point, then, the amplitude and phase are accessed by the computer when the probe is stationary.

C.3. The Control and Data Acquisition Software:

The software for position control and data acquisition was specially written by P. Markland for the instrument configuration described earlier. The program accepts commands to set line or plane measurements, or measurements on trajectories, surfaces of arbitrary shapes or throughout a volume in keeping with a data set prescribed in an external file. The output file contains information about the measurement configuration, frequency and the measured amplitude and phase at each point of measurement In the case of planar measurement, and after each scanned line, the probe was commanded to return to a specific reference point and register the amplitude and phase at that point. This was useful in checking the stability of the measurements throughout the experiment.

C.4. Performance Verification:

One of the possible sources of error is the phase variation with the rotation of the waveguide rotary joints mentioned earlier. A check was conducted by replacing the probe with a short-circuit, feeding the probe waveguide with an input signal, and monitoring the reflected signal through a directional coupler. If the rotary joints rotation were modifying the probe output amplitude or phase, this would have been detected by a change in the reflected signal amplitude or phase as the probe is moved from one

extreme to another. There was no change on the reflected signal under these conditions, which indicated that the probe signal path had maintained a constant electrical length as the probe was moving.

The probe position was checked against the position command from the computer using high precision optical techniques[68]. It was found that a maximum deviation of 0.77 mm. (0 03λ at 11.6 GHz.) was present. This maximum deviation was located at one extreme of the scanning volume, where the reference position was set at the centre of this volume. This error limit is not serious for the purpose of this work.

The probe output waveguide is connected to the signal input of the network analyzer through a calibrated variable attenuator. In each experiment, the attenuation is varied with the probe fixed at a location with maximum expected output voltage, and the subsequent reduction in the reading of the network analyzer is compared to the added attenuation. This was necessary to insure that the signal input of the network analyzer operated within the linear region (unsaturated). An adjustment of the gain setting of the network analyzer was often necessary for this purpose.

The stability of the frequency and electrical length of the waveguides was improved by maintaining the whole measurement at a moderately stabilized room temperature. The stability of the measurements over the entire duration of the measurement, was monitored by reading the amplitude and phase at the fixed reference point mentioned earlier after each scanned line The variation of the measured amplitude and phase at the reference point during the measurement of Figure (4.22-a) is shown in Figure (C 3). Stable readings of the probe output voltage at the reference point and a field plot with no evidence of irregular behavior, unlike the one shown in Figure (4.14-a), were the major factors in considering a measurement results as acceptable.

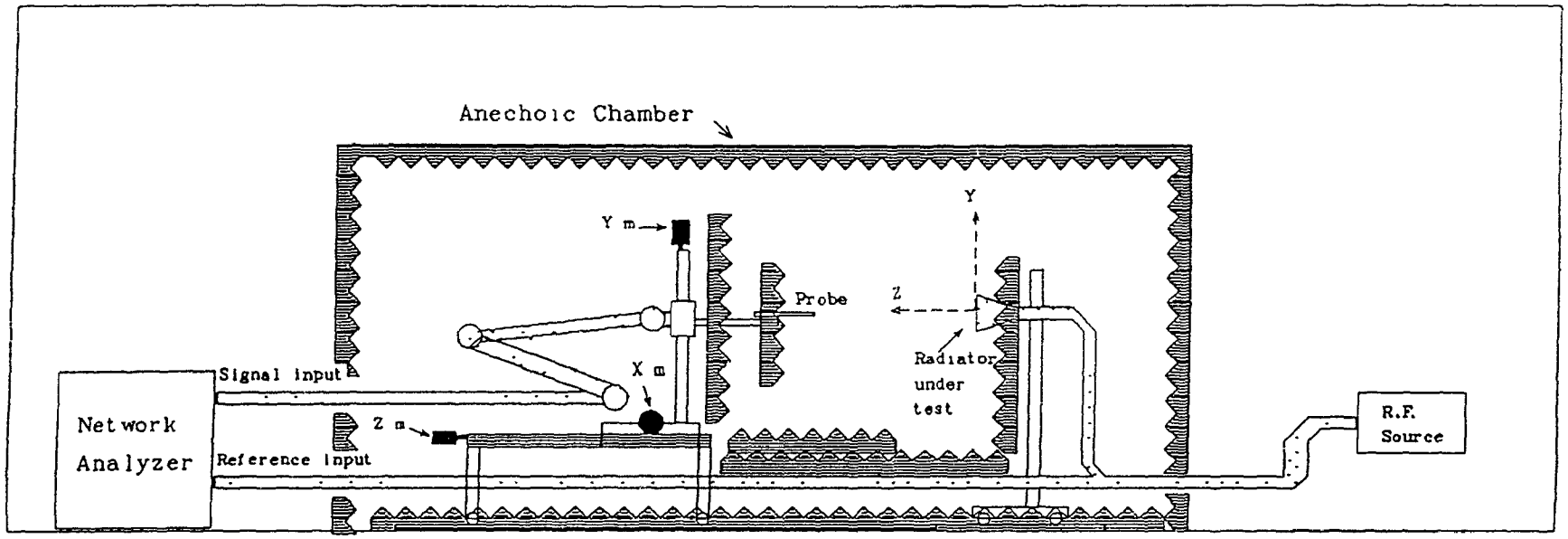

Figure (C.1). Schematic outline of the probe positioning system. The system is built inside a microwave anechoic chamber. The microwave absorbers are dark shaded, and the waveguides are distinguished with dot pattern. **Xm**, **Ym** and **Zm** indicate the locations of x, y and z motors respectively. The figure is not drawn to scale.

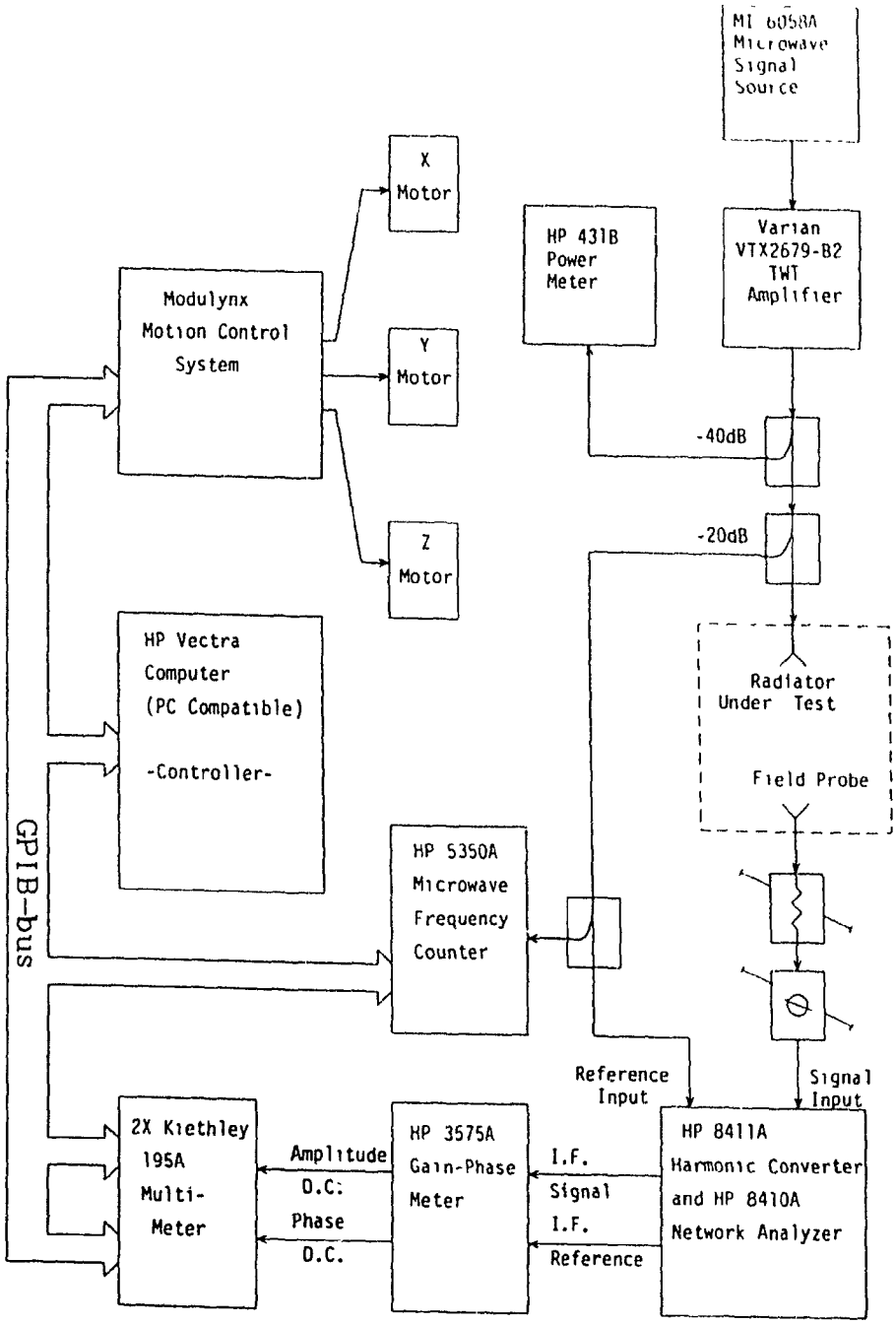

Figure (C.2): The measuring instruments: A block diagram.

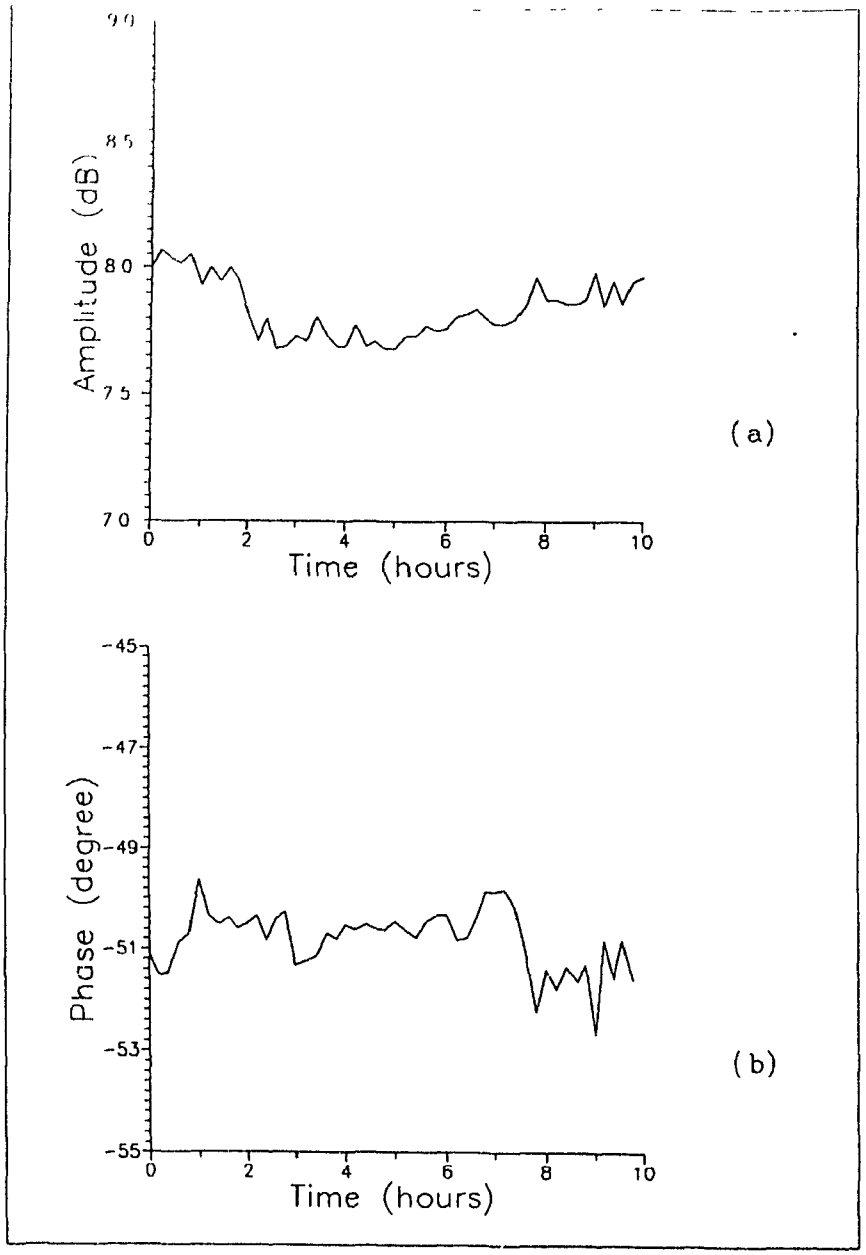

Figure (C.3): The amplitude and phase fluctuation at a fixed point versus time:

a- Amplitude (dB)

b- Phase (degrees).

This data was collected at a reference point $x=y=0$ and $z=5$ cm., during the measurement of data shown in Figure (4.22-a).

APPENDIX (D)

SOFTWARE DESCRIPTION

Some of the computer programmes developed for this work are described here Most of them are presented by the order of their use. The investigative nature of the work necessitate producing modular software with intermediate data files that can be inspected instead of large specialized programs. This approach resulted in programmes that are less user friendly, but easy to modify according to the conclusions drawn from the intermediate results.

Most of the software is written in FORTRAN, compiled using the Lahey F77L compiler with the SSP-PC external function library, and run on PC-compatible machines. The plots shown in this thesis were produced using Grapher, Surf and Topo packages for x-y plots, surface plots and contour maps respectively. The names given to the programmes in the following description do not follow any specific system

D.1. Format Conversion:

These are programmes that are used to convert the measurement files into format suitable for input to the data processing software. For example, some programmes produce separate amplitude and phase data files from the raw measurement data output of the control software described in the previous appendix. Additional programs are designed to prepare the data in a form suitable for plotting, such as the polar plots of figures (4.6) and (4.13).

D.2. Probe Modeling:

These are programmes that are used in processing the results of the experimental work of Section (3.4), and in the theoretical modeling of probe #1 described in appendix (B).

1. **DLPRC4.FOR:** A program to read the amplitude and phase resulting from the dipole probe measurements described in Section (3 4), produce the complex measured voltage, and Fourier transform this data. The outputs are two files, one of the complex spectral domain measured voltage, and the other of the magnitude of the spectral domain voltage for plotting, as shown in Figure (3.8).

2. **DL5PRC.FOR:** is an implementation of Equation (3.15) to find the spectral domain electric current distribution of the dipole probe under test from the complex measured spectral voltage. The algorithm employed by this program is detailed in Section (3.4). This program has produced the experimentally evaluated electric current distribution of Figure (3.9).

3. **POLY.FOR:** A program to calculate the coefficients of a forth order polynomial that analytically represents the spectral domain electric current distribution of the dipole tested in Section (3.4) from the output of DL5PRC.FOR. The QR decomposition[60] is used for solving the over-determined system associated with such calculations. The resulting polynomial for the dipole tested in that section at 11.65 GHz. is:

$$I(k_x) = 1 + 0.127k_x - 1.163k_x^2 + 0.974k_x^3 - 0.296k_x^4 \qquad -k_o < k_x < k_o$$

This polynomial was used to model the dipole probe in the field extraction for evaluating the plane wave spectrum in Figure (4.12) and the consequent calculation of the radiation patterns shown in Figure (4.13).

4. **MOMNG4.FOR:** A program to calculate the theoretical space domain electric current distribution on a dipole. The dipole specifications are entered from an external file. This program is based on the algorithm described by Stutzman and Thiele[41], Appendix (G). The spectral domain current distribution is calculated by DLPRC4.FOR to produce the theoretical probe data shown in Figure (3.9).

D.3. Microstrip Edge Experiments Data Processing:

These programmes are used in processing the resulting data of the experiments described in Section (4.1). Four modules are used for this purpose:

1. **MCREG1.FOR:** This program reads the measured voltage data along a line and the measurement parameters, as described in sub-section (4.1.2), performs the inverse Fourier transformation and extracts the complex electric field using the dipole probe #2 model given in Appendix (B). In addition to the intermediate file produced, which contains the complex spectral domain electric field, a file containing the magnitude of this quantity is produced for plotting. The resulting plotted data is shown in Figure (4.4).

2. **MCREG2.FOR:** Using the above-mentioned intermediate results, this program calculates the magnitude and phase of the equivalent magnetic current at the edge plane using Equation (2.5-a). The output magnitude curves corresponding to two experiments are shown in Figure (4.5).

3. **MCREG3.FOR:** This program calculates the electric field amplitude and phase over an x-z plane using Equation (2.1) as described in sub-section (4.1.3). The resulting data from such calculations is shown in Figure (4.7).

4. **PTRNEG.FOR:** This program is used to calculate the far-field radiation pattern of the microstrip edge from the measured spectral domain electric field resulting from the intermediate data of MCREG1.FOR. The calculation is based on equations (4.1) and (4.2), and the results from such a calculation are plotted in Figure (4.6).

D.4. Equivalent Currents and Near-Field Calculations:

EVANIK.FOR: This is a program to calculate the equivalent magnetic current at the radiator aperture, from the planar measurement data and parameters. The complex measured voltage is inverse Fourier transformed, and the electric field distribution in the spectral domain is extracted from the transformed data using the model of dipole probe #2, Appendix (B). The spectral domain currents at the radiator aperture are evaluated using Equation (2.5-a). The contour and surface plots of figures (4.16), (4.17), (4.18) and (4.23) are calculated using this program. Each polarization of the fields and currents is dealt with separately because of the assumption of linearly polarized response of probe #2.

The program has the following features:

1. The program can deal with values of maximum tangential wave number, $k_{t_{max}}$ in Section (2.4), larger than k_o. This implies that the evanescent modes can be employed in the equivalent currents calculations. These modes were employed in producing figures (4.16) and (4.17).

2. The field extraction procedure can be skipped, corresponding to an ideal measurement probe. Alternatively, The field values can be modified to simulate the response of different kinds of probes without applying the field extraction procedure. This was included to study the effect of the probe size on the evaluated aperture fields or currents.

3. The discrete Fourier transform (DFT) is used in this and the other programmes for transformation instead of the fast Fourier transform. Although that resulted in slower software, it offered a controllable spatial and spectral domain sampling rate. This advantage is exercised, for example in Figure (4.23), where the same information is shown for two different sampling rates and window sizes.

4. The option of multiplying the raw measurement data by a Hanning window function. This is used in investigating the effect of this window on the evaluated aperture currents.

FORTE.FOR: This is a program used to calculate the electric near-field on a plane parallel to the aperture plane, with specified dimensions and distance from the radiator. The program uses the aperture magnetic currents amplitude and phase data evaluated by EVANIK.FOR for that purpose. The algorithm is based on Equation (2.1) with J_s set to zero. This program is used to produce the field surface and contour maps shown in figures (4 19-a), (4.19-c), (4.25-a) and (4.25-c).

FORTE1.FOR: Similar to FORTE FOR, except that the field is evaluated over a plane normal to the aperture plane. This program is used to produce the contour maps shown in figures (4.20-a), (4.26-a) and (4.26-c).

D.5. Miscellaneous:

Other programmes were written, that do not fall within the above categories. Two programmes are used in the attempt to model the horn cluster as a contribution of individual horns, described in sub-section (4.3.2). The first, MESPC2.FOR, produces a preset number of spectral domain electric field data points within a pre-specified fraction of the radiation circle, from the planar measurement results. This data is used by HOMOD2.FOR to evaluate the excitation of each individual horn as described in the same sub-section.

The theoretical results shown in figures (2.4), (2.5) and (3.6) are calculated by programmes that are based on a one dimensional equation root finding algorithm for the first two figures and a two dimensional one for the latter figure.

The E-plane and H-plane far-field radiation patterns in Figure (4.13) are calculated from the plane wave spectrum data of Figure (4.12) using EXY.FOR which evaluated these patterns from the data shown in Figure (4.11) and the corresponding phase data.

REFERENCES

(1) Appel-Hansen,J., Gillespie,E.S., Hickman,T.G and Dyson,J D , "Antenna measurements", from *Handbook of Antenna Design*, Rudge,A.W., Milne,K., Olver,A.D. and Knight,P.,(*ed.*), Peter Peregrinus Ltd., 1982.

(2) Special Issue on Near-Field Scanning Techniques, *IEEE Trans on Antennas and Propagation*, Vol AP-36, No 6, June 1988

(3) Yaghjian,A D., "An overview of near-field antenna measurements", *IEEE Trans. on Antennas and Propagation*, Vol.AP-34, No 1, pp 30-45, Jan 1986

(4) Sletten,C J , "Reflector antennas", from *Antenna Theory*, Collin,R E and Zucker,F J. *(ed)*, Part 2, Chapter 17, McGraw-Hill Inc , 1969.

(5) Richmond,J.H. and Tice.T.E , "Probes for microwave near-field measurements", *IRE Trans on Microwave Theory and Techniques*, Vol MTT-3, pp 32-34, April 1955.

(6) Brown,J. and Jull,E V , "The prediction of aerial radiation pattern from near-field measurements", *Proc IEE*, Vol 108B, pp 635-644, Nov 1961

(7) Harrington,R.F., *Time Harmonic Electromagnetic Fields*, N Y McGraw-Hill, 1961.

(8) Silver,S., *Microwave Antenna Theory and Design*, MIT radiation Lab Publication, Vol.12, N.Y.: McGraw-Hill, 1949.

(9) Stratton,J.A., *Electromagnetic Theory*, N Y.: McGraw-Hill, 1941

(10) Collin,R.E., "Radiation from apertures", from *Antenna Theory*, Collin,R E and Zucker,F.J. *(ed.)*, Part 1, Chapter 3, McGraw-Hill Inc., 1969.

(11) Thal,H L.Jr., and Manges,J.B , "Theory and practice for a spherical-scan near-field antenna range", *IEEE Trans on Antennas and Propagation*, Vol AP-36, No.6, pp 815-821, June 1988

(12) Hansen,J.E *(ed). Spherical Near-Field Antenna Measurements*, Peter Peregrinus Ltd, 1988.

(13) Ponnapalli,S. and Sarker,T.K , "Near-field to far-field transformation) using an equivalent current approach", *Proc. of IEEE International Symposium on Antennas and Propagation AP-S 91*, London, Ontario, June 1991

(14) Sarker,T K., Ponnapalli,S and Arvas,E. "An accurate, efficient method of computing far-field antenna patterns from near-field measurements", *Proc of IEEE International Symposium on Antennas and Propagation AP-S 90*, Dallas, Texas, May 1990

(15) Levine,E., "Special measurement techniques for printed antennas", form *Handbook of Microstrip Antennas*, James,J.R. and Hall,P.S *(ed.)*, Vol.2, Chapter 16, Peter Peregrinus Ltd., 1989.

(16) Frayne,P G., "Microstrip field diagnostics", from *Handbook of Microstrip Antennas*, James,J.R. and Hall,P.S *(ed.)*, Vol 2, chapter 21, Peter Peregrinus Ltd, 1989.

(17) Chujo,W., Ito,T , Hori,Y. and Teshirogi,T . "Surface accuracy measurement of a deployable mesh reflector by planar near-field scanning", *IEEE Trans on Antennas and Propagation*, Vol AP-36, No.6, pp.879-883, June 1988

(18) Rahmat-Samii,Y. and Lemanczyk,J , "Application of spherical near-field measurements to microwave holographic diagnosis of antennas", *IEEE Trans. on Antennas and Propagation*, Vol.AP-36, No.6, pp 869-878, June 1988

(19) Bennet,J C., Anderson,A.P , McInnes,P.A. and Whitaker,A.J.T., "Microwave Holographic metrology of large reflector antennas", *IEEE Trans on Antennas and Propagation*, Vol AP-24, No.3, pp 295-303, May 1976.

(20) Lee,J.J , Ferren,E.M , Woollen,D P and Kuan M , "Near-field probe used as a Diagnostic tool to locate defective elements in an array antenna", *IEEE Trans. on Antennas and Propagation*, Vol AP-36, No 6, pp 884-889, June 1988.

(21) Tricoles,G., Rope,E L , and Hayward,R A., "Improved resolution in microwave holographic images", *IEEE Trans on Antennas and Propagation*, Vol.AP-29, No.2, pp.320-326, March 1981.

(22) Joy,E.B , "Near-field testing of radar antennas", *Microwave Journal*, Vol 33, No.1, pp.119-130, Jan. 1990

(23) Guler,M.G , Joy,E B and Black,D N., "Planar surface near-field data determined from spherical surface near-field measurements", *Proc. of the 1989 Antenna Measurement techniques Association Meeting*, pp 14/9-14/12, Monterey, California, Oct 9-13, 1989

(24) Guler,M.G , Joy,E.B Wilson,R E, Dubberley,J R , Slappy,A.L., Waid,S.C and Dominy,A.R , "Spherical backward transform applied to radome evaluation", *Proc. of the 1988 Antenna Measurement techniques Association Meeting*, pp.3/27-3/30, Atlanta, GA, Sept. 12-16, 1988.

(25) Lewis,R.L., and Newell,A C , "Efficient and accurate method for calculating and representing power density in the near zone of microwave antennas", *IEEE Trans. on Antennas and Propagation*, Vol.AP-36, No.6, pp 890-901, June 1988.

(26) Woonton,G A , "On the measurement of Diffraction fields", *Proc. of McGill Symposium on Microwave Optics*, pp.347-350, 1953

(27) Dyson,J.D., "Measurement of near-fields of antennas and scatterers", *IEEE Trans. on Antennas and Propagation*, Vol.AP-21, No 4, pp 446-460, July 1973.

(28) Bassen,H.I. and Smith,G S., "Electric probe - a review", *IEEE Trans on Antennas and Propagation*, Vol AP-31, No.5, pp.710-718, Sept. 1983.

(29) Kerns,D.M., "Correction of near-field antenna measurements made with an arbitrary but known probe", *Electronics Letters*, Vol 6, No.11, pp.346-347, May 28th, 1970

(30) Kerns,D M., *Plane-Wave Scattering-Matrix Theory of Antennas and Antenna-Antenna Interactions*, NBS Monograph 162, U S. Govt Printing Office, Washington D C , June 1981.

(31) Leach,W M and Paris,D T , "Probe compensated near-field measurements on a cylinder", *IEEE Trans. on Antennas and Propagation*, Vol.AP-21, No 4, pp.435-445, July 1973

(32) Farahat,K S and Bennet,J C , "Antenna near-field measurements using directive probes", *Proc. IEE*, Vol 133, Part H, No 1, pp.26-33, Feb. 1986.

(33) Paris,D T., Leach,W M. and Joy,E B , "Basic theory of probe-compensated near-field measurements", *IEEE Trans. on Antennas and Propagation*, Vol.AP-26, No.3, pp.373-379, May 1978

(34) Repjar,A.G , Newell,A.C. and Francis,M.H., "Accurate determination of planar near-field correction parameters for linearly polarized probes", *IEEE Trans on Antennas and Propagation*, Vol.AP-36, No.6, pp.855-868, June 1988.

(35) Yaghjian,A.D., "Efficient computation of antenna coupling and fields within the near-field region", *IEEE Trans on Antennas and Propagation*, Vol AP-30, No.1, pp.113-128, Jan. 1982.

(36) Sarker,T K., Weiner,D D. and Jain,V.K., "Some mathematical considerations in dealing with the inverse problem", *IEEE Trans. on Antennas and Propagation*, Vol.AP-29, No.2, pp 373-379, March 1981.

(37) Deschamps,G.A. and Cabayan,H.S. "Antenna synthesis and solution of inverse problems by regularization methods", *IEEE Trans. on Antennas and Propagation*, Vol.AP-20, No.3, pp.268-274, May 1972.

(38) Clemmow P C., *The Plane Wave Spectrum Representation of Electromagnetic Fields*, Pergamon Press Ltd , 1966

(39) Al-Mahdawi,T.I and Pavlasek,T.J F , "Wire and aperture probe modeling in planar near-field scanning", *ANTEM'90*, Winnipeg, Aug.15-17, 1990.

(40) Al-Mahdawi,T I. and Pavlasek,T J.F , "Measurement of correction parameters for a dipole probe", *IEEE International Symposium on Antennas and Propagation AP-S 89*, San jose, California, June 1989

(41) Stutzman,W L and Thiele,G A , *Antenna Theory and Design*, John Wiley and sons, 1981.

(42) Tikhonov,A N and Arsenin,V Y , *Solution of Ill-Posed Problems*, V H Winston and sons, Washington D C , 1977

(43) Mittra,R. *(ed)*, *Computer Techniques for Electromagnetics*, Oxford, N Y Pergamon Press, 1973

(44) Carlson,A.B., *Communication Systems: Introduction to Signals and Noise in Electrical Communications*, McGraw-Hill Inc., 1968.

(45) Roberts,R A. and Clifford,T.M., *Digital Signal Processing*, Addison-Wesley 1987

(46) Felsen,L.B., *Radiation and Scattering of Waves*, Englewood Cliffs,N.J · Prentice-Hall, 1973

(47) Newell,A.C., "Error analysis techniques for planar near-field measurements", *IEEE Trans on Antennas and Propagation*, Vol.AP-36, No 6, pp 754-768, June 1988.

(48) Wang,J.J.H., "An examination of the theory and practices of planar near-field measurements", *IEEE Trans. on Antennas and Propagation*, Vol AP-36, No.6, pp.746-753, June 1988.

(49) Jordan,E.C. and Balmain,K G , *Electromagnetic Waves and Radiating Systems*, Englewood Cliffs, N J : Prentice-Hall Inc , 1968

(50) Joy,E.B. and Paris,D.T , "Spatial sampling and filtering in near-field measurements", *IEEE Trans on Antennas and Propagation*, Vol AP-20, No 3, pp.253-261, May 1972.

(51) Collin,R.E., *Field Theory of Guided Waves*, N Y ·McGraw-Hill, 1960.

(52) Munson,R.E., "Microstrip Antennas", from *Antenna Engineering Handbook*, Johnson,R.C. and Jasik,H. *(ed.)*, Chapter 7, McGraw-Hill, 1984.

(53) James,J.R , Hall,P.S. and Wood,C., *Microstrip Antenna Theory and Design*, Peter Peregrinus, 1981

(54) Bahl,I J and Bhartia,P *Microstrip Antennas*, Artech House, 1980

(55) Special Issue on Microstrip Antennas, *IEEE Trans. on Antennas and Propagation*, Vol.AP-29. Jan. 1981

(56) Gupta,K.C. and Benalla,A *(ed.)*, *Microstrip Antenna Design*, Artech House Inc , 1988.

(57) Mosig,J.R., Hall,R.C. and Gardiol,F E , "Numerical analysis of microstrip patch antennas", from *Handbook of Microstrip Antennas*, James,J R and Hall,P S. *(ed)*, Vol.1, Chapter 8, Peter Peregrinus Ltd , 1989

(58) Williams,J.T., Delgado,H.J and Long,S.A., "An antenna pattern measurement technique for eliminating the fields scattered from the edges of a finite ground plane", *IEEE Trans. on Antennas and Propagation*, Vol AP-38, No 11, pp.1815-1822, Nov 1990.

(59) Wood,P.J., *Reflector Antenna Analysis and Design*, Peter Peregrinus, 1980.

(60) Dahlquist,G. and Bjorek,A., *Numerical Methods*, Englewood-cliff,N.J.: Printace-Hall, 1979.

(61) Henderson,A , James,J.R., Newham,P. and Morris,G., "Analysis of gating errors in time domain antenna measurements", *IEE Proceedings*, Vol.136, Part H, No.4, Aug. 1989

(62) Muresan,L V., "A near-field experimental investigation of interaction between two horns", Master of Engineering thesis, McGill University, Montréal 1981.

(63) Pavlasek,T.J.F. and Markland,P., Private Communication.

(64) Wegrowicz,L.A., Pokuls,R.A., Ilott,P.A., Markland,P.J. and Pavlasek,T.J.F., "Far-field prediction of reflector antennas by partial measurements", *1989 URSI Radio Science Meeting*, June 26-30, San Jose California 1989.

(65) Pavlasek,T.J F and Howarth,B.A., "Analysis of automatic homodyne method amplitude and phase measurements", *IEEE Trans on Microwave Theory and Techniques*, Vol.MTT-20, No.9, pp.623-626, Sept. 1972.

(66) Mishra,S., Pavlasek,T.J.F. and Muresan,L.V., "Automated computer based facility for measurement of near-field structure of microwave radiators and scatterers", *IEEE Trans. on Instrumentation and Measurements*, Vol.IM-29, No 4, pp.455-461, Dec. 1980.

(67) Ilot,P., Markland,P., Pavlasek,T. and Wegrowicz,L., "An immediate and near-field volume sscanning X and K-band facility", *Antenna Measurement Techniques Association*, Eighth Annual Meeting and symposium, Ottawa, Sept. 1986.

(68) Industrial Measurement Technologies Inc., "Measurement of position of microwave scanner head for McGill University", File.MCGILL01, Nov. 1988.